NASA Technical Paper 3002

AVSCOM Technical Report 89-A-002

May 1990

The Effects of Structural Flap-Lag and Pitch-Lag Coupling on Soft Inplane Hingeless Rotor Stability in Hover

William G. Bousman

US ARMY AVIATION SYSTEMS COMMAND AVIATION R&T ACTIVITY

NASA

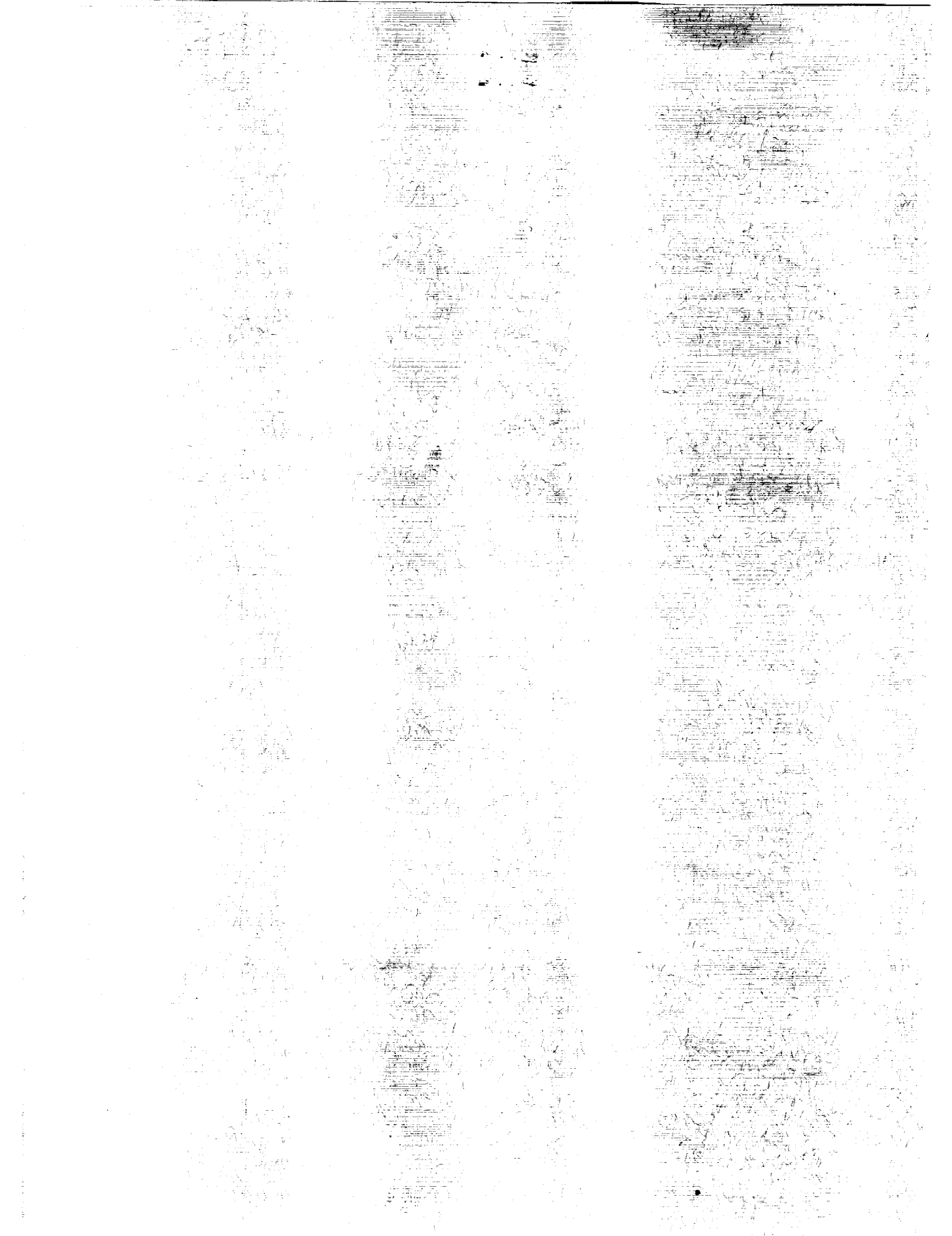

NASA Technical Paper 3002

AVSCOM Technical Report 89-A-002

1990

The Effects of Structural Flap-Lag and Pitch-Lag Coupling on Soft Inplane Hingeless Rotor Stability in Hover

William G. Bousman
Aeroflightdynamics Directorate
USAARTA-AVSCOM
Ames Research Center
Moffett Field, California

National Aeronautics and Space Administration
Office of Management
Scientific and Technical Information Division

PAGE 11 INTENTIONALLY BLANK

TABLE OF CONTENTS

PAGE IV INTENTIONALLY BLANK

SYMBOLS

a	linear two-dimensional section lift curve slope, rad^{-1}
B	tip loss factor
b	number of blades
C_o	coefficient of equilibrium lead-lag equation, equation (A6)
C_T	thrust coefficient, $T/\pi\rho\Omega^2 R^4$
C_β, C_ζ	coefficients of equilibrium and perturbation lead-lag equations, equations (A3) and (A4)
$C_{\dot\beta}, C_{\dot\zeta}, C_{\Delta\theta}, C_{\Delta\theta b}, C_{\Delta\theta h}$	coefficients of perturbation lead-lag equation, equations (A20), (A21), (A23), (A25), and (A27)
c	blade chord, in.
c_l, c_d	section lift and drag coefficients
$c_{l_o}, c_{d_o}, c_{l_\alpha}, c_{d_\alpha}$	nonlinear airfoil section parameters: local lift and drag coefficients, and local lift and drag curve slopes
c_{d_p}	airfoil profile drag coefficient at zero angle of attack
c_{l_p}	lift coefficient due to camber at zero angle of attack
D	reference dimension, ft
e	hinge offset, made dimensionless by R
F_o	coefficient of equilibrium flap motion, equation (A5)
F_β, F_ζ	coefficients of equilibrium and perturbation flap equations, equations (A2) and (A3)
$F_{\dot\beta}, F_{\dot\zeta}, F_{\Delta\theta}, F_{\Delta\theta b}, F_{\Delta\theta h}$	coefficients of perturbation flap equation, equation (A18), (A19), (A22), (A24), and (A26)
g	acceleration of gravity, ft/sec^2
I	blade inertia about hinge, lb_m-in^2
K	coupling parameter, equation (1)
K_β, K_ζ	combined flap and lead-lag spring stiffnesses at $\theta_h = \theta_b = 0$, ft-lb/rad, equations (A10) and (A11)
$K_{\beta f}, K_{\zeta f}$	flap and lead-lag spring stiffness of fixed hub springs, ft-lb/rad, figure 23
$K_{\beta h}, K_{\zeta h}$	flap and lead-lag spring stiffnesses of inclinable hub springs, ft-lb/rad, figure 23
$K_{\beta b}, K_{\zeta b}$	flap and lead-lag spring stiffnesses at blade root, ft-lb/rad, figure 23
m_b	blade mass, lb_m

R	rotor radius, in.
$\mathcal{R}$	rotor elastic coupling parameter
Re	Reynolds number, VD/ν
$\mathcal{R}_b, \mathcal{R}_h$	rotor blade and flexure elastic coupling parameters, equations (A13) and (A15)
$\mathcal{R}_{wb}, \mathcal{R}_{wh}$	elastic coupling parameters, equations (A28) and (A29)
$\mathcal{R}_{\beta b}, \mathcal{R}_{\zeta b}, \mathcal{R}_{\beta h}, \mathcal{R}_{\zeta h}$	ratio of spring element flexibility to overall flexibility for flap and lead-lag degrees of freedom, equation (A12)
r_{cg}	blade center of gravity measured from hinge, in.
s	Laplace transform variable, sec^{-1}
T	thrust, lb
V	reference velocity, ft/sec
α	angle of attack, rad
β	blade flapping deflection about axis parallel to the plane of rotation, deg, figure 23
γ	Lock number, $\rho acR^4/I$
Δ	stiffness parameter, equation (A8)
δ_3	negative pitch-flap coupling
ζ	blade lead-lag deflection about an axis parallel to rotational axis, deg, figure 23
η_m	lead-lag structural damping ratio
θ	blade pitch angle, deg
θ_b	inclination of principal flexural axes of blade, deg, figure 23
θ_h	inclination of flexural axes of hub, deg, figure 23
θ_β	pitch-flap coupling, positive when pitch is nose up and flap is up; $\partial\theta/\partial\beta$
$\theta_{\beta o}$	pitch-flap coupling of flexures when $\theta_h = 0°$
$\theta_{\beta b}, \theta_{\beta h}$	pitch-flap coupling parameters, equations (A34) and (A35)
θ_ζ	pitch-lag coupling, positive when pitch is nose up and lead-lag is forward, $\partial\theta/\partial\zeta$
$\theta_{\zeta o}$	pitch-lag coupling of flexures when $\theta_h = 0°$
ν	kinematic viscosity of air, ft^2/sec
ρ	density of air, slug/ft^3
σ	rotor solidity, $bc/\pi R$
σ_ζ	real part of lead-lag mode eigenvalue or measured lead-lag damping exponent, sec^{-1}

ϕ_i	downwash angle at 3/4 blade radius, rad
ω_Y	stand lateral frequency, Hz
$\omega_{\beta o}, \omega_{\zeta o}$	uncoupled flap and lead-lag mode nonrotating frequencies *in vacuo*, rad/sec or Hz
ω_β	measured flap frequency, Hz
$\bar{\omega}_\Delta^2$	flap-lag elastic coupling parameter, equation (A7)
ω_ϵ	frequency difference, Hz
ω_ζ	imaginary part of lead-lag mode eigenvalue or measured lead-lag mode frequency, rad/sec or Hz
Ω	rotor angular velocity, rad/sec or rpm
$(\ )_o, \Delta(\ )$	equilibrium and perturbation quantities
$(\bar{\ })$	made dimensionless by Ω

THE EFFECTS OF STRUCTURAL FLAP-LAG AND PITCH-LAG COUPLING ON SOFT INPLANE HINGELESS ROTOR STABILITY IN HOVER

William G. Bousman

Ames Research Center

and

Aeroflightdynamics Directorate, U.S. Army Research and Technology Activity

SUMMARY

A 1.62-m-diameter rotor model was tested in hover to examine the effects of structural flap-lag and pitch-lag coupling on isolated rotor blade lead-lag stability. Flap-lag coupling was introduced by inclining the principal axes of the blade structure up to 60°. Pitch-lag coupling was obtained either alone or in combination with flap-lag coupling through the use of skewed flexural hinges. The principal results confirm the predictions of theory, and show that both structural flap-lag and pitch-lag coupling when used separately are beneficial to blade stability. Moreover, when the couplings are combined, the lead-lag damping is significantly greater than it would be if the individual contributions were superimposed. Pitch-flap coupling is shown to have only a minor effect on blade lead-lag damping. Differences between theory and experiment observed at zero blade pitch and flexure angles during the initial testing were determined in a second test to be caused by stand flexibility. Other differences between theory and experiment warrant further investigation.

INTRODUCTION

A simplified mathematical model of an isolated hingeless rotor blade in hover, derived by Ormiston and Hodges (ref. 1), has been useful in obtaining an understanding of the behavior of hingeless rotors, and of how their stability is influenced by aeroelastic coupling. In particular, the distribution of blade flexibility inboard or outboard of the pitch change bearing has a strong effect on the elastic coupling of the rotor flap and lead-lag motions, and hence on blade stability. The major predictions of this work were confirmed in subsequent small-scale rotor experiments (ref. 2), and the essential features of the mathematical model were validated for the cases where the flexibility is primarily inboard of the pitch change bearing ($\mathcal{R} \approx 0$), or outboard of the pitch change bearing ($\mathcal{R} \approx 1$). Additional experiments (ref. 3) followed, using a rotor configuration with the flexibility distributed equally inboard and outboard of the pitch change bearing ($\mathcal{R} \approx 0.5$), and the results showed reasonable agreement with theory.

The mathematical model of reference 1 has been used to study the influence of various types of aeroelastic coupling on the damping of soft inplane hingeless rotors with the specific intent of finding ways to significantly augment the damping of the lead-lag mode (ref. 4). Ormiston has examined the flap and lead-lag perturbation equations that at a blade pitch angle of 0° are coupled by

$$K = \frac{\mathcal{R}\bar{\omega}_\Delta^2 \sin 2\theta_h}{2\Delta}\left(\frac{\mathcal{R}\bar{\omega}_\Delta^2 \sin 2\theta_h}{2\Delta} - \frac{\gamma}{8}\theta_\zeta\right) \quad (1)$$

The lead-lag damping of the rotor is increased if K is positive and decreased if K is negative. Structural flap-lag coupling is represented by the term $\frac{\mathcal{R}\bar{\omega}_\Delta^2 \sin 2\theta_h}{2\Delta}$ and depends primarily on the elastic coupling, $\mathcal{R}$; the difference between the flap and lead-lag stiffness, $\bar{\omega}_\Delta^2$; and the inclination of the structure's principal axes, θ_h. The pitch-lag coupling of the rotor is accounted for in the term $\frac{\gamma}{8}\theta_\zeta$, in which the pitch-lag coupling is positive when the nose of the blade pitches up with leading motion of the blade. The effect of the coupling term is slight for small values of flap-lag or pitch-lag coupling, but in combination the effect can be quite large. This is shown in figure 1, where the predicted variation in lead-lag damping is shown as a function of the primary variables in equation (1)—the flexural inclination, θ_h, and the pitch-lag coupling, θ_ζ.

At inclination angles of 0° or 90° the damping is caused only by the profile drag on the blade, and is very small. If the pitch-lag coupling is zero, the effect of flap-lag coupling is to increase the rotor damping a small amount. However, the combined effect of flap-lag and pitch-lag coupling is to strongly increase the lead-lag damping.

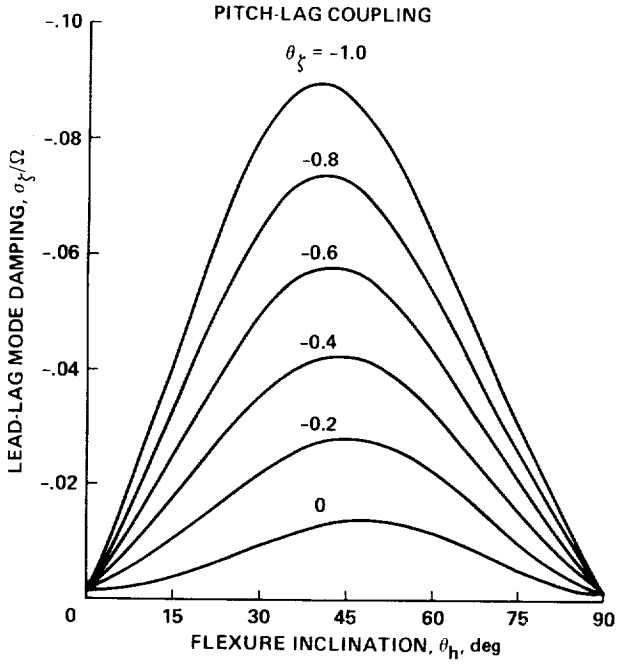

Figure 1.– Effect of inclination of principal flexural axes and pitch-lag coupling on lead-lag mode damping at 0° pitch angle; $p = 1.1, \bar{\omega}_\zeta = 0.7, \gamma = 8, 2c_{d_p}/a = 0.01, \theta_\beta = 0$.

An experiment with a model rotor was undertaken with the objective of examining the effects of structural flap-lag and pitch-lag coupling separately and in combination, and of validating the theoretical model. The more significant results of this experiment, reported in reference 5, in general confirmed the augmentation of lead-lag damping that was predicted by theory. However, the comparison of theory and experiment also showed a number of areas of disagreement. In a subsequent experiment, two of these areas of disagreement were examined: (1) the substantially higher damping measured at low blade pitch angles for a configuration with combined structural and flap-lag coupling, and (2) the higher damping measured for a configuration without any coupling at 0° pitch angle.

The report starts with a brief discussion of the theoretical model and its influence on the experimental design. A detailed description of the rotor model is given, and the test procedures and methods used for data analysis are discussed. The test results are then presented, starting with the effects of structural flap-lag coupling alone, proceeding to a discussion of pitch-lag coupling alone, following with a discussion of pitch-flap coupling alone, and concluding with a discussion of flap-lag and pitch-lag coupling in combination. Approximately 60% of the data are new and were not reported in reference 5. In addition, data from the second experiment that relate to the first area of disagreement mentioned above are included here. There are three appendices. The equations of motion used for the correlation are presented in appendix A. Appendix B contains a description of the model. Appendix C contains a description of the second experiment, which dealt with the second area of disagreement mentioned above, and the results of that experiment.

EXPERIMENT DESCRIPTION

Experiment Design

The objective of the experiment was to obtain measurements of damping and frequency, and then to compare these measurements with the predictions in reference 4. The theoretical model in reference 4 is highly simplified, being restricted to a single, isolated rotor blade in hover with one flap and one lead-lag degree of freedom. The blade is assumed to be rigid and to be hinged at the rotor center, and its flexibility is represented by spring restraints at the central flap and lead-lag hinges as shown in figure 2. A major problem was determining how to represent this spring-restrained, centrally hinged, rigid blade with a physically realizable model. The approach taken was to approximate the spring-restrained hinges of the theoretical model using short flexures placed as close to the hub centerline as possible. The blade, in turn, had to be much stiffer than the flexures.

Structural flap-lag coupling is provided by rotating the flap and lead-lag flexures about a spanwise axis. The inclination of the flexure can be varied from 0° to 90° independently of the pitch angle of the blade. Pitch-lag coupling was obtained by skewing the flexural axes so that lead-lag deflections cause an appropriate change in the pitch angle.

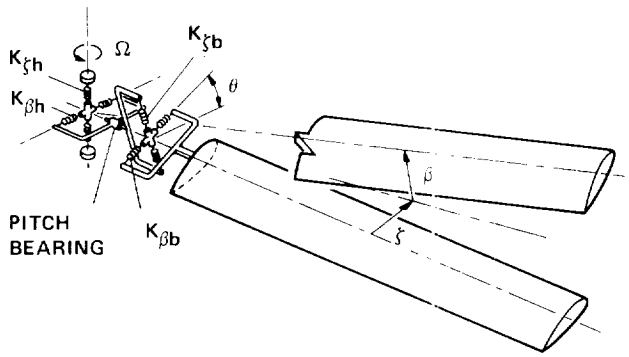

Figure 2.– Representation of hingeless rotor blade with spring-restrained, centrally hinged, rigid blade. (For clarity, blade springs are shown offset from axis of rotation.)

The blade torsion mode was effectively decoupled from the blade flap and lead-lag degrees of freedom by designing the root flexures to be very stiff in torsion. The stand stiffness was selected so that its first cantilever frequencies were above the lead-lag mode natural frequencies in the fixed system. However, as shown in appendix C, the frequency separation was not enough to prevent coupling between the stand and the lead-lag degree of freedom at the higher rotor speeds.

Model Rotor

A photograph of the model rotor (fig. 3) shows the root end of the blades, the blade root flexures, and the rotor hub. In this picture, the flexural axes are inclined at 36°. The design of the flexures can be better understood by examining the exploded view in figure 4. The lead-lag and flap flexures are separate elements, but are connected by two side beams that fold back the load path so that when the flexures are assembled, their centerlines are approximately coincident. The inner portion of the lag flexure is bolted to the hub through a set of mounting rings that allow the lead-lag and flap flexural axes to be rotated to any desired angle. A blade root socket is mounted on the outboard end of the flap flexure, and this socket mates with the cone at the blade root. Clamps are used to lock the blade into the socket. All connections are bolted or clamped to minimize the effects of friction and free play. Changes in flexural inclination and blade pitch angle are made by hand.

Skewed flap and lead-lag flexures were built in addition to the straight flap and lead-lag flexures shown in figure 4. The straight and skewed flexures were interchangeable and therefore four flexure combinations could be tested, as is shown in figure 5. Configuration one, the straight flap/straight lead-lag flexure set shown in figure 5(a), represents a rotor without any coupling when the flexure inclination, θ_h, is set to 0°. This is the baseline rotor to which all configuration changes are compared. The effect of structural flap-lag coupling is examined by changing the flexure inclination; the maximum coupling results when the flexure inclination is 45°.

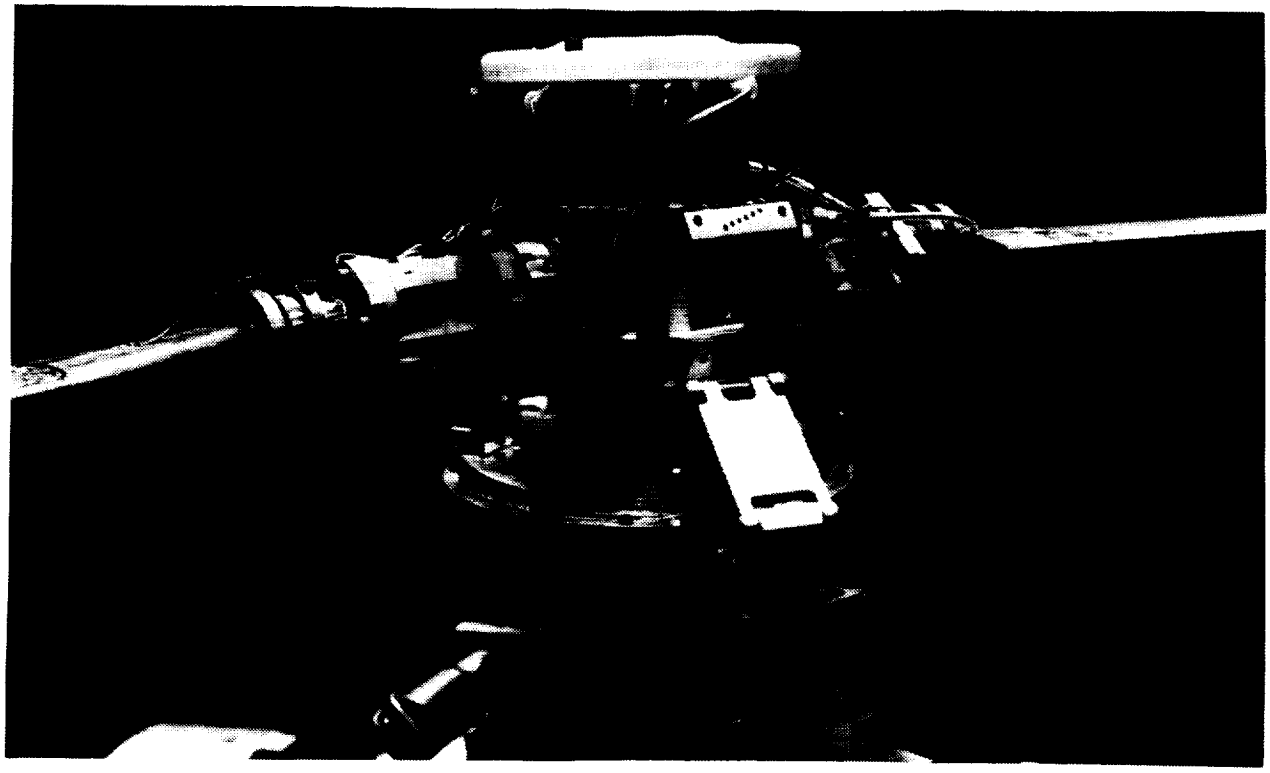

Figure 3.– Model rotor.

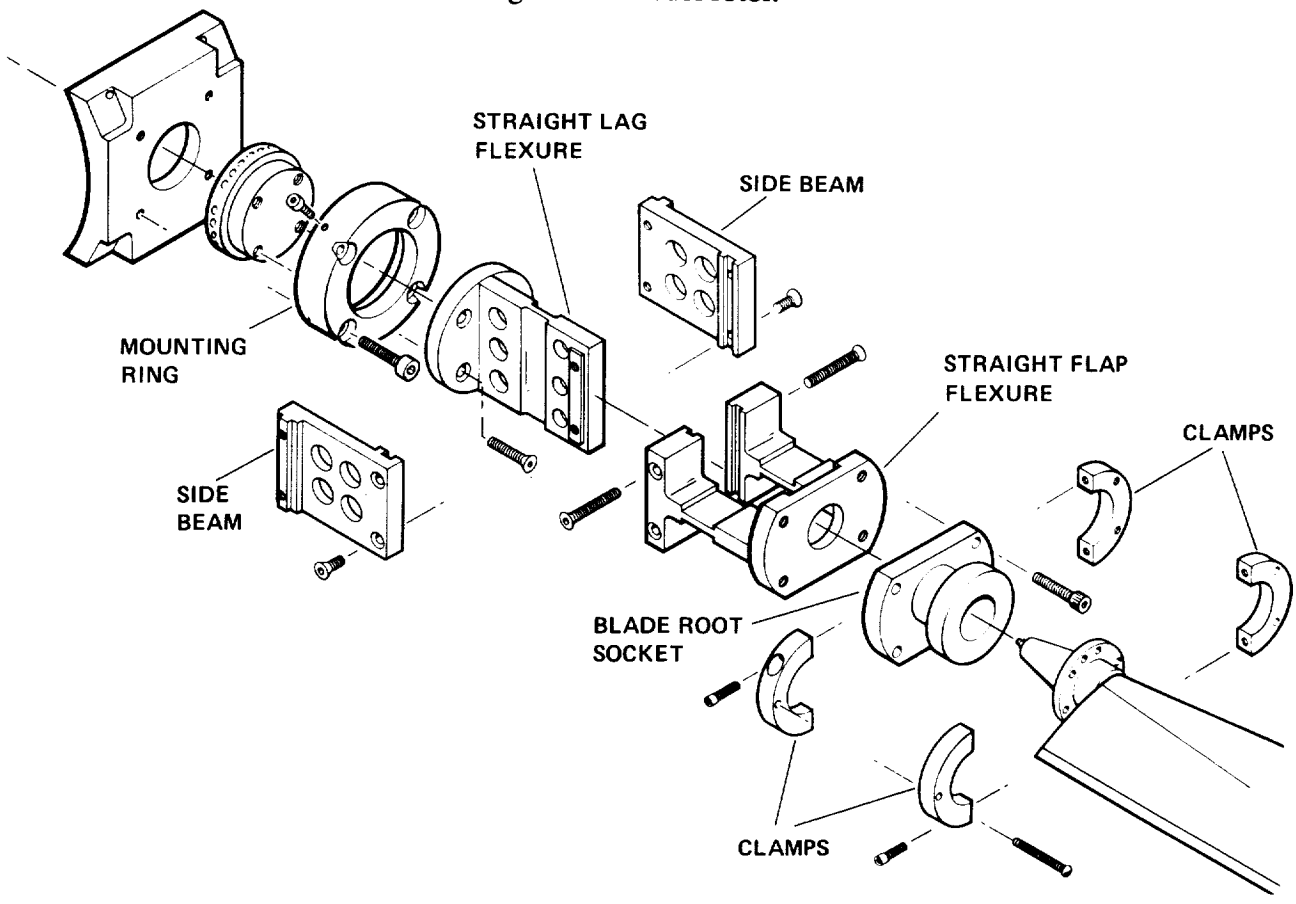

Figure 4.– Rotor blade flexures.

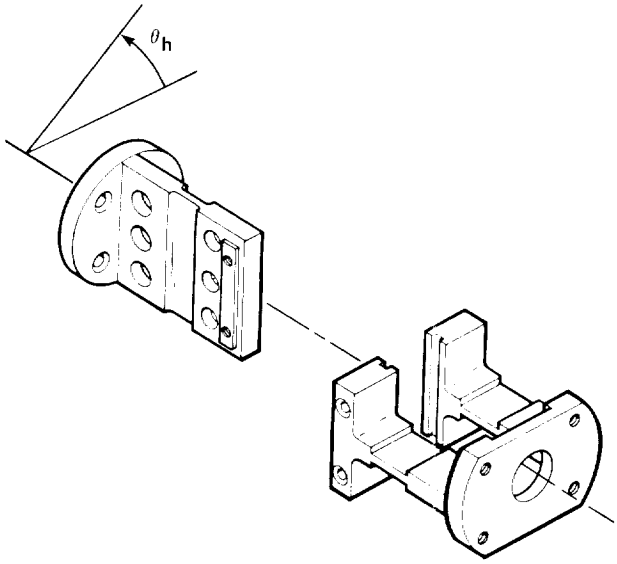

(a) Straight flap/straight lead-lag flexures (configuration one).

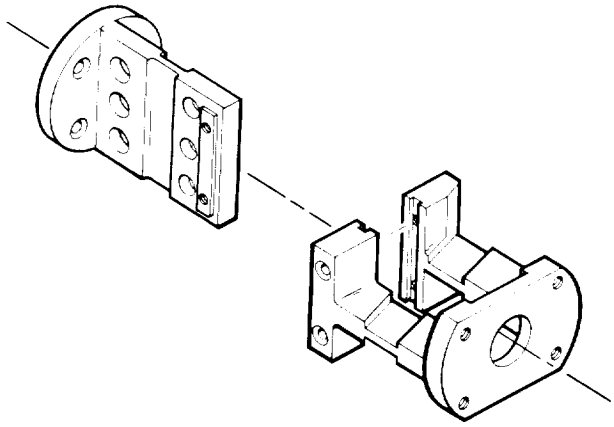

(c) Skewed flap/straight lead-lag flexures (configuration three).

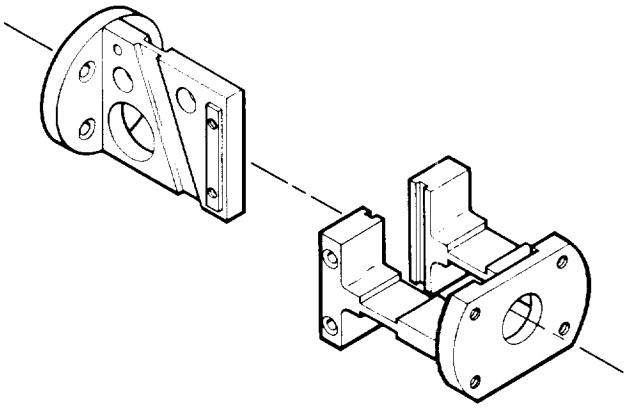

(b) Straight flap/skewed lead-lag flexures (configuration two).

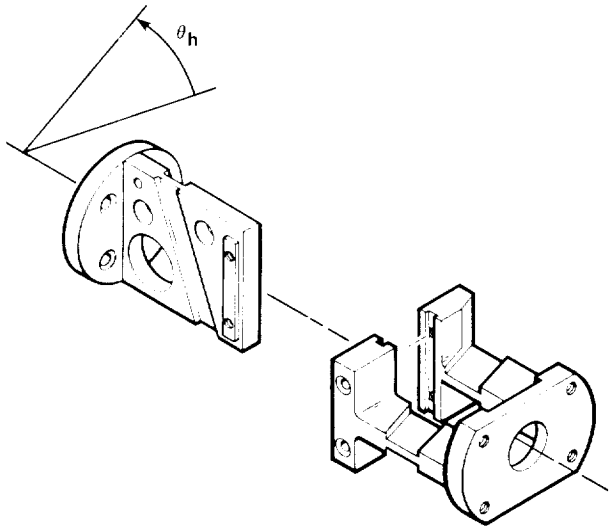

(d) Skewed flap/skewed lead-lag flexures (configuration four).

Figure 5.– Rotor blade flexure combinations.

The effect of pitch-lag coupling alone is examined using the straight flap/skewed lead-lag set (configuration two), shown in figure 5(b). For this set the flexure inclination is fixed at 0°, and only the blade pitch angle is changed. The skewing of the lead-lag flexure causes negative pitch-lag coupling; that is, as the blade leads forward the kinematic effect of the skewed flexure is to make the blade twist down, which results in negative pitch-lag coupling.

The effect of pitch-flap coupling alone is examined in a similar fashion using the skewed flap/straight lead-lag flexure set (configuration three) as shown in figure 5(c). In this case the skewing of the flap flexure is such that as the blade flaps up,

the blade twists up, providing positive pitch-flap coupling (or negative δ_3). The flexure inclination is fixed at 0° for these tests to avoid the effects of structural flap-lag coupling.

The effects of structural flap-lag and pitch-lag coupling in combination are investigated using the skewed flap/skewed lead-lag flexure set (configuration four), shown in figure 5(d). In this figure the skewed flexures are shown at a flexural inclination of zero; hence, the flap-lag coupling is also zero. The skewed lead-lag flexure provides negative pitch-lag coupling, whereas the skewed flap flexure causes positive pitch-flap coupling. As flexural inclination, θ_h, is increased in order to increase the flap-lag coupling, the effect of the skewed lead-lag and flap flexures will change as well. In figure 5(d) it can be seen that for $\theta_h = 0°$ the skewed lead-lag flexure causes negative pitch-lag coupling; that is, as the blade leads forward, it will pitch down. When the skewed lead-lag flexure is rotated to 90°, there is no longer any pitch-lag coupling—when the blade leads forward, no pitch angle is induced. Now, however, the skewed lead-lag flexure will induce negative pitch-flap coupling. For $\theta_h = 90°$, as the blade flaps up, the skewed lead-lag flexure forces the blade to pitch down. Thus the effect of flexural inclination on the skewed pitch-lag flexure is to change the coupling from negative pitch-lag to negative pitch-flap. Similar arguments apply to the skewed flap flexure, which causes positive pitch-flap coupling when $\theta_h = 0°$, and negative pitch-lag coupling at $\theta_h = 90°$. The coupling of the two flexures combine as

$$\begin{Bmatrix} \theta_\zeta \\ \theta_\beta \end{Bmatrix} = \begin{bmatrix} \cos\theta_h & -\sin\theta_h \\ \sin\theta_h & \cos\theta_h \end{bmatrix} \begin{Bmatrix} \theta_{\zeta o} \\ \theta_{\beta o} \end{Bmatrix} \qquad (2)$$

The resulting pitch-lag and pitch-flap coupling for this flexure combination is shown in figure 6 as a function of the flexure inclination. The flexure skew angles have been selected so that their pitch-lag contributions are additive, while their pitch-flap values are in opposition. At the design point, where $\theta_h = 36°$, the pitch-lag coupling reaches a

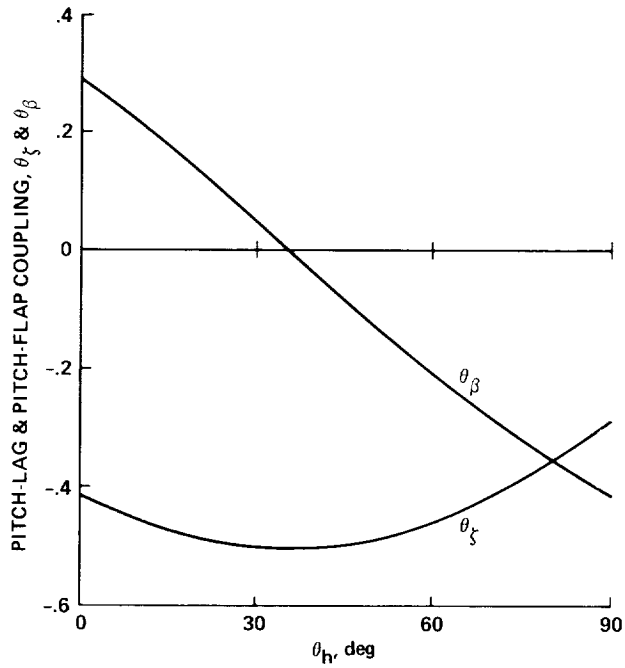

Figure 6.– Pitch-lag and pitch-flap coupling of skewed flap/skewed lead-lag flexure combination as the flexure inclination is varied.

minimum and the pitch-flap coupling is zero. For lower flexure inclinations, $\theta_h < 36°$, there will be increasing amounts of positive pitch-flap coupling, while for higher flexure inclinations, $\theta_h > 36°$, there will be increasing amounts of negative pitch-flap coupling.

The flexures were machined from 17-4 PH stainless steel, and heat-treated to achieve a yield strength of 174 kpsi. Parts outboard of the flexures such as the blade sockets and clamps were made of titanium to minimize weight. The model blades are untwisted and are made of an aramid fiber, fiberglass, and balsa wood. Both uniaxial and cross-ply layers of the aramid fiber were included, to provide high stiffness in both bending and torsion. The blade was laid up in a mold machined to NACA 23012 contours. More detail on the blade construction can be found in reference 6. Descriptive characteristics of the rotor are given in table 1. Additional detail is provided in appendix B.

TABLE 1.– ROTOR PARAMETERS

Parameter	Value
Blade radius, R, in.	31.92
Blade chord, c, in.	1.65
Solidity, σ	0.033
Hinge offset, e	0.105
Lock number, γ	7.99

The rotor test stand and excitation system are shown in figure 7. Figure 8 shows more detail of the rotor and stand. The rotor was driven through a 7.5:1 reduction gearbox by two 4.5 kW, water-cooled, electric motors mounted on opposite ends of the model. The motors, the gearbox, and the model were mounted in a gimbal frame which allowed freedom about the model's roll axis for excitation of the blade natural frequencies. The excitation source was an electrodynamic shaker that oscillated the model through the linkage shown in the figures. Following excitation, a pair of pneumatic clamps was applied to the linkage to lock out the motion.

The model in figure 7 was originally designed with a five-component balance just below the hub assembly. The fixed system controls and the swashplate assembly were mounted metrically on this balance on a structure that also acted as the inner bearing support for a pair of angular duplex bearings on which the hub rotates. For these tests, the five-component balance was replaced with a pedestal support that was substantially stiffer than the balance. However, a replacement bearing support was not available in time for the tests, so the swashplate and the control assembly were left on the stand although they were not connected to the blades.

Cables (not shown in fig. 7) were attached to the stand below the yoke and were connected to the test-area floor to provide additional stiffening of the stand. With the cables installed and the excitation linkage locked by the pneumatic clamps, the first lateral stand frequency was approximately 27 Hz and the first longitudinal stand frequency was about 29 Hz. (The first stand frequency of 38 Hz reported in reference 5 is in error.) In figure 9, these stand frequencies are compared with the blade lead-lag natural frequencies that appear in the fixed system at values of $\Omega \pm \omega_\zeta$. At the maximum rotor speeds tested, 840 rpm for the straight lead-lag flexure and 880 rpm for the skewed lead-lag flexure, the lead-lag natural frequencies are at 23 and 24 Hz, respectively. When the first experiment was performed, the indicated frequency separation of 15% was believed to be acceptable. However, as was demonstrated in the second test (see appendix C), a considerably greater separation is required to avoid errors in the frequency and damping measurements.

The model was tested in a chamber approximately 25 ft high, 20 ft wide, and 26 ft long. Although the room was vented to the atmosphere, no attempt was made to disperse the wake or to reduce recirculation through baffles or similar structures. The ratio of the rotor plane height above the floor to the rotor diameter was 0.82, which is less than the desired value of 1.2; however, full-scale test data indicate that the thrust augmentation in this case was less than 2% (ref. 7). Neither room recirculation nor ground-plane effects on induced flow were measured, nor were corrections made to the theory. The effect of induced flow changes on isolated blade stability is, in general, slight (ref. 8).

Instrumentation

Strain gage bridges were installed on both the flap and lead-lag flexures in a conventional manner to measure the bending moment at the flexure centerline. An additional strain gage bridge was added to the flap flexures to determine the torsional moment by measuring the bending moment at the flexure root due to torsion, rather than using the more conventional torsion strain gage bridge. Bridge excitation and signal leads were routed to an instrumentation "beanie" and were then passed down the center of the drive shaft, where they connected to a 60-channel slip ring mounted in the base of the

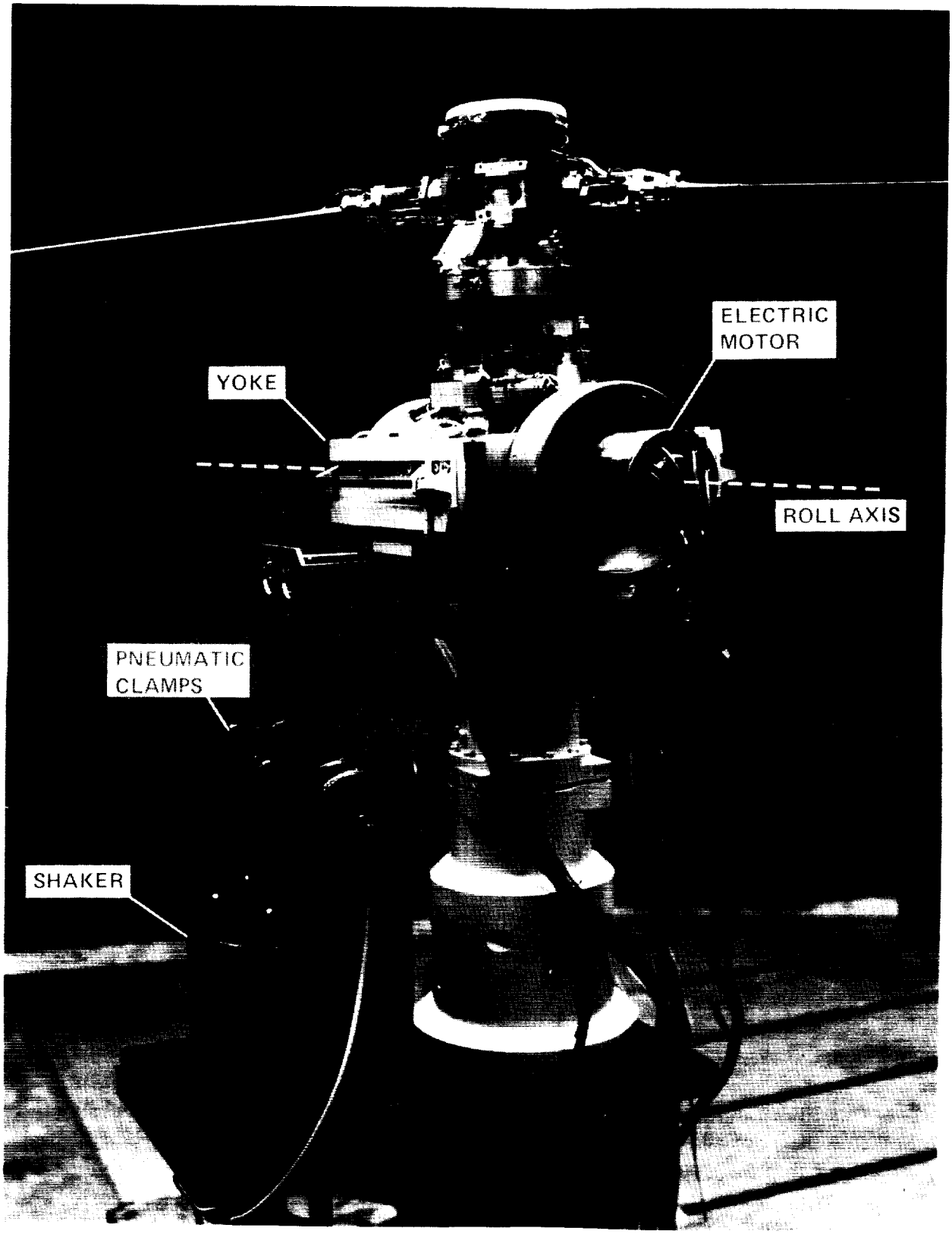

Figure 7.– Two-bladed rotor model showing stand and excitation system.

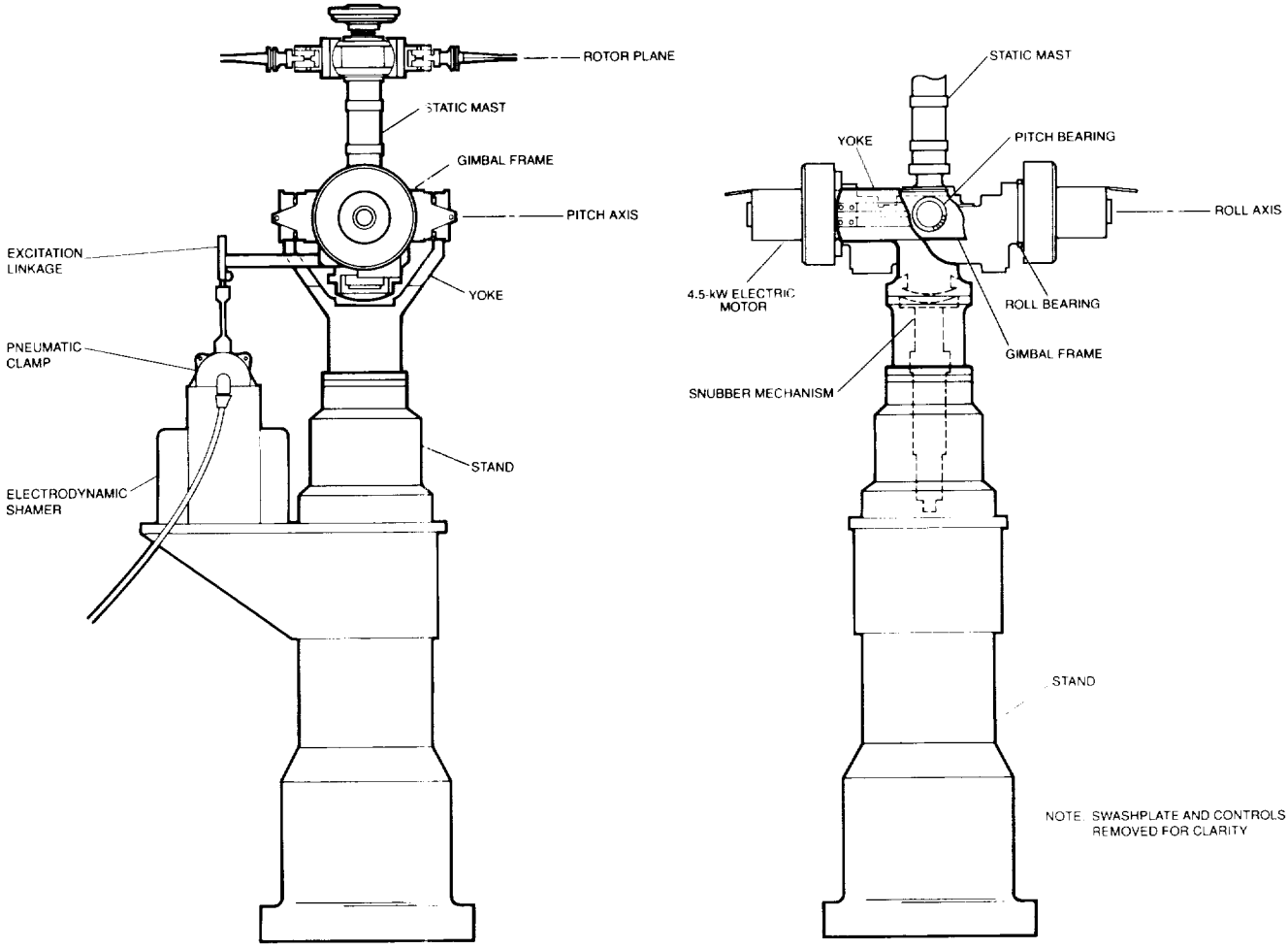

Figure 8.– Two views of model rotor and stand.

transmission. The signals from the slip ring were conditioned and amplified in a conventional fashion, and were then displayed or recorded on oscilloscopes, oscillographs, and analog FM tape, as required.

The flexure strain gage bridges were calibrated to determine the flexure flap, lead-lag, and torsional moments as a function of strain gage output. Flexure angular deflections were also measured, to provide an estimate of flexure stiffness. Two kinds of transducers were used to determine the angular deflection: a sensitive accelerometer and an electrolytic cell inclinometer. The accelerometer detected the angular deflection by measuring the sine of the angle of the gravity vector; however, drift and temperature sensitivity made these measurements unreliable. The electrolytic cell inclinometer measured angular deflection from the change in electrolytic conductivity as an anode-cathode combination was tilted with respect to an electrolyte/vacuum interface. These latter measurements were considered satisfactory.

Rotor speed was measured with both 1/rev and 60/rev sensors, the latter being used only for online monitoring and control of the model. Accelerometers mounted to the static mast were used to detect stand motion during measurements.

Testing Methods

The flap and lead-lag modes of the single blade combine for this two-bladed configuration to form four modes: flapping collective and differential modes, and lead-lag collective and differential modes. The collective flapping mode, in which

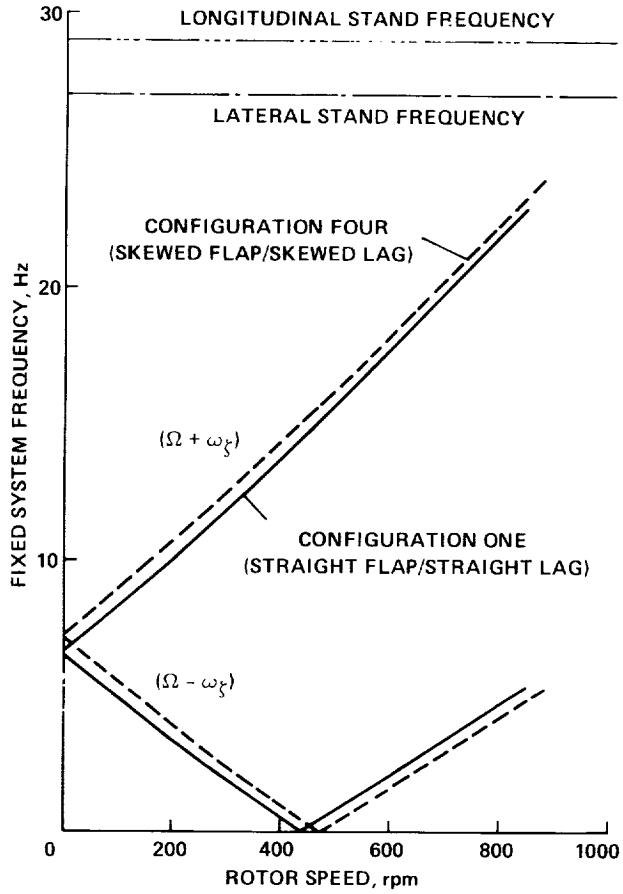

Figure 9.– Blade lead-lag natural frequencies and test-stand cantilever frequencies in the fixed system, $\theta_h = \theta_b = 0°$.

both blades are in phase, is reacted by the vertical stiffness of the hub support, while the differential flapping mode is reacted by the stand lateral and longitudinal stiffnesses. Both flapping modes are highly damped because of the blade aerodynamics; therefore measurement of frequency and damping is extremely difficult except at low rotor speeds. Of the two lead-lag modes, the collective mode couples directly with the drive system, so that its frequency and damping are dependent upon the drive system inertia, damping, and stiffness. For the lead-lag differential mode, the blade's motions are out of phase and react each other such that the mode is torqueless, that is, the blades act as mirror images of each other in the rotating system, and thus simulate the isolated blade of theory. The measurement problem, then, was to determine the frequency and damping of the lead-lag differential mode.

The lead-lag differential mode was excited by oscillating the model about the roll axis using an electrodynamic shaker. This mode was excited at a fixed system frequency of either $\Omega + \omega_\zeta$ or $\Omega - \omega_\zeta$ until sufficient amplitude of blade motion was achieved, at which point the excitation was cut off and the motions were allowed to decay. Most of the test data were obtained using a frequency of $\Omega + \omega_\zeta$, because the shaker performance was better in this frequency range.

The strain gage bending moment signals recorded from each lead-lag flexure showed both collective and differential modes. These signals were differenced electronically to remove the collective mode which acts as a contaminant or noise source, and the differential mode was reinforced. The frequency and damping of the differential mode were estimated from the differenced signals as described in reference 9. Briefly, this technique tunes a tracking filter to the lead-lag frequency to provide both a narrow-bandpass, filtered signal and the logarithm of the rms amplitude of the filtered signal. The log rms signal has the useful property that, for an exponential decay, the output signal is a linear function of time and its slope is proportional to the exponent of the decay.

Because most commercially available tracking filters have poor time-domain performance, rapid changes in signal level at frequencies outside the filter bandwidth tend to cause errors in the tracking filter output. This difficulty can be alleviated if the transient is recorded on analog tape and then played backward through the tracking filter. The tracking filter then reads the exponential decay as an exponential rise, and the performance is significantly improved (ref. 9). Two examples of the application of the tracking filter to the experimental data are shown in figures 10 and 11. Figure 10 exhibits a tracking filter analysis for a case with low damping that shows very little noise contamination. For times less than 0.0 sec the data represent forced oscillation of the blades. At 0.0 sec the excitation

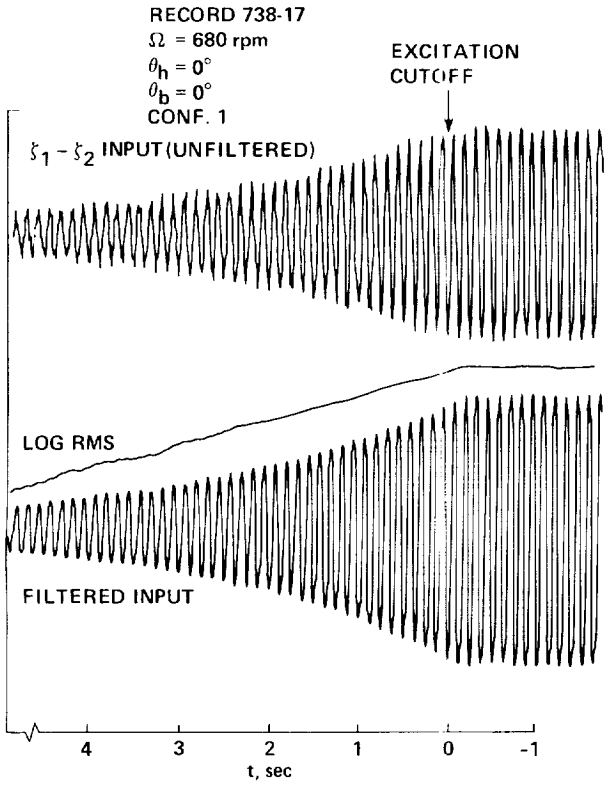

Figure 10.– Example of tracking filter analysis for case with low damping in which the signal is played backward.

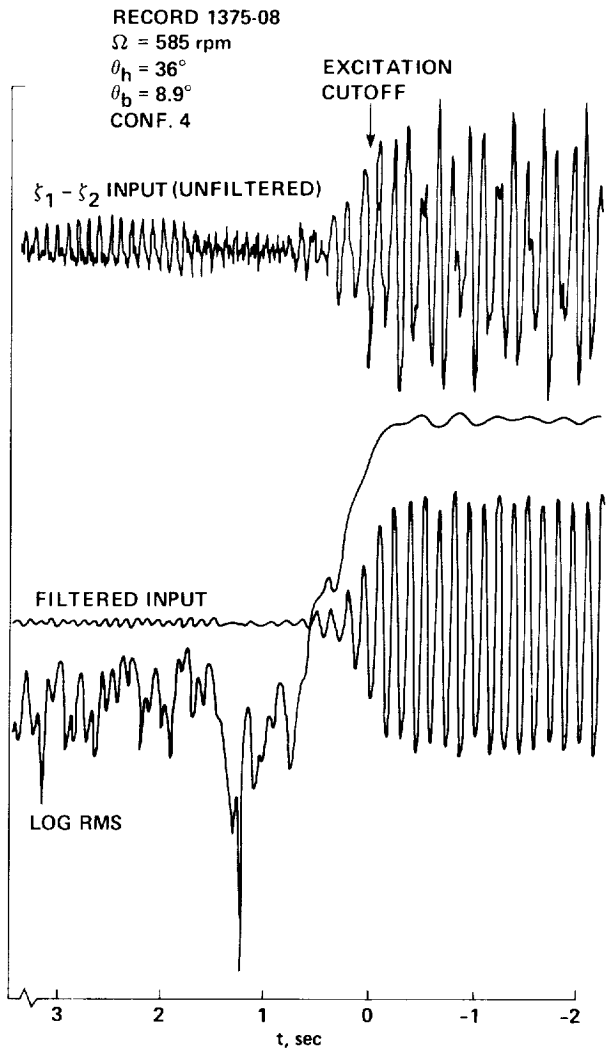

Figure 11.– Example of tracking filter analysis for case with high damping in which the signal is played backward.

is cut off (see arrow) and the blade oscillation decays. A small amount of noise can be seen in the unfiltered decay; this is essentially eliminated in the filtered signal. The time-domain characteristics of the filter cause an approximate 0.2-sec shift of the signal to the right. The filtered signal is used to estimate the modal frequency. The location of the signal maximum in each cycle can be measured within 0.01 sec from the oscillograph trace, so for the 5 sec of data shown here the frequency can be estimated within ±0.2%. The damping is estimated from the slope of the log rms signal over the linear region from 0.0 to 2.5 sec. The accuracy that can be achieved in measuring frequency and damping is degraded at high damping levels, as can be seen in figure 11. For this case, where the blade pitch is about 9°, noise in the signal is apparent both during excitation and afterward (the contamination is largely 1/rev). The effect of the noise is reduced in the filtered signal, but since the blade motion damps out after only six or seven cycles, the accuracy of the frequency and damping estimates is reduced. At each test condition two transient decay signals were recorded on the oscillograph, and an additional two were recorded on analog tape for subsequent playback and analysis.

TEST RESULTS

Configurations Tested

Four configurations were tested using the four combinations of straight and skewed flexures outlined in table 2. The effects of structural flap-lag coupling alone were investigated using configuration one, the straight flap and straight lead-lag flexures. The primary emphasis was on the effects of flexure inclination and the differential stiffness between flap and lead-lag on the lead-lag modal damping at zero blade-pitch angle. The effects of pitch-lag coupling alone were examined using configuration two, the straight flap/skewed lead-lag flexure set. The emphasis here was on the effect of blade pitch angle on the lead-lag mode damping. The skewed flap/straight lead-lag flexure set, configuration three, was tested to examine the effects of pitch-flap coupling on the lead-lag mode damping. Finally, the last configuration, the skewed flap/skewed lead-lag flexure set, was tested to investigate the effects of flap-lag and pitch-lag coupling in combination, particularly at zero blade-pitch angle.

Measurements of modal damping and frequency were obtained for the four test configurations for the parameter variations shown in table 2. The effects of structural flap-lag coupling were investigated by rotating the flexures so that they were inclined to the rotor disk plane by the inclination angle, θ_h. The blade pitch angle was then adjusted to its prescribed value (normally 0°). The rotor was run up to a speed selected to give the desired value of the nondimensional lead-lag frequency. For cases where the blade pitch angle was greater than zero the rotor speed selected was the same one used for the zero-pitch-angle condition. The data for the investigation of pitch-lag and pitch-flap coupling alone (configurations two and three) were obtained with the inclination angle set at zero to avoid the effects of flap-lag coupling. The data for the skewed flap/skewed lead-lag flexures (configuration four) were obtained using the same procedures as for configuration one.

Theoretical calculations are compared with the measurements in the following sections. The theoretical model is largely the same as presented in reference 5, and is discussed in appendix A. The derivation of the model properties used in these calculations is given in appendix B.

Structural Flap-Lag Coupling

Effects of flexure inclination and the flap-lag stiffness difference at zero pitch angle– The straight flap/straight lead-lag flexures (configuration one) were tested to examine the effects of structural flap-lag coupling on the damping of the lead-lag mode. The effects of structural flap-lag coupling are caused both by the flexure inclination and the difference in stiffness between the flap and lead-lag

TABLE 2.– TEST CONFIGURATIONS

	Configuration one	Configuration two	Configuration three	Configuration four
Flap flexure	Straight	Straight	Skewed	Skewed
Lead-lag flexure	Straight	Skewed	Straight	Skewed
Reference figure	5(a)	5(b)	5(c)	5(d)
Flexure inclination, θ_h, deg ($\theta_b = 0°$)	0, 18, 36, 39, 42, 45, 48, 51, 54, 60	—	—	0, 18, 36, 39, 42, 45, 48, 51, 54, 60
Nondimensional lead-lag frequency, $\bar{\omega}_\zeta$, ($\theta_b = 0°$)	0.60, 0.65, 0.70, 0.75, 0.80	0.60, 0.65, 0.70, 0.75, 0.80	—	0.60, 0.65, 0.70, 0.75, 0.80
Blade pitch angle, θ_b, deg ($\bar{\omega}_\zeta = 0.70$)	0-9	0-9	0-9	0-9 ($\theta_h = 0, 18, 36, 51, 60°$) –4-0 ($\theta_h = 36°$)

degrees of freedom. This can be seen by examining the expression

$$\frac{\mathcal{R}}{2\Delta}\left(\frac{K_\zeta}{I\Omega^2}-\frac{K_\beta}{I\Omega^2}\right)\sin 2\theta_h$$

taken from equation (1). The term for the nondimensional stiffness difference, $\bar{\omega}_\Delta^2$, has been expanded here to show its dependency on the flexure stiffnesses and on the rotor speed. The effect of flexure inclination is seen in the last term, $\sin 2\theta_h$, which has its maximum value at an inclination of 45°. Since the flap and lead-lag stiffnesses are constant, the dominant effect here is that of the rotor speed. As the rotor speed increases, the nondimensional stiffness difference, the nondimensional lead-lag frequency, and the structural flap-lag coupling decrease. The two effects can be examined, therefore, by varying the flexure inclination and the rotor speed. For these tests the rotor speed was chosen to give a constant value of the nondimensional lead-lag frequency for all flexure inclinations.

The flap-lag coupling effects are illustrated in figure 12, in which the lead-lag frequency and damping are shown as functions of flexure inclination for three values of nondimensional lead-lag frequency. In all cases the effect of flexure inclination is to increase the lead-lag damping until a maximum is reached, at about 50°. This maximum occurs at an angle beyond 45° because the nondimensional stiffness is also increasing with flexure inclination, since the rotor speed must be reduced to maintain a constant nondimensional lead-lag frequency. The lead-lag frequency and damping are shown in figure 13 as functions of the nondimensional lead-lag frequency for four values of flexure inclination. At low values of flexure inclination, the effect of the nondimensional lead-lag frequency is quite small. However, at large flexure inclinations the effect is large, as expected.

The comparison of theory and experiment shown in figures 12 and 13 is qualitatively good in that both the measurements and the calculations show similar increases in damping as a result of the flexure inclination and the nondimensional stiffness difference term. However, a number of differences are seen between theory and experiment, especially at the lower values of nondimensional lead-lag frequency (high rotor speed) where the theory underestimates the measured damping, and at the higher values of nondimensional lead-lag frequency (low rotor speed) where the theory overestimates the measured damping. The data obtained in the second test entry (presented in appendix C) demonstrate that errors occurred in both frequency and damping because of coupling between the stand and rotor degrees of freedom. This may explain some of the discrepancies seen here; however, as discussed in appendix C, the errors caused by coupling with the stand are largest at high rotor speed and smallest at low rotor speed. Therefore, the substantial differences between theory and experiment seen at the lowest rotor speeds (see fig. 12(c)) cannot be explained by this coupling.

The damping data in figure 12 show a curious dip at a flexure inclination of about 45° that is not seen in the theoretical predictions. This is especially noticeable at a nondimensional frequency of 0.80 (fig. 13(c)). These data are plotted on an expanded scale in figure 14, to which a hand-faired fit of the data has been added to show the dip more clearly. In all cases the dip in the damping corresponds closely to a flexure inclination of 45° and seems unrelated to rotor speed or lead-lag frequency.

Effect of blade pitch angle on damping at $\bar{\omega}_\zeta = 0.7$ – The rotor model was tested over a blade-pitch-angle range of 0–9° for flexure inclinations of 0°, 36°, and 54°. The damping data were analyzed for the case of $\bar{\omega}_\zeta = 0.7$ and the results are shown in figure 15. At all three flexure inclinations the effect of the blade pitch angle is to increase the lead-lag damping. This increase in damping is greater at the higher flexure inclinations. The theory underestimates the measured damping at $\theta_h = 0°$, but shows good agreement at the higher flexure inclinations.

Pitch-Lag Coupling

The straight flap/skewed lead-lag flexure set (configuration two) was tested to investigate the effects of pitch-lag coupling alone. The flexure inclination was fixed at 0° to avoid flap-lag coupling, and the effect of the skewed lead-lag flexure was to

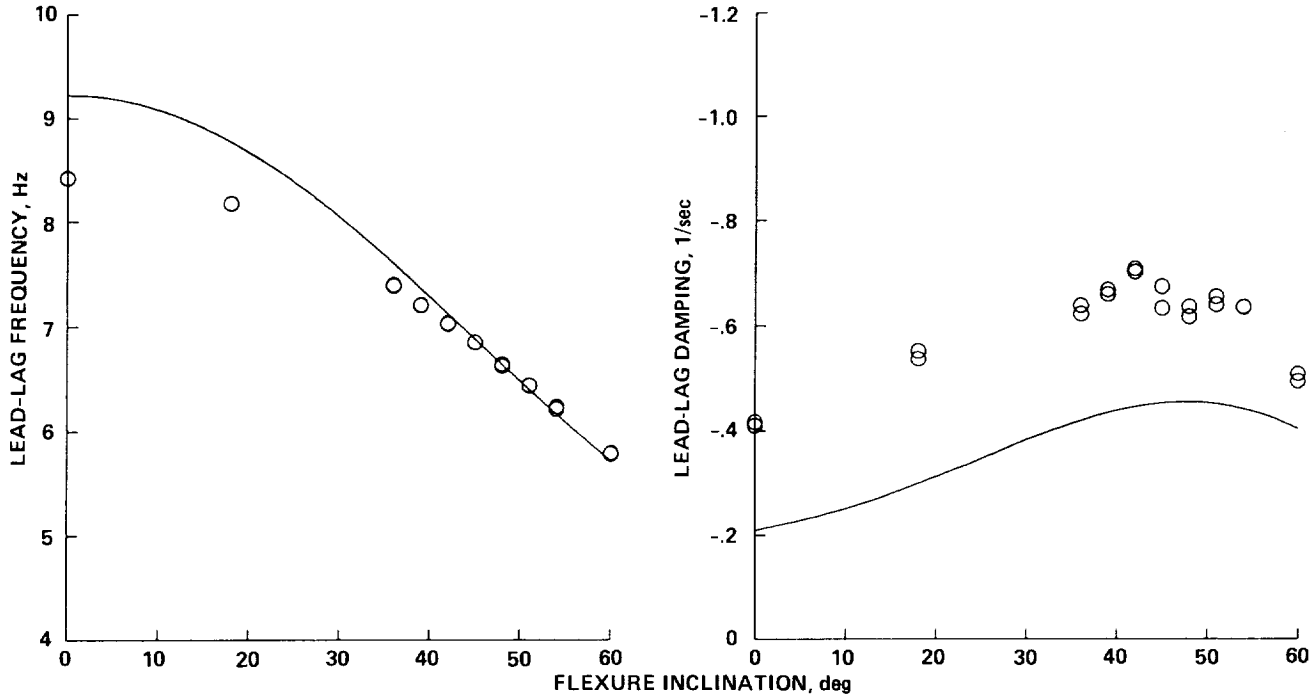

(a) $\bar{\omega}_\zeta = 0.6$.

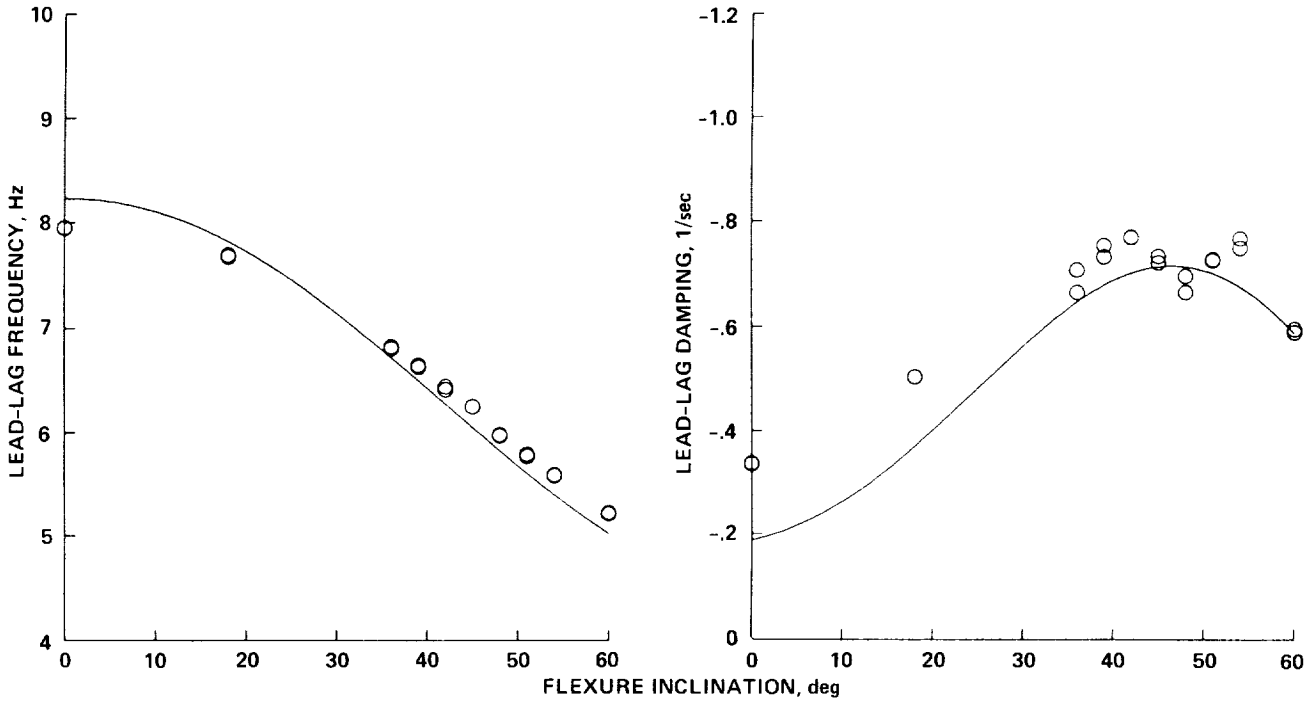

(b) $\bar{\omega}_\zeta = 0.7$.

Figure 12.– Lead-lag frequency and damping for straight flap/straight lead-lag flexures (configuration one) as functions of flexure inclination, $\theta_h = 0°$.

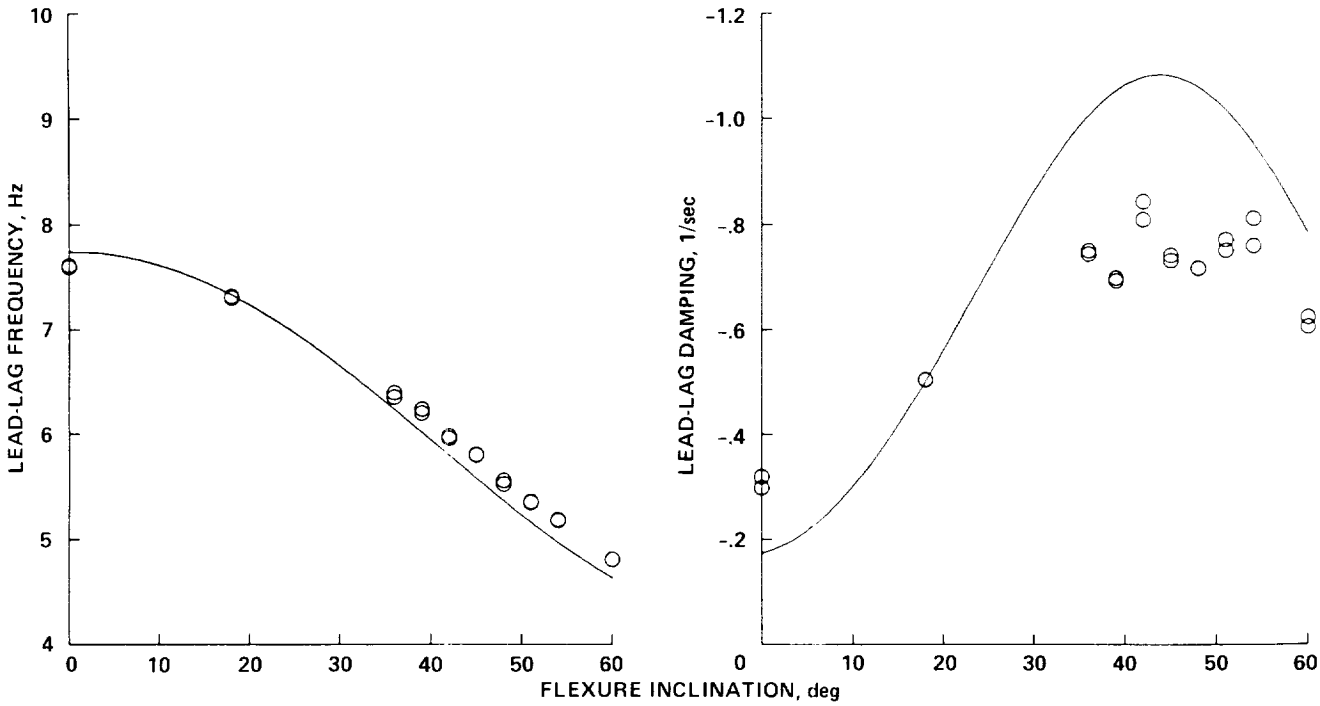

(c) $\bar{\omega}_\zeta = 0.8$.

Figure 12.– Concluded.

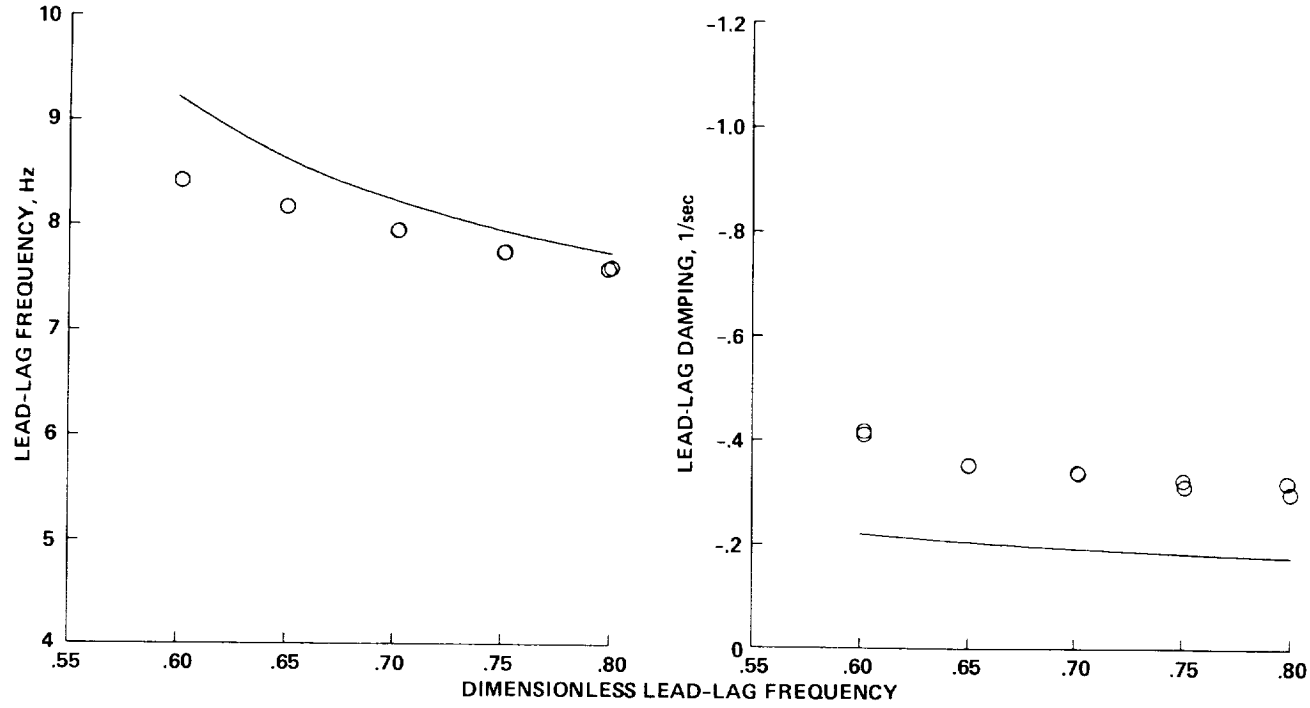

(a) $\theta_h = 0°$.

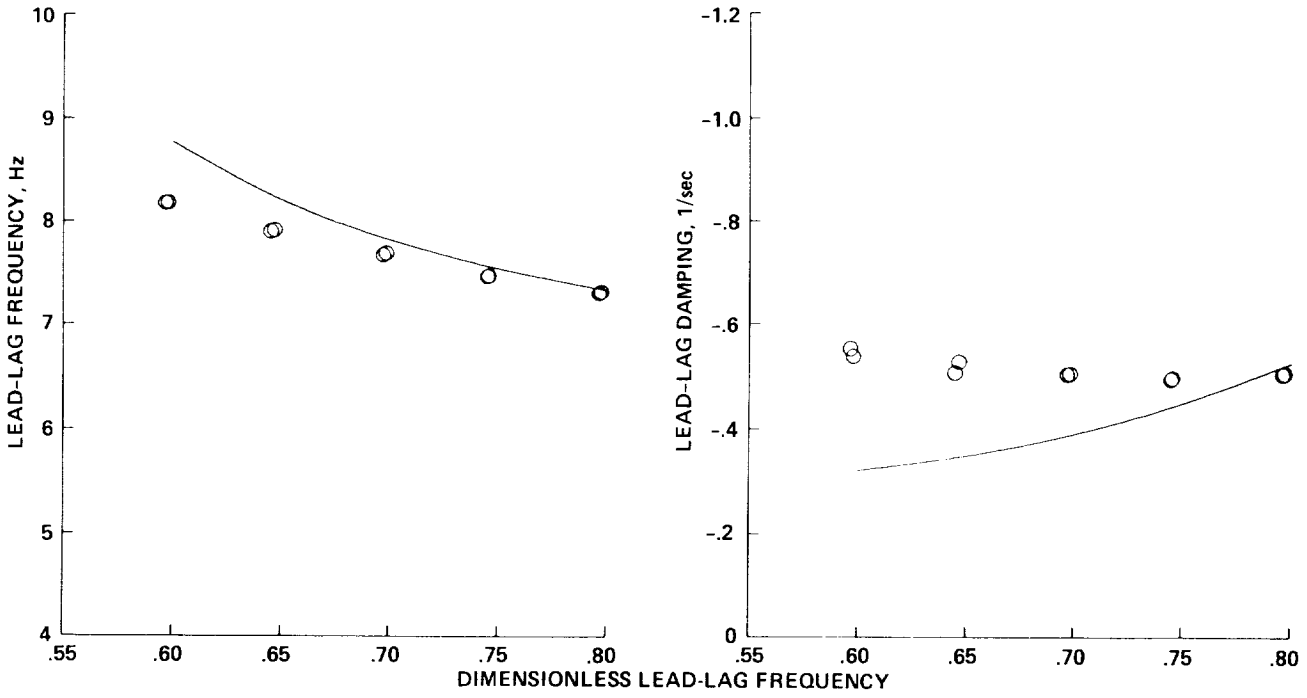

(b) $\theta_h = 18°$.

Figure 13.– Lead-lag frequency and damping for straight flap/straight lead-lag flexures (configuration one) as functions of nondimensional lead-lag frequency, $\theta_h = 0°$.

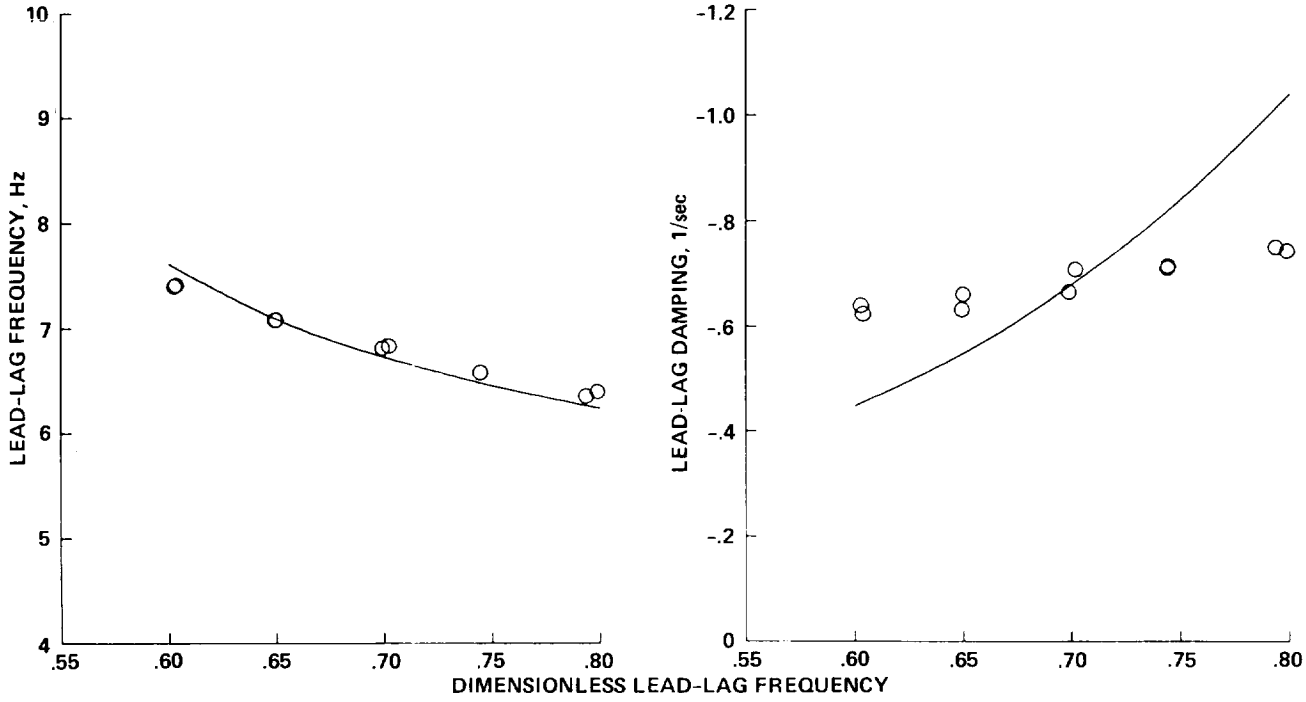

(c) $\theta_h = 36°$.

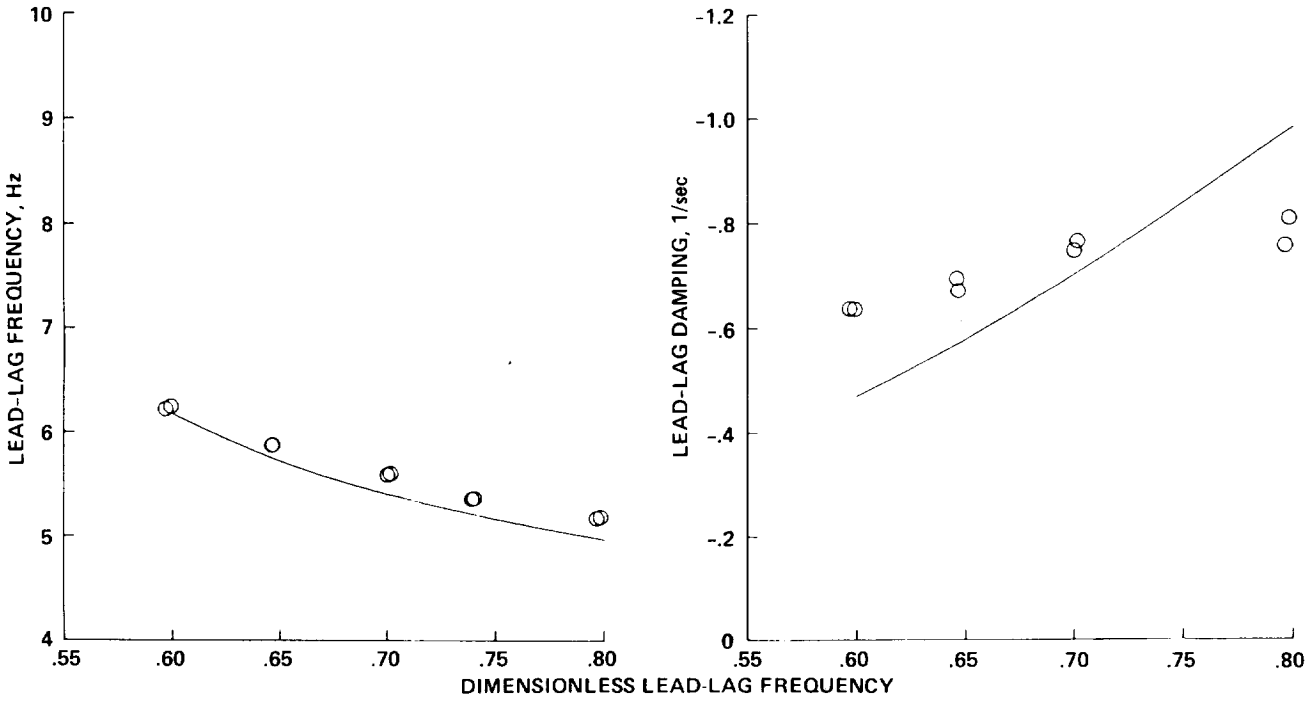

(d) $\theta_h = 54°$.

Figure 13.– Concluded.

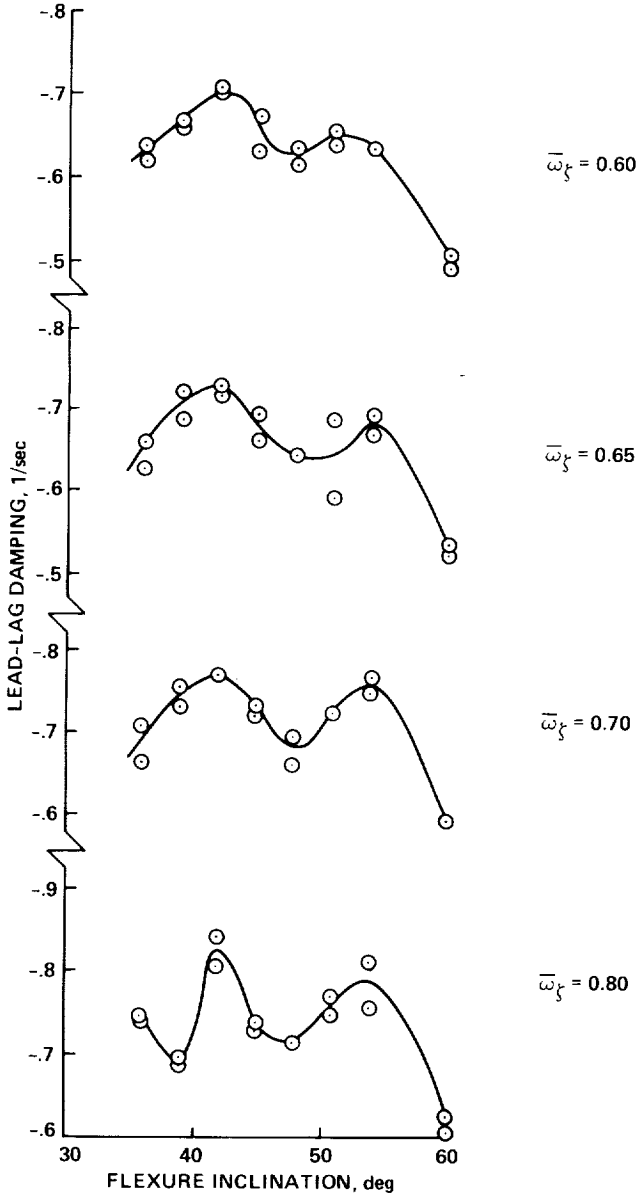

Figure 14.– Variation in damping with flexure inclination for straight flap and straight lead-lag flexure (configuration one), $\theta_b = 0°$. The curve shown is faired through the data.

provide negative pitch-lag coupling, $\theta_\zeta = -0.41$. This configuration was tested for nondimensional lead-lag frequencies of 0.60 to 0.80 and pitch angles from 0° to 9°. At $\bar{\omega}_\zeta = 0.70$ the effect of blade pitch angle is strongly stabilizing, as shown in figure 16. The data show the same trend as the theoretical prediction, but they do not show good agreement with the theory at high and low pitch angles. In figure 17, theory and experiment are compared for frequency and damping as functions of the nondimensional lead-lag frequency. The agreement in this case is poor.

Pitch-Flap Coupling

The skewed flap/straight lead-lag flexure set (configuration three) was tested to investigate the effects of pitch-flap coupling alone. The flexure inclination was kept at 0° to avoid flap-lag coupling. The effect of the skewed flap flexure is to cause positive pitch-flap coupling, $\theta_\beta = 0.29$. The damping as a function of blade pitch angle is shown in figure 18. The effect of the blade pitch angle is to increase the lead-lag damping. The theoretical trend shows much the same behavior as the measurements, but predicts a lower value of the damping. A comparison of this configuration with the straight flap/straight lead-lag flexures (configuration one) shown in figure 15(a) shows nearly identical behavior. This suggests that the effects of pitch-flap coupling on the lead-lag damping are slight and the residual pitch-flap coupling that occurs on the skewed flap/skewed lead-lag flexures (configuration four) at flexure inclinations away from 36° (see fig. 6) will have little or no effect on the lead-lag damping for that configuration.

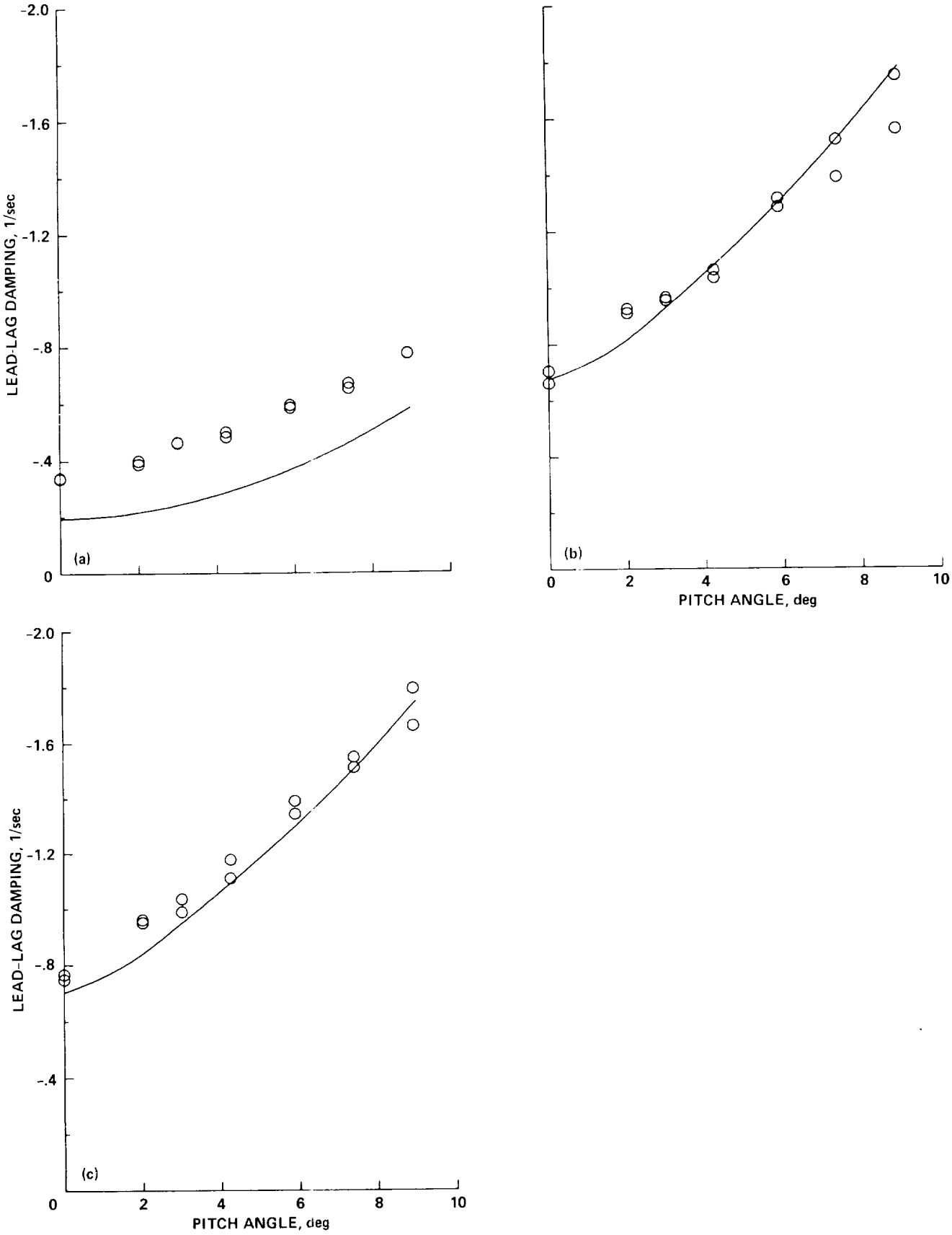

Figure 15.– Lead-lag damping as a function of blade pitch angle for straight flap/straight lead-lag flexures (configuration one), $\bar{\omega}_\zeta = 0.7$. (a) $\theta_h = 0°$, (b) $\theta_h = 36°$, (c) $\theta_h = 54°$.

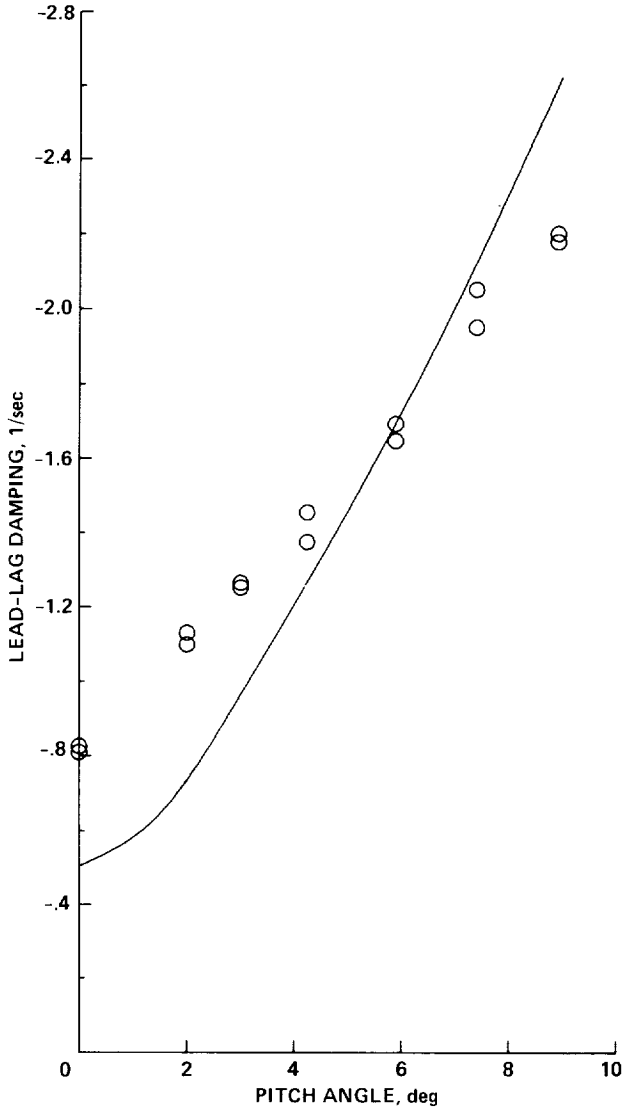

Figure 16.– Lead-lag damping as a function of blade pitch for straight flap and skewed lead-lag flexures (configuration two); $\theta_h = 0°, \bar{\omega}_\zeta = 0.70, \theta_\zeta = -0.41, \theta_\beta = 0.0$.

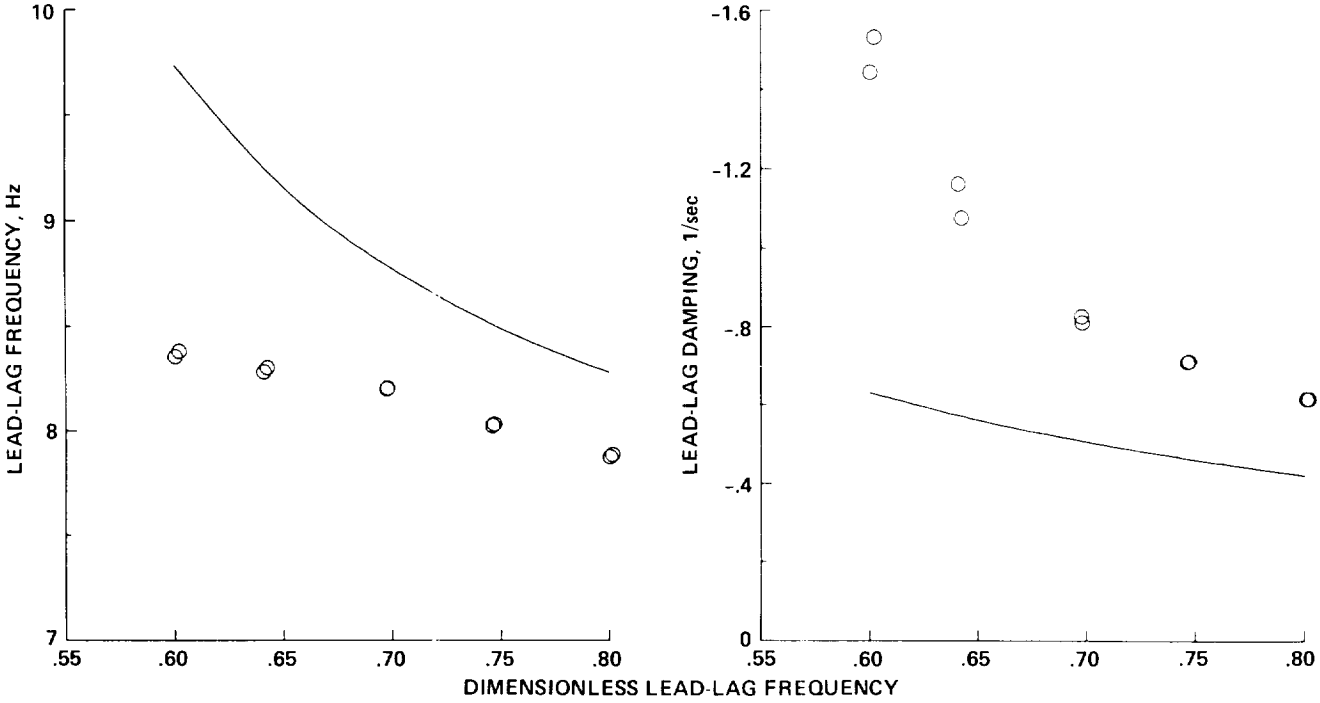

Figure 17.– Lead-lag frequency and damping as a function of nondimensional frequency for straight flap/skewed lead-lag flexures (configuration two); $\theta_h = 0°, \theta_b = 0°, \theta_\zeta = -0.41, \theta_\beta = 0.0$.

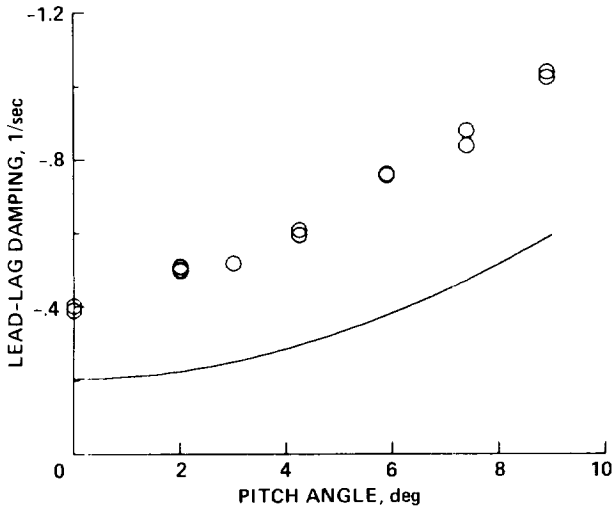

Figure 18.– Lead-lag damping as a function of blade pitch angle for skewed flap/straight lead-lag flexure (configuration three); $\bar{\omega}_\zeta = 0.70, \theta_h = 0°, \theta_\zeta = 0.0, \theta_\beta = 0.29$.

Structural Flap-Lag Coupling and Pitch-Lag Coupling in Combination

Effects of flexure inclination and the flap-lag stiffness difference at zero pitch angle–The skewed flap/skewed lead-lag flexures (configuration four) were tested to examine the effects of structural flap-lag and pitch-lag coupling in combination. The effects of structural flap-lag coupling are caused both by the flexure inclination and the difference in stiffness between the flap and lead-lag degrees of freedom as discussed earlier in the section on the effects of flap-lag coupling alone. The effect of pitch-lag coupling is to accentuate the flap-lag coupling as can be seen in the expanded form of equation (1) shown here:

$$K = \frac{\mathcal{R}}{2\Delta}\left(\frac{K_\zeta}{I\Omega^2} - \frac{K_\beta}{I\Omega^2}\right)\sin 2\theta_h \times \left[\frac{\mathcal{R}}{2\Delta}\left(\frac{K_\zeta}{I\Omega^2} - \frac{K_\beta}{I\Omega^2}\right)\sin 2\theta_h - \frac{\gamma}{8}\theta_\zeta\right]$$

Within the brackets, the flap-lag and pitch-lag coupling terms are additive; their sum then multiplies the effect of flap-lag coupling alone. The pitch-lag coupling varies only slightly as flexure inclination is changed for configuration four (see fig. 6); therefore, the primary influence on lead-lag damping for this configuration is caused by the flap-lag coupling induced by the flexure inclination and the rotor speed (through its effect upon the nondimensional stiffness term). The effects of flexure inclination and the nondimensional stiffness difference were examined by varying the flexure angle and the rotor speed while fixing the blade pitch angle at zero. The rotor speed was selected to give a constant value of the nondimensional lead-lag frequency for all flexure inclinations.

The effect of flexure inclination is shown in figure 19 where the lead-lag frequency and damping are shown as functions of flexure inclination for three values of nondimensional lead-lag frequency. In all cases the effect of flexure inclination is to increase the lead-lag damping until a maximum is reached at about 40° for the experimental data and at about 30° for the predictions. This behavior is similar to that of the configuration with flap-lag coupling alone (see fig. 12), except that the damping level is about four times higher for the configuration here. The theoretical predictions show that the increase in damping with flexure inclination is greater for the higher values of nondimensional lead-lag frequency (lower rotor speed), but the measured increase is similar regardless of the nondimensional lead-lag frequency.

The effect of the nondimensional stiffness term is shown in figure 20 where the damping and frequency are shown as functions of the nondimensional lead-lag frequency for five values of flexure inclination. The effect is slight for small flexure inclination, but becomes more significant as the flexure inclination is increased. A comparison of the theory and the data in figures 19 and 20 shows similar trends, but some substantial differences as well. Except at the highest values of the nondimensional lead-lag frequency, the measured lead-lag damping is much higher than the calculated damping. It will be shown in the following section that this difference occurs only at blade pitch angles or rotor thrust levels near zero.

Effects of pitch angle on lead-lag damping– The lead-lag damping as a function of pitch angle is shown in figure 21 for flexure inclinations of 0°, 18°, 36°, 51°, and 60° for a nondimensional lead-lag frequency of 0.70. The damping as a function of the pitch angle is shown in figure 22 for nondimensional lead-lag frequencies of 0.60, 0.70, and 0.80 for a flexure inclination of 36°. Two major features are seen in comparing the measurements with the theoretical predictions. First, the general effect of blade pitch angle is to increase the damping as the angle increases. Second, at flexure inclinations of 36°, 51°, and 60° there is a noticeable difference between the behavior of the data and the predictions at low blade-pitch angles. In general, for pitch angles from −2° to +2° the measured damping is significantly higher than the predictions; there is the appearance in the figure of a "hump" or "bump" around the zero pitch angle. This behavior is also

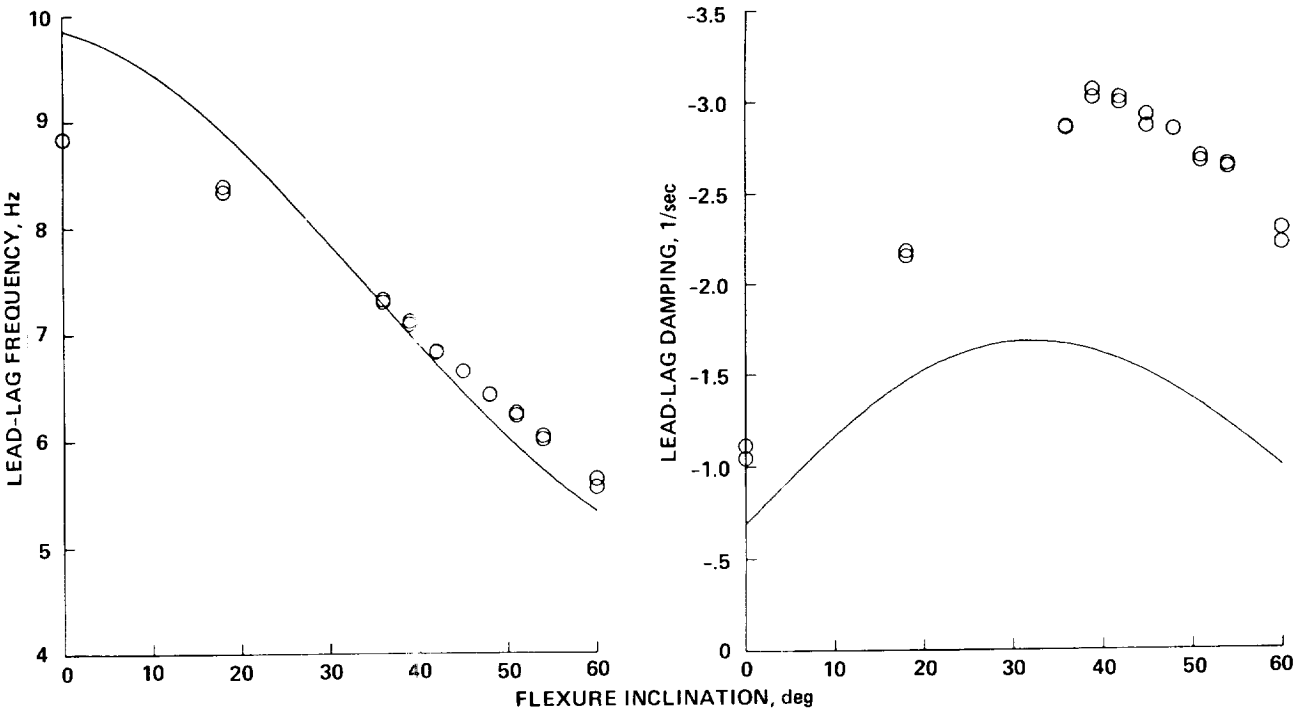

(a) $\bar{\omega}_\zeta = 0.60$.

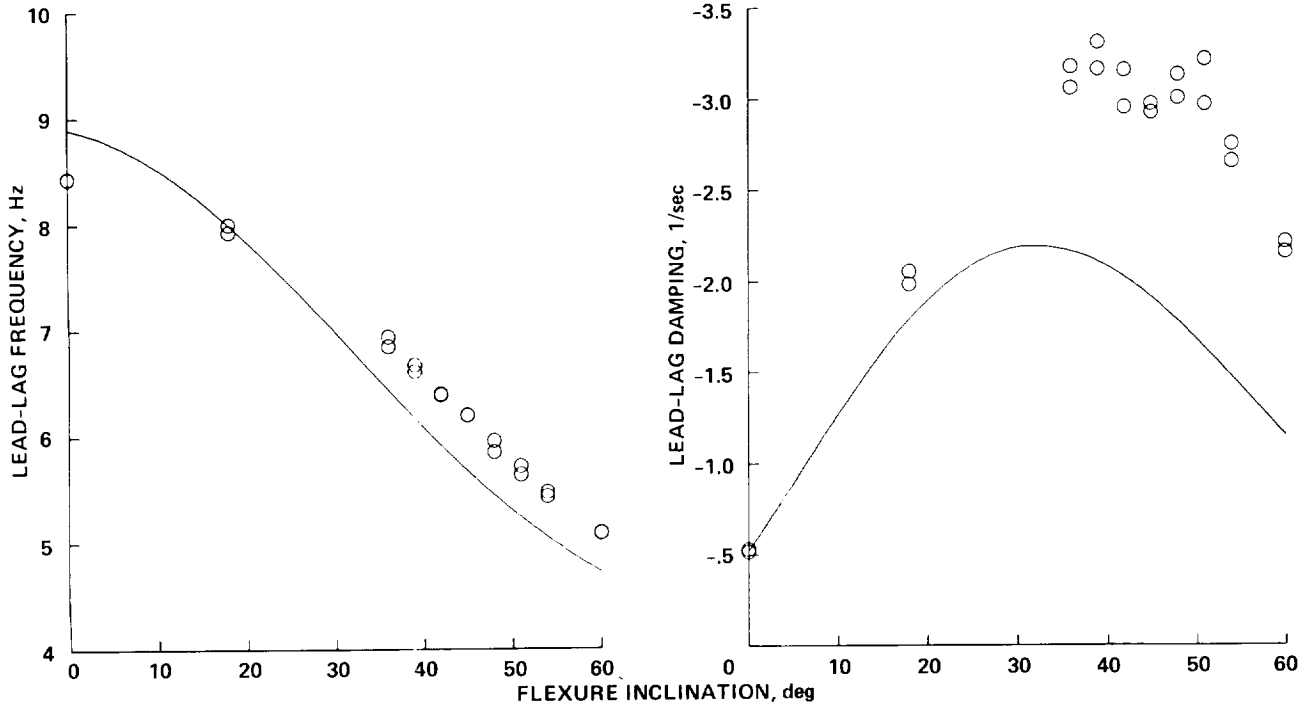

(b) $\bar{\omega}_\zeta = 0.70$.

Figure 19.– Lead-lag frequency and damping as functions of flexure inclination for the skewed flap/skewed lead-lag flexure (configuration four), $\theta_b = 0°$.

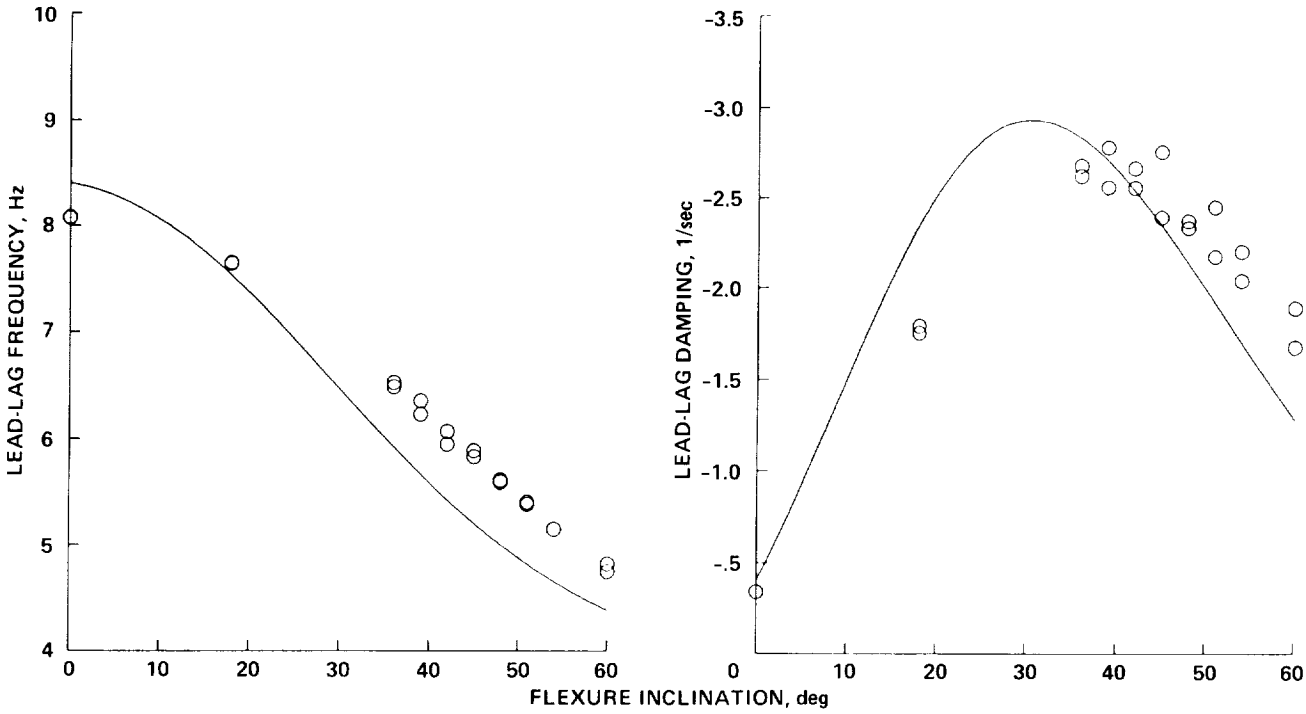

(c) $\bar{\omega}_\zeta = 0.80$.

Figure 19.– Concluded.

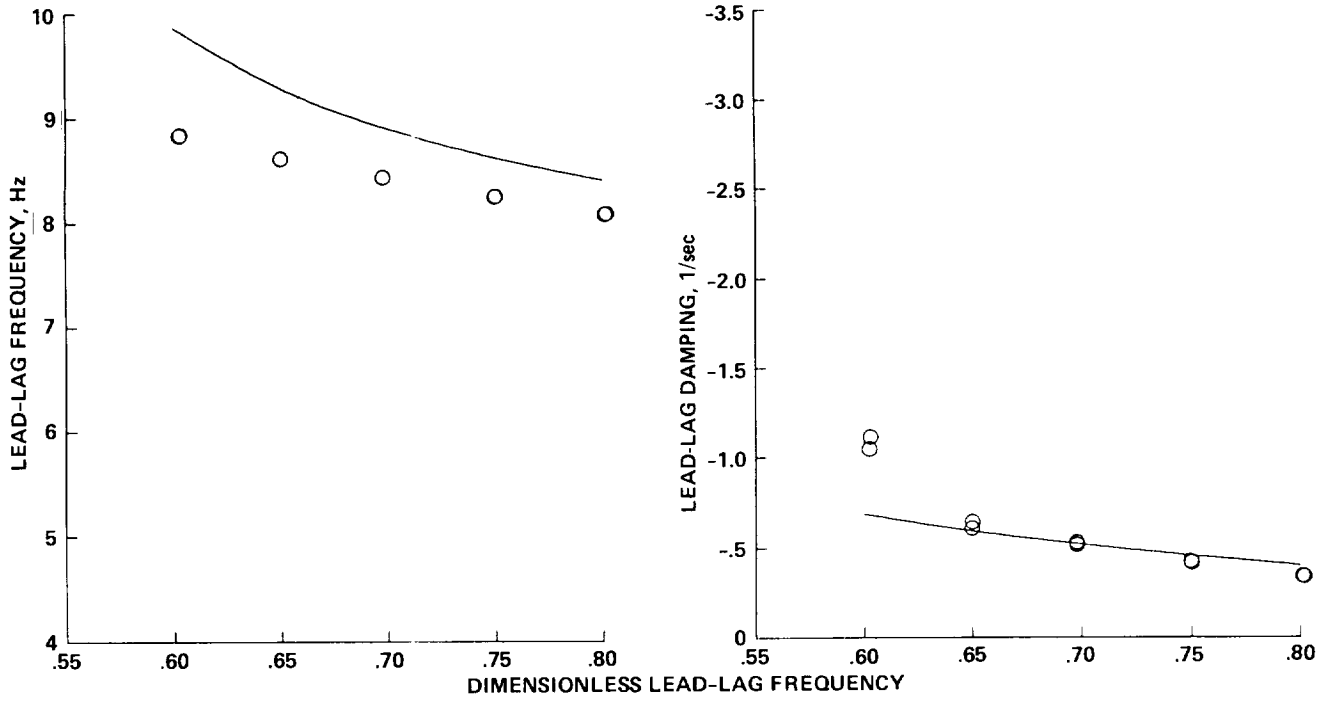

(a) $\theta_h = 0°$.

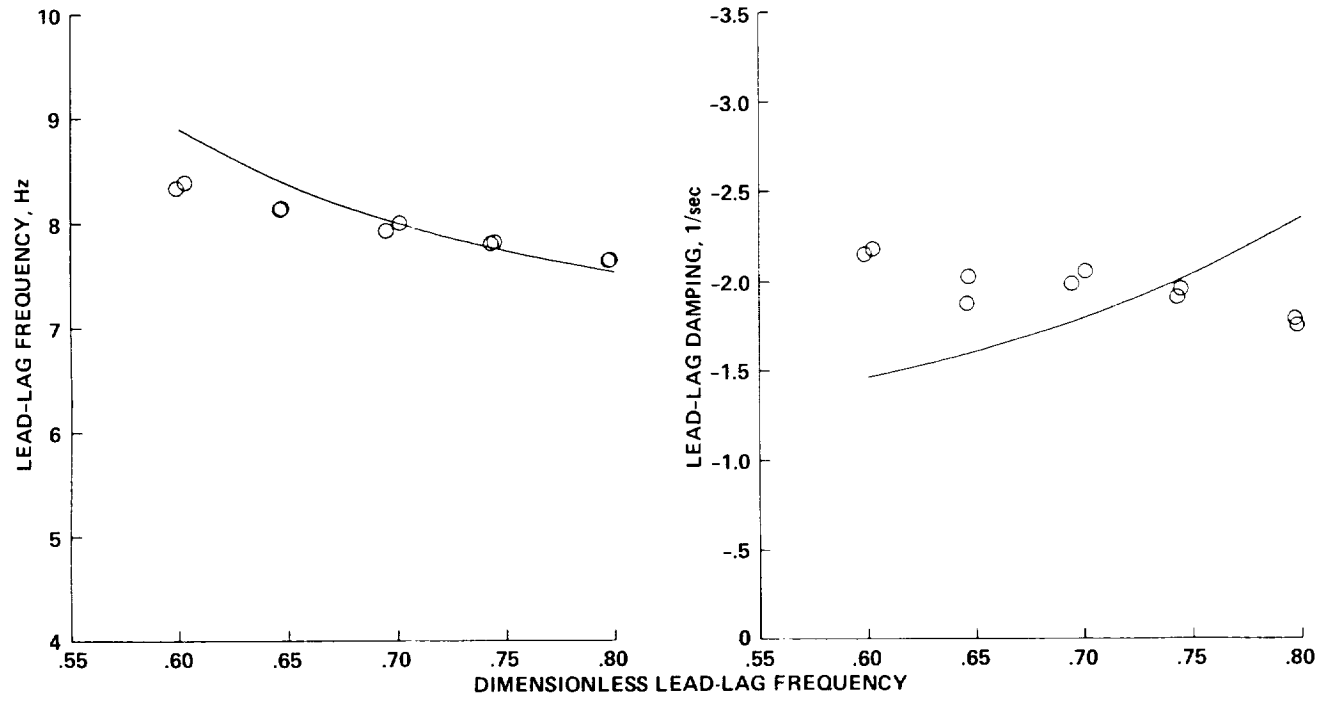

(b) $\theta_h = 18°$.

Figure 20.– Lead-lag frequency and damping as functions of nondimensional frequency for the skewed flap/skewed lead-lag flexure (configuration four), $\theta_b = 0°$.

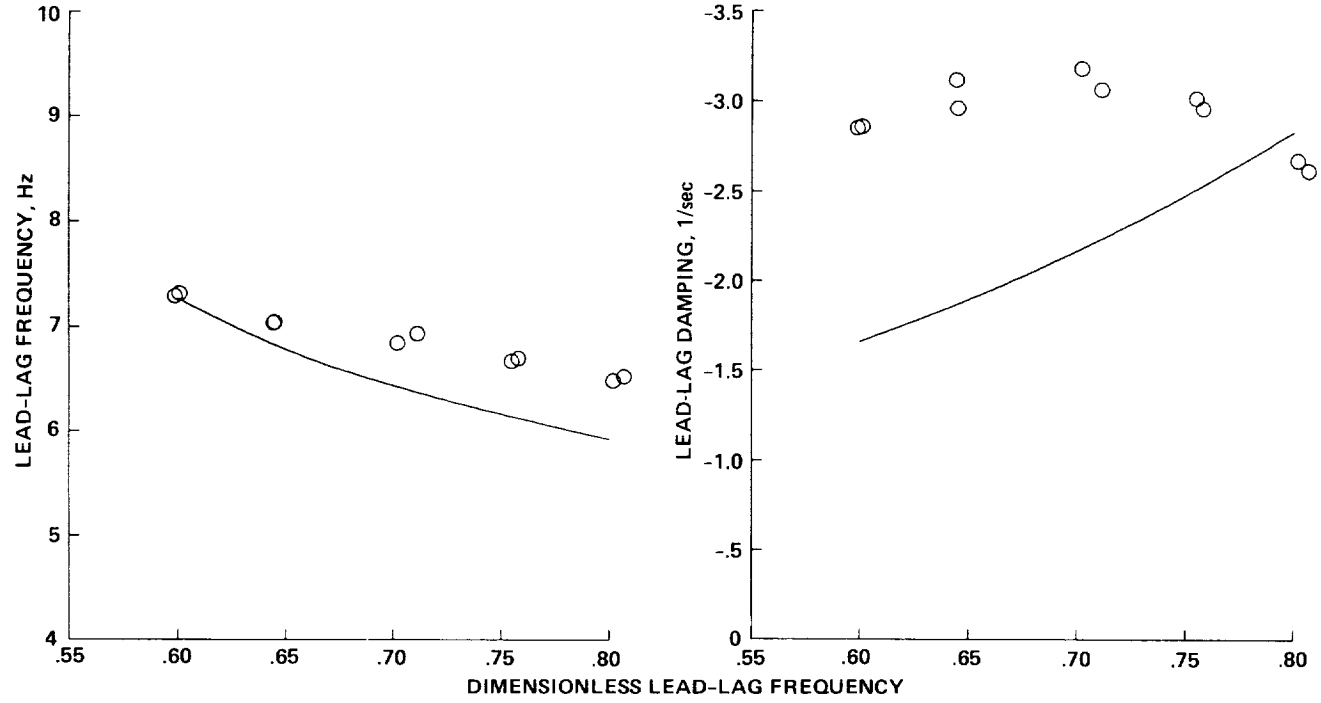

(c) $\theta_h = 36°$.

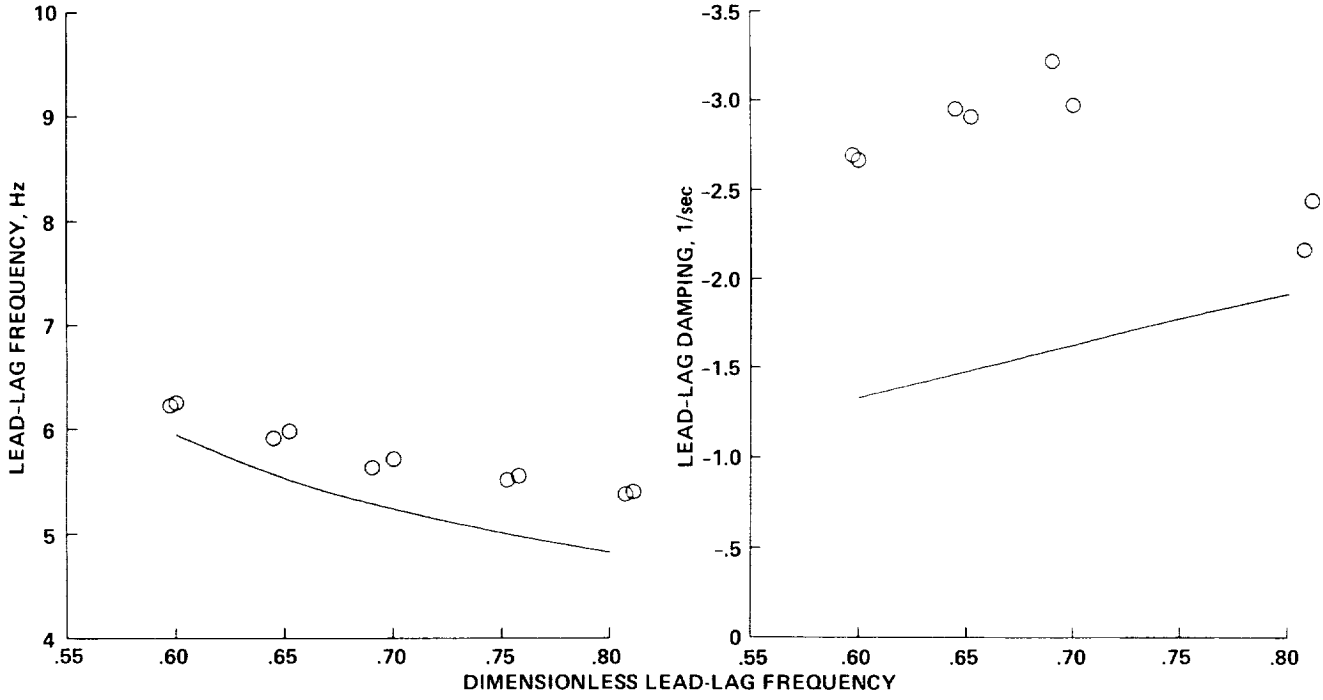

(d) $\theta_h = 51°$.

Figure 20.– Continued.

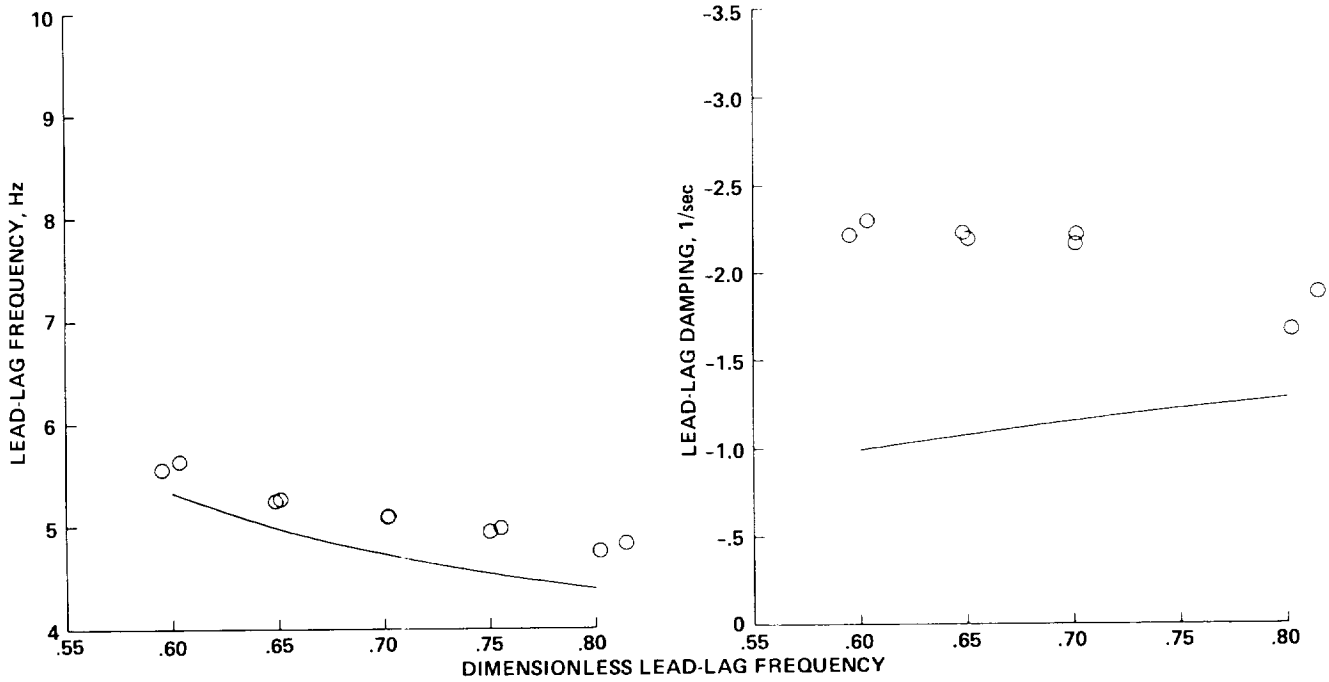

(e) $\theta_h = 60°$.

Figure 20.– Concluded.

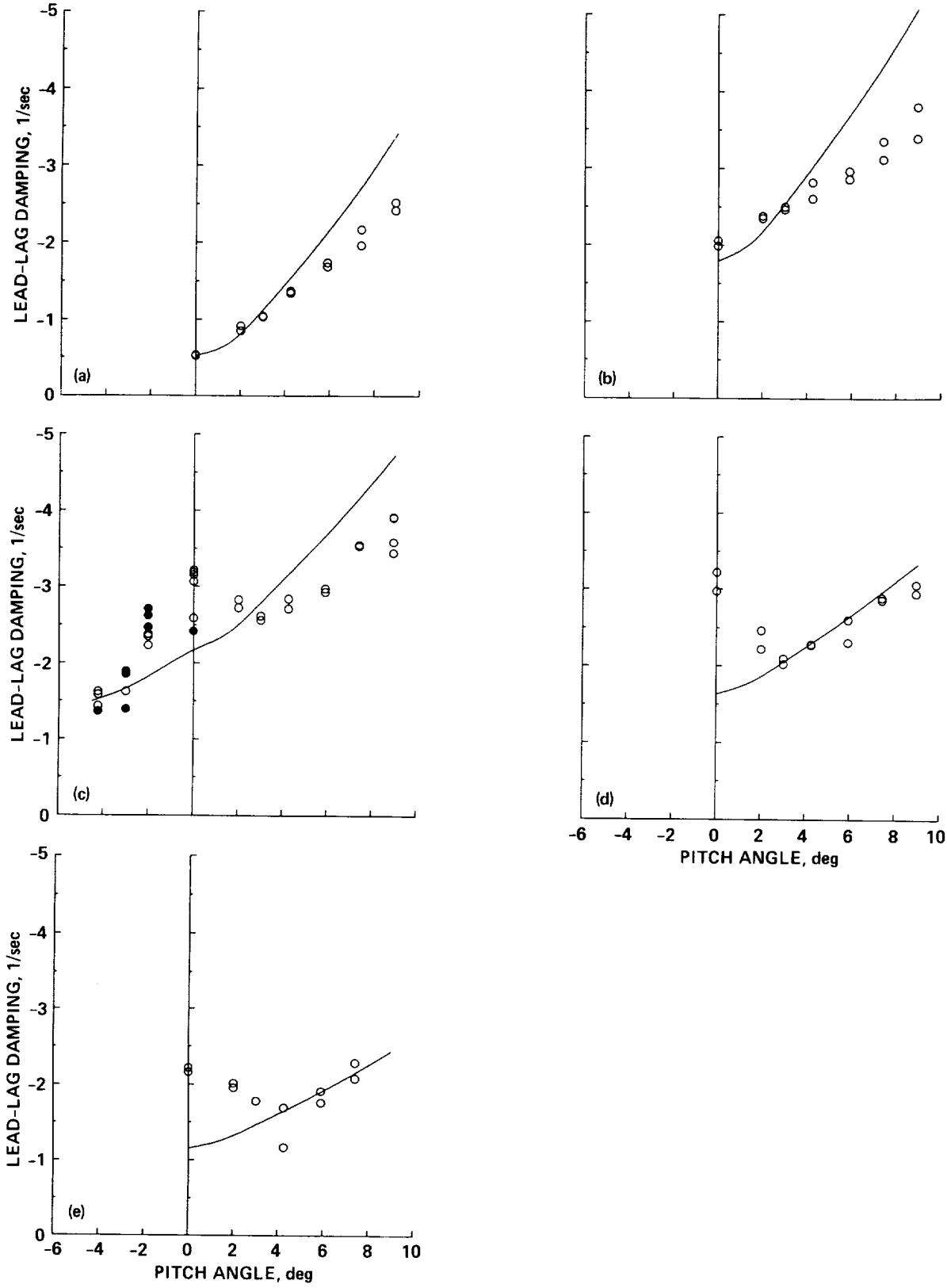

Figure 21.– Lead-lag damping as a function of blade pitch angle for the skewed flap/skewed lead-lag flexure (configuration four); $\bar{\omega}_\zeta = 0.70$. Excitation at $\Omega - \omega_\zeta$ shown by solid symbols. (a) $\theta_h = 0°$, (b) $\theta_h = 18°$, (c) $\theta_h = 36°$, (d) $\theta_h = 51°$, (e) $\theta_h = 60°$.

apparent at other nondimensional lead-lag frequencies as shown in figure 22. The difference in damping at low pitch angle or low thrust that is seen here is the same difference noted at nondimensional frequencies of 0.60 and 0.70 in figures 19(a) and 19(b).

The damping data shown in figures 21 and 22 for pitch angles less than zero were obtained in the second experiment. In addition, the effect of the forcing frequency was studied experimentally by exciting the rotor at a frequency of $\Omega - \omega_\zeta$ as well as at the $\Omega + \omega_\zeta$ frequency that had been used in the first experiment. Excitation at a frequency of $\Omega - \omega_\zeta$ is shown by the solid symbols in figures 21 and 22; no significant difference is observed following excitation at these different fixed-system frequencies.

A comparison of the theoretical predictions and the measurements in figures 21 and 22 shows reasonable agreement in the general trends. However, the theory does not show the hump in the damping that was measured for pitch angles near 0°, and this discrepancy remains unexplained. The theory and experiment show good agreement in damping level except for the case of $\bar{\omega}_\zeta = 0.80$, in which the theoretical prediction is substantially higher.

Comparison of the Effects of Flap-Lag, Pitch-Lag, and Pitch-Flap Coupling on Lead-Lag Damping

In figure 23, the lead-lag damping of the four test configurations described in table 2 is compared for a nondimensional lead-lag frequency of 0.70. Configuration one, with zero flexure inclination, represents a rotor without coupling. As shown in figure 23(a), the damping is very low at a pitch angle of 0°, and increases slowly with pitch angle. If the flexures are inclined to 36° for configuration one, this causes structural flap-lag coupling and the zero-pitch-angle damping jumps from about –0.3 to –0.6 sec^{-1}. The damping increase with pitch angle is greater for this case than for the uncoupled case. Configuration two includes pitch-lag coupling but no flap-lag coupling (fig. 23(b)). Its behavior is similar to that of flap-lag coupling alone, although in this case the theory predicts a more rapid increase with pitch angle than was measured in the experiment. Configuration three includes pitch-flap coupling alone and, as shown in figure 23(b), both calculation and measurement are very similar to those for the uncoupled case. Configuration four includes structural flap-lag and pitch-lag coupling in combination and the damping is substantially higher than that for configurations with flap-lag or pitch-lag coupling alone.

The predictions of the mathematical model show good agreement with the measurements as concerns the effects of the various couplings, with the exception of the low-pitch-angle or low-thrust data of configuration four. The cause of this discrepancy is unknown.

CONCLUSIONS

The major conclusions of this experimental investigation are:

1. For configuration one (straight flap and straight lag flexures), with structural flap-lag coupling alone, and a blade pitch angle of zero, the lead-lag damping increases with flexural angle, and reaches a maximum at about an inclination of 54°. The damping is also strongly influenced by the difference in nondimensional lead-lag and flap stiffnesses, $\bar{\omega}_\zeta^2 - \bar{\omega}_\beta^2$, being greater for larger values of the stiffness difference term, and reduced for smaller values of $\bar{\omega}_\zeta^2 - \bar{\omega}_\beta^2$. These trends agree qualitatively with theory.
2. For configuration one, with structural flap-lag coupling alone, the effect of pitch angle at $\bar{\omega}_\zeta = 0.70$ is to strongly increase the lead-lag damping at large flexure inclinations. At zero flexure inclination the stabilizing effect of pitch angle is much less. Theory and experiment show good agreement in this case.
3. For configuration one, with structural flap-lag coupling alone, the data show two maxima in the range of flexure inclinations from

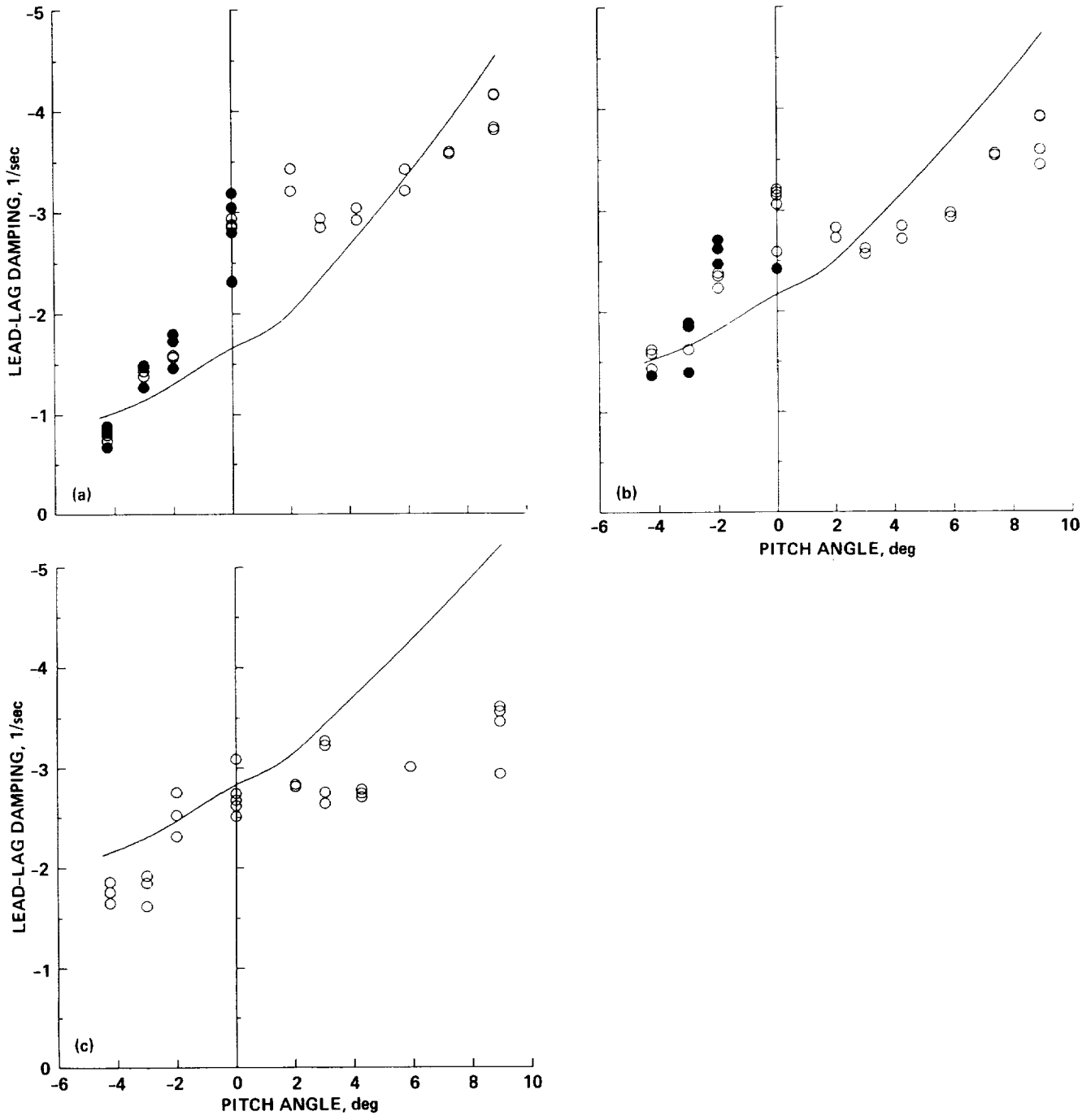

Figure 22.– Lead-lag damping as a function of blade pitch angle for the skewed flap/skewed lead-lag flexure (configuration four); $\theta_h = 36°$. Excitation at $\Omega - \omega_\zeta$ shown by solid symbols. (a) $\bar{\omega}_\zeta = 0.60$, (b) $\bar{\omega}_\zeta = 0.70$, (c) $\bar{\omega}_\zeta = 0.80$.

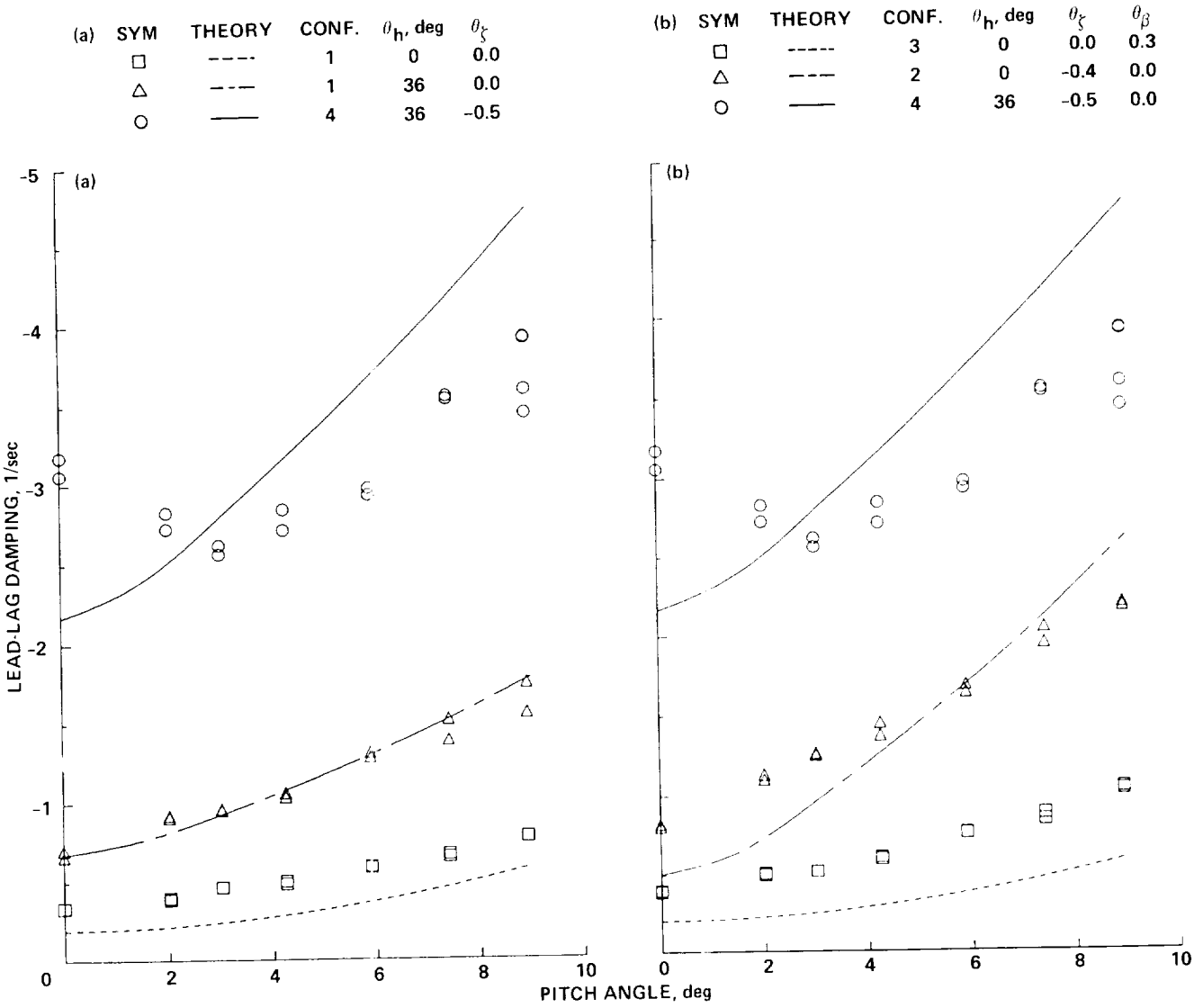

Figure 23.– Lead-lag damping as a function of blade pitch angle, $\bar{\omega}_\zeta = 0.70$. (a) Comparison of combined pitch-lag and flap-lag coupling (configuration four), flap-lag coupling alone (configuration one with flexure inclination of 36°), and no coupling (configuration one with zero flexure inclination). (b) Comparison of combined pitch-lag coupling (configuration four), pitch-lag coupling alone (configuration two), and pitch-flap coupling alone (configuration three).

45° to 55°. The theory predicts only a single maximum.

4. For configuration two (straight flap and skewed lead-lag flexures), with pitch-lag coupling alone, pitch angle has a strong stabilizing effect on the lead-lag damping. The theory shows the same effect and gives good qualitative agreement.
5. For configuration three (skewed flap and straight lead-lag flexures), with pitch-flap coupling alone, no significant differences are seen from the uncoupled rotor. This result is also shown by the theoretical calculations.
6. For configuration four (skewed flap and skewed lead-lag flexures), which combines structural flap-lag and pitch-lag coupling, there is a rapid increase in lead-lag damping at zero blade-pitch angle as the flexure inclination is increased. A maximum in damping is reached at about 40°. Qualitatively, this behavior is similar to that in the case of flap-lag coupling alone, but the damping is three to five times greater.
7. For configuration four the peak lead-lag damping achieved is considerably higher than the theoretical prediction at zero blade pitch angle. When the damping is examined as a function of blade pitch angle, it is seen that within 2° or 3° of zero blade pitch angle the measured damping is higher than predicted.
8. It is shown experimentally in appendix C that coupling between the rotor lead-lag degrees of freedom and the stand can have a substantial effect on both the lead-lag frequency and the damping. It is shown empirically that the first cantilever modes of the test stand must be two and one-half to three times greater than the fixed-system lead-lag mode frequency of $\Omega + \omega_\zeta$ to avoid the effects of this coupling. This criterion was not met in the present experiment, resulting in some errors in frequency and damping. The size of these errors is unknown.

Ames Research Center
National Aeronautics and Space Administration
Moffett Field, CA 94035-1000, November 1, 1989

APPENDIX A

THEORETICAL MODEL

As discussed in the section on Experiment Design, it was desired that the experimental model match the theoretical model as closely as possible. Specifically, it was desired that the hinge offset be as close to zero as possible. However, the resulting design value of 0.105 was too high and had a significant effect upon the blade rotating frequencies. The equations of motion used in reference 4, therefore, were rederived to include equal offset in the flap and lead-lag hinges. In addition, the two-spring model of reference 4 which uses one spring set to represent the blade and a second spring set to represent the hub was replaced with a three-spring model. The additional spring set represents the flexures, which may have any inclination independent of the hub or the blade. A tip-loss correction was added to the blade aerodynamics in the rederived equations.

The rotor model used in reference 4 was discussed briefly in the Experimental Design section; see also figure 2. The model used for correlation here is shown in figure 24. The three sets of springs shown in the figure represent the small flexibility of the fixed hub of the present model rotor, the flexure flexibility, and the flexibility of the very stiff blades.

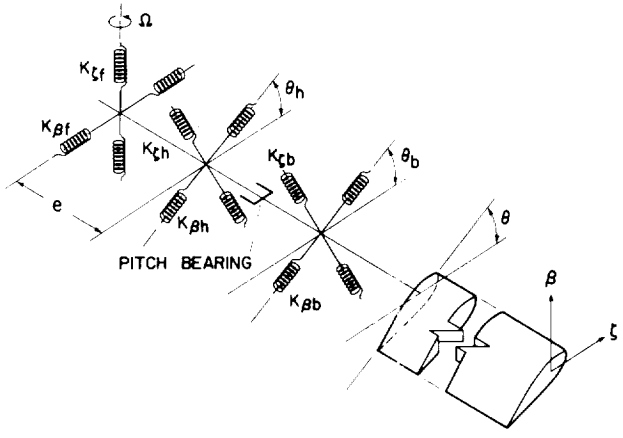

Figure 24.– Three-spring model of blade flexibility.

The flexure spring set and the blade spring set may be rotated in pitch to introduce flap-lag structural coupling. The flexure spring set inclination is represented by the angle θ_h while the blade spring set is fixed to the blade and has the same inclination as the blade pitch angle, θ_b. The two outer spring sets are shown offset from each other for illustrative purposes; mathematically they are considered coincident. The equations of motion are derived assuming the blade lags first, then flaps. This lag-flap sequence corresponds to the design of the model, as can be seen in figure 4. However, as the flexure inclination increases from 0° to 90°, the experimental hub transitions from a lag-flap sequence to a flap-lag sequence. Some of the terms in the equations of motion for a flap-lag sequence will change (ref. 10), but that effect is not included here. In addition, the equations do not account for the effects of the skewed flexures on inertial coupling terms.

Modified Equilibrium Equations

The modified equations were obtained from reference 5.

$$\begin{bmatrix} F_\beta & F_\zeta \\ C_\beta & C_\zeta \end{bmatrix} \begin{Bmatrix} \beta_o \\ \zeta_o \end{Bmatrix} = \begin{Bmatrix} F_o \\ C_o \end{Bmatrix} \qquad (A1)$$

where

$$F_\beta = 1 + \frac{3}{2}\frac{e}{(1-e)} + \frac{1}{\Delta}\left[\bar{\omega}_{\beta o}^2 + \bar{\omega}_\Delta^2\left(\mathcal{R}_b \sin^2\theta_b + \mathcal{R}_h \sin^2\theta_h\right)\right] \qquad (A2)$$

$$F_\zeta = C_\beta = \frac{\bar{\omega}_\Delta^2}{2\Delta}\left(\mathcal{R}_b \sin 2\theta_b + \mathcal{R}_h \sin 2\theta_h\right) \qquad (A3)$$

$$C_\zeta = \frac{3}{2}\frac{e}{(1-e)} + \frac{1}{\Delta}\left[\bar{\omega}_{\zeta o}^2 - \bar{\omega}_\Delta^2(\mathcal{R}_b \sin^2\theta_b + \mathcal{R}_h \sin^2\theta_h)\right] \quad (A4)$$

$$F_o = \frac{\gamma B^4}{8a}\left(c_{l_o} - \phi_i c_{d_o}\right)\left(1 - \frac{4}{3}\frac{e}{B}\right) - \frac{g m_b r_{cg}}{I\Omega^2} \quad (A5)$$

$$C_o = -\frac{\gamma B^4}{8a}\left(c_{d_o} + \phi_i c_{l_o}\right)\left(1 - \frac{4}{3}\frac{e}{B}\right) \quad (A6)$$

and

$$\bar{\omega}_\Delta^2 = \bar{\omega}_{\zeta o}^2 - \bar{\omega}_{\beta o}^2 \quad (A7)$$

$$\Delta = 1 + \frac{\bar{\omega}_\Delta^4}{\bar{\omega}_{\zeta o}^2 \bar{\omega}_{\beta o}^2}\left[\mathcal{R}_b(1-\mathcal{R}_b)\sin^2\theta_b + \mathcal{R}_h(1-\mathcal{R}_h)\sin^2\theta_h - \mathcal{R}_b\mathcal{R}_h\left(2\sin^2\theta_b \sin^2\theta_h + \frac{1}{2}\sin 2\theta_b \sin 2\theta_h\right)\right] \quad (A8)$$

$$\bar{\omega}_{\beta o}^2 = \frac{K_\beta}{I\Omega^2}; \quad \bar{\omega}_{\zeta o}^2 = \frac{K_\zeta}{I\Omega^2} \quad (A9)$$

$$K_\beta = \frac{K_{\beta b} K_{\beta h} K_{\beta f}}{K_{\beta h} K_{\beta f} + K_{\beta b} K_{\beta f} + K_{\beta b} K_{\beta h}} \quad (A10)$$

$$K_\zeta = \frac{K_{\zeta b} K_{\zeta h} K_{\zeta f}}{K_{\zeta h} K_{\zeta f} + K_{\zeta b} K_{\zeta f} + K_{\zeta b} K_{\zeta h}} \quad (A11)$$

$$\mathcal{R}_{\beta b} = K_\beta / K_{\beta b}; \quad \mathcal{R}_{\zeta b} = K_\zeta / K_{\zeta b} \quad (A12)$$

$$\mathcal{R}_b = \frac{\bar{\omega}_{\zeta o}^2 \mathcal{R}_{\beta b} - \bar{\omega}_{\beta o}^2 \mathcal{R}_{\zeta b}}{\bar{\omega}_{\zeta o}^2 - \bar{\omega}_{\beta o}^2} \quad (A13)$$

$$\mathcal{R}_{\beta h} = K_\beta / K_{\beta h}; \quad \mathcal{R}_{\zeta h} = K_\zeta / K_{\zeta h} \quad (A14)$$

$$\mathcal{R}_h = \frac{\bar{\omega}_{\zeta o}^2 \mathcal{R}_{\beta h} - \bar{\omega}_{\beta o}^2 \mathcal{R}_{\zeta h}}{\bar{\omega}_{\zeta o}^2 - \bar{\omega}_{\beta o}^2} \quad (A15)$$

$$\phi_i = \sqrt{\frac{\sigma c_{l_o}}{6}} \quad (A16)$$

The steady moment due to blade weight has been added to the equilibrium equations for correlation with model-scale data.

Modified Perturbation Equations

$$\begin{bmatrix} s^2 + F_{\dot\beta}s + F_\beta & F_{\dot\zeta}s + F_\zeta \\ C_{\dot\beta}s + C_\beta & s^2 + C_{\dot\zeta}s + C_\zeta \end{bmatrix} \begin{Bmatrix} \Delta\beta \\ \Delta\zeta \end{Bmatrix} = \begin{Bmatrix} F_{\Delta\theta} \\ C_{\Delta\theta} \end{Bmatrix} \Delta\theta + \begin{Bmatrix} F_{\Delta\theta b} \\ C_{\Delta\theta b} \end{Bmatrix} \Delta\theta_b + \begin{Bmatrix} F_{\Delta\theta h} \\ C_{\Delta\theta h} \end{Bmatrix} \Delta\theta_h \quad (A17)$$

where

$$F_{\dot\beta} = -\frac{\gamma B^4}{8a}\left(\phi_i c_{d_\alpha} - c_{l_\alpha} - c_{d_o}\right)\left(1 - \frac{8}{3}\frac{e}{B}\right) \quad (A18)$$

$$F_{\dot\zeta} = -\frac{\gamma B^4}{8a}\left[2c_{l_o} + \phi_i(c_{l_\alpha} - \phi_i c_{d_\alpha} - c_{d_o})\right] \times \left(1 - \frac{8}{3}\frac{e}{B}\right) + 2\beta_o \quad (A19)$$

$$C_{\beta} = \frac{\gamma B^4}{8a}\left(c_{l_o} - \phi_i c_{l_\alpha} - c_{d_\alpha}\right)\left(1 - \frac{8}{3}\frac{e}{B}\right) - 2\beta_o \qquad (A20)$$

$$C_{\zeta} = \frac{\gamma B^4}{8a}\left[2c_{d_o} + \phi_i(c_{l_o} + c_{d_\alpha} + \phi_i c_{l_\alpha})\right] \times \left(1 - \frac{8}{3}\frac{e}{B}\right) + 2\eta_m\bar{\omega}_{\zeta o} \qquad (A21)$$

$$F_{\Delta\theta} = \frac{\gamma B^4}{8a}\left(c_{l_\alpha} - \phi_i c_{d_\alpha}\right)\left(1 - \frac{4}{3}\frac{e}{B}\right) \qquad (A22)$$

$$C_{\Delta\theta} = -\frac{\gamma B^4}{8a}\left(c_{d_\alpha} + \phi_i c_{l_\alpha}\right)\left(1 - \frac{4}{3}\frac{e}{B}\right) \qquad (A23)$$

$$F_{\Delta\theta b} = -\frac{\bar{\omega}_\Delta^2 \mathcal{R}_b}{\Delta}\left\{\left[sin2\theta_b - \mathcal{R}_{wb}\left(F_\beta - 1 - \frac{3}{2}\frac{e}{(1-e)}\right)\right]\beta_o - (\mathcal{R}_{wb}F_\zeta - cos2\theta_b)\zeta_o\right\} \qquad (A24)$$

$$C_{\Delta\theta b} = -\frac{\bar{\omega}_\Delta^2 \mathcal{R}_b}{\Delta}\left\{(cos2\theta_b - \mathcal{R}_{wb}F_\zeta)\beta_o - \left[sin2\theta_b + \mathcal{R}_{wb}\left(C_\zeta - \frac{3}{2}\frac{e}{(1-e)}\right)\right]\zeta_o\right\} \qquad (A25)$$

and

$$F_{\Delta\theta h} = -\frac{\bar{\omega}_\Delta^2 \mathcal{R}_h}{\Delta}\left\{\left[sin2\theta_h - \mathcal{R}_{wh}\left(F_\beta - 1 - \frac{3}{2}\frac{e}{(1-e)}\right)\right]\beta_o - (\mathcal{R}_{wh}F_\zeta - cos2\theta_h)\zeta_o\right\} \qquad (A26)$$

$$C_{\Delta\theta h} = -\frac{\bar{\omega}_\Delta^2 \mathcal{R}_h}{\Delta}\left\{(cos2\theta_h - \mathcal{R}_{wh}F_\zeta)\beta_o - \left[sin2\theta_h + \mathcal{R}_{wh}\left(C_\zeta - \frac{3}{2}\frac{e}{(1-e)}\right)\right]\zeta_o\right\} \qquad (A27)$$

and where

$$\mathcal{R}_{wb} = \frac{\bar{\omega}_\Delta^2}{\bar{\omega}_{\beta o}^2\bar{\omega}_{\zeta o}^2}\left[(1 - \mathcal{R}_b)sin2\theta_b - \mathcal{R}_h(2\,sin^2\theta_h sin2\theta_b + sin2\theta_h cos2\theta_b)\right] \qquad (A28)$$

$$\mathcal{R}_{wh} = \frac{\bar{\omega}_\Delta^2}{\bar{\omega}_{\beta o}^2\bar{\omega}_{\zeta o}^2}\left[(1 - \mathcal{R}_h)sin2\theta_h - \mathcal{R}_b(2\,sin^2\theta_b sin2\theta_h + sin2\theta_b cos2\theta_h)\right] \qquad (A29)$$

For those cases where stall and nonlinear aerodynamics may be neglected, the following substitutions are made.

$$\alpha = \theta - \phi_i \qquad (A30)$$

$$c_{l_o} = c_{l_p} + a\alpha; \quad c_{l_\alpha} = a \qquad (A31)$$

$$c_{d_o} = c_{d_p}; \quad c_{d_\alpha} = 0 \qquad (A32)$$

The effects of pitch-lag or pitch-flap coupling are included by setting

$$\Delta\theta = \theta_\beta\Delta\beta + \theta_\zeta\Delta\zeta \qquad (A33)$$

The structural perturbation angles, $\Delta\theta_b$ and $\Delta\theta_h$, may also be coupled to flap and lead-lag perturbations, but not necessarily with the same coupling terms.

$$\Delta\theta_b = \theta_{\beta b}\Delta\beta + \theta_{\zeta b}\Delta\zeta \qquad (A34)$$

$$\Delta\theta_h = \theta_{\beta h}\Delta\beta + \theta_{\zeta h}\Delta\zeta \qquad (A35)$$

For correlation with the experimental data it was assumed that $\Delta\theta_b$ and $\Delta\theta$ were the same, and that $\Delta\theta_h$ was zero.

APPENDIX B

MODEL PROPERTIES

A two-view drawing of the rotor hub and blade is shown in figure 25. The blade is stiff relative to the hub flexures, and most of the blade motion takes place about the flexure centerlines. The lead-lag flexure, the side beam, and the flap flexure, with appropriate dimensions, are shown in figures 26–28. The assembly of these individual components can be understood by referring to figures 4 and 25. The mass and stiffness properties of each component were calculated from the design drawings; these data are tabulated in tables 3–5.

Details of the blade design and construction are shown in figure 29. The calculated mass and stiffness properties of the assembled hub and blade from B.S. 2.034 in. outboard are given in table 6. For calculation purposes the running weight and pitch inertia values were assumed to be additive. The combined stiffnesses were calculated assuming a series-spring representation for the hub flexures and the side beams.

Mass properties of the untwisted blades were obtained during their manufacture and were reported in reference 11. Average values of these properties are given in table 7. The Lock number was calculated for sea level, standard day conditions, and a lift curve slope of 5.73.

The rotor stiffness properties defined in equations (A7) through (A15) were obtained from nonrotating frequency measurements. The rotor perturbation equations may be solved for nonrotating conditions, in which case a closed form for the frequencies is obtained from equation (A17):

$$\omega_{1,2} = \left(2\omega_{\zeta o}^2 \omega_{\beta o}^2 \Big/ \left\{ (\omega_{\zeta o}^2 + \omega_{\beta o}^2) \pm (\omega_{\zeta o}^2 - \omega_{\beta o}^2)[\,1 - 4\mathcal{R}_h(1-\mathcal{R}_h)\sin^2\theta_h - 4\mathcal{R}_b(1-\mathcal{R}_b)\sin^2\theta_b + \mathcal{R}_h\mathcal{R}_b(8\sin^2\theta_h\sin^2\theta_b + 2\sin 2\theta_h \sin 2\theta_b)\,]^{\frac{1}{2}} \right\} \right)^{\frac{1}{2}} \qquad (B1)$$

The flap frequency is associated with the positive sign of the radical. The stiffness properties to be determined are nonrotating flap and lead-lag frequencies, $\omega_{\beta o}$ and $\omega_{\zeta o}$; the blade elastic coupling, $\mathcal{R}_b$; and the flexure elastic coupling, $\mathcal{R}_h$. To obtain $\omega_{\beta o}$ and $\omega_{\zeta o}$, the blade pitch angle and the flexure inclination angle were set to zero, which simplifies equation (B1) to

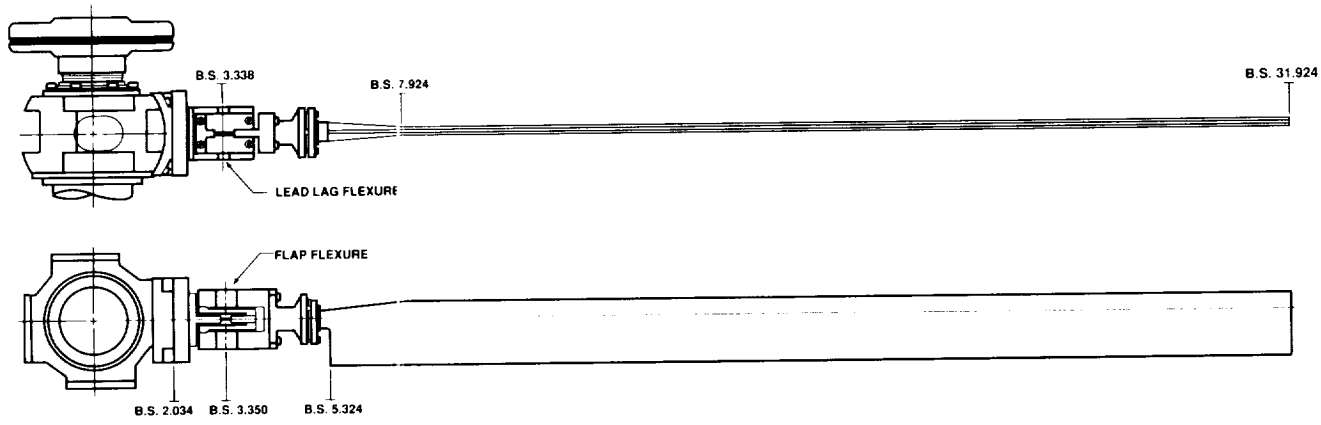

Figure 25.– Two views of rotor hub and blade.

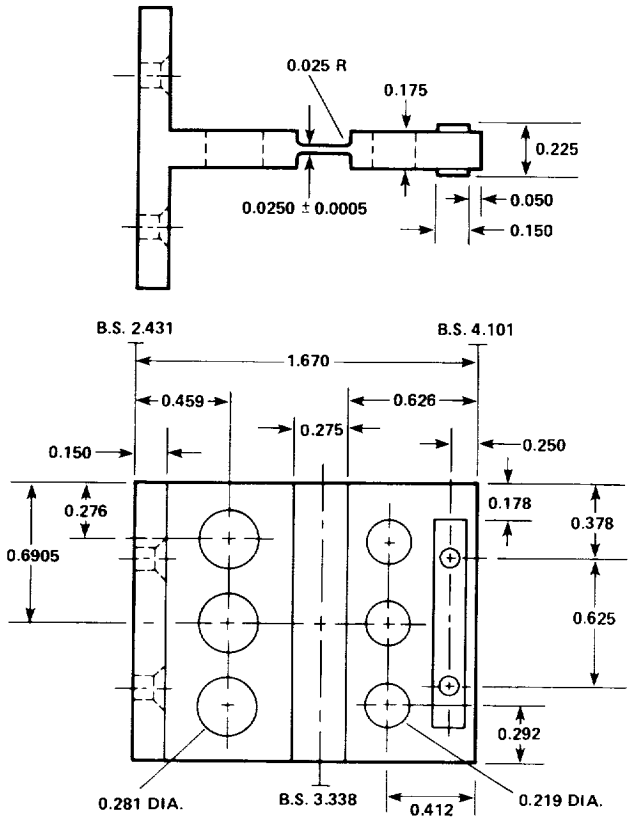

Figure 26.– Two views of lead-lag flexure.

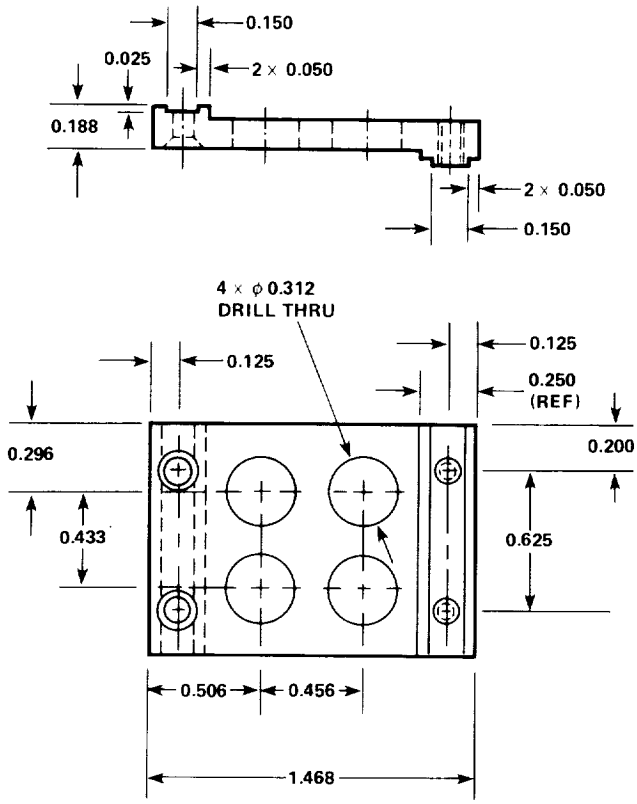

Figure 27.– Two views of flexure side beam.

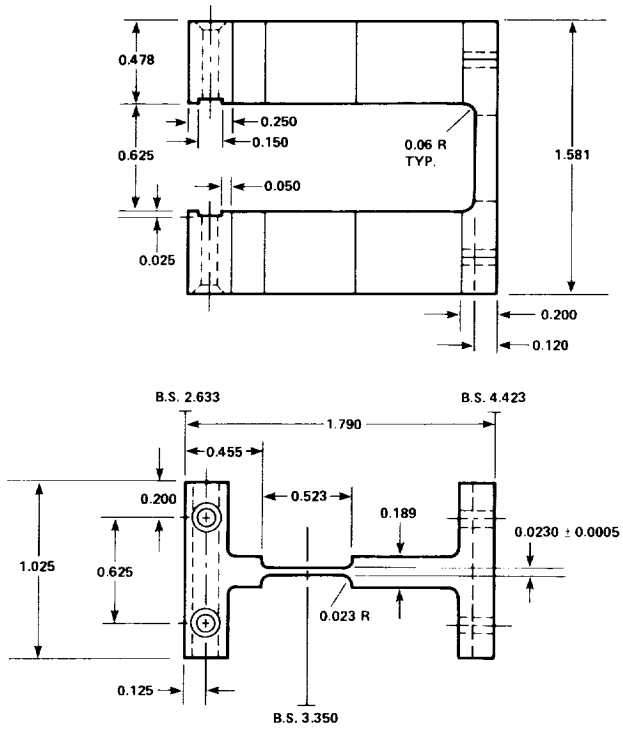

Figure 28.– Two views of flap flexure.

TABLE 3.– CALCULATED MASS AND STIFFNESS PROPERTIES OF LEAD-LAG FLEXURE[a]

Blade station, in.	Weight, $lb_m/in.$	EI_f, 10^6 lb-in^2	EI_c, 10^6 lb-in^2	GJ, 10^6 lb-in^2	I_θ, lb_m in^2/in.
2.431	0.422	5.18	5.18	3.93	0.101
2.581	0.422	5.18	5.18	3.93	0.101
2.581	0.0682	1.11	0.179	0.116	0.0110
2.750	0.0682	1.11	0.179	0.116	0.0110
2.791	0.0398	0.756	0.0102	0.116	0.0110
2.890	0.0266	0.597	0.00701	0.116	0.0110
2.989	0.0398	0.756	0.0102	0.116	0.0110
3.030	0.0682	1.11	0.0179	0.116	0.0110
3.200	0.0682	1.11	0.0179	0.116	0.0110
3.200	0.0292	0.477	0.00141	0.00139	0.00155
3.225	0.0097	0.159	0.0000521	0.00139	0.00155
3.450	0.0097	0.159	0.0000521	0.00139	0.00155
3.475	0.0292	0.477	0.00141	0.00139	0.00155
3.475	0.0682	1.11	0.0179	0.114	0.0110
3.553	0.0682	1.11	0.0179	0.114	0.0110
3.585	0.0451	0.857	0.0118	0.114	0.0110
3.663	0.0357	0.745	0.00935	0.114	0.0110
3.741	0.0451	0.857	0.0118	0.114	0.0110
3.773	0.0682	1.11	0.0179	0.114	0.0110
4.101	0.0682	1.11	0.0179	0.114	0.0110

[a]Material – 17-4 PH stainless; $\rho = 0.282\ lb_m/in^3$, $E = 29 \times 10^6\ lb/in^2$, $G = 11 \times 10^6\ lb/in^2$. Axis of symmetry coincident with 0.25c.

$$\omega_{1,2} = \sqrt{\frac{2\omega_{\zeta o}^2\omega_{\beta o}^2}{(\omega_{\zeta o}^2 + \omega_{\beta o}^2) \pm (\omega_{\zeta o}^2 + \omega_{\beta o}^2)}} \qquad (B2)$$

The values for $\omega_{\beta o}$ and $\omega_{\zeta o}$ were then obtained directly from the measurements for this uncoupled case.

The blade elastic coupling, $\mathcal{R}_b$, describes how much of the rotor flexibility is attributable to the blade. This parameter was obtained from frequency measurements made with the flexure inclination set at 0° and the blade pitch angle set at 90°. In this case, equation (B1) was rearranged as a quadratic in $\mathcal{R}_b$, and the measured lead-lag frequency was used to determine its value. The experimental data and the frequencies predicted from equation (B1) for the straight flexures are shown in figure 30. The match between theory and experiment is quite good and, of course, is exact for the solid symbols, because these were used to determine the parameters in equation (B1). For all flexure sets the agreement is within ±0.5% for lead-lag and ±1.0% for flap. Note that for the nonrotating flap mode there are separate frequencies for each blade because of slight differences in mass and stiffness. These differences do not show up in the lead-lag frequency measurements because of the way the two blades couple to form collective and differential modes. The calculation of the individual blade flap frequencies shown in figure 30 is based on their respective flap frequencies, $\omega_{\beta,1}$ and $\omega_{\beta,2}$. However, for

TABLE 4.– CALCULATED MASS AND STIFFNESS PROPERTIES OF SIDE BEAMS[a]

Blade station, in.	Weight, $lb_m/in.$	EI_f, 10^6 lb-in^2	EI_c, 10^6 lb-in^2	GJ, 10^6 lb-in^2	I_θ, lb_m in^2/in.
2.633	0.0535	0.468	0.298	0.0109	0.0105
2.883	0.0535	0.468	0.298	0.0109	0.0105
2.883	0.0410	0.359	0.190	0.0109	0.00493
2.983	0.0410	0.359	0.190	0.0109	0.00493
3.029	0.0234	0.269	0.109	0.0109	0.00493
3.139	0.0160	0.221	0.0745	0.0109	0.00493
3.249	0.0234	0.269	0.109	0.0109	0.00493
3.295	0.0410	0.359	0.190	0.0109	0.00493
3.439	0.0410	0.359	0.190	0.0109	0.00493
3.485	0.0234	0.269	0.109	0.0109	0.00493
3.595	0.0160	0.221	0.0745	0.0109	0.00493
3.705	0.0234	0.269	0.109	0.0109	0.00493
3.751	0.0410	0.359	0.190	0.0109	0.00493
3.851	0.0410	0.359	0.190	0.0109	0.00493
3.851	0.0613	0.537	0.220	0.0109	0.00957
4.101	0.0613	0.537	0.220	0.0109	0.00957

[a]Material – Ti-6Al-4V alloy; $\rho = 0.160\ lb_m/in^3$, $E = 16 \times 10^6\ lb/in^2$, $G = 6.2 \times 10^6\ lb/in^2$.

TABLE 5.– CALCULATED MASS AND STIFFNESS PROPERTIES OF FLAP FLEXURE[a]

Blade station, in.	Weight, $lb_m/in.$	EI_f, 10^6 lb-in^2	EI_c, 10^6 lb-in^2	GJ, 10^6 lb-in^2	I_θ, lb_m in^2/in.
2.633	0.276	2.49	9.20	9.92	0.114
2.883	0.276	2.49	9.20	9.92	0.114
2.883	0.0510	0.0156	1.70	1.46	0.0167
3.088	0.0510	0.0156	1.70	1.46	0.0167
3.088	0.0186	0.000759	0.621	0.0192	0.00106
3.111	0.0062	0.000028	0.207	0.0192	0.00106
3.588	0.0062	0.000028	0.207	0.0192	0.00106
3.611	0.0186	0.000759	0.621	0.0192	0.00106
3.611	0.510	0.0156	1.70	0.185	0.0167
4.223	0.510	0.0156	1.70	0.185	0.0167
4.223	0.242	2.00	0.763	3.98	0.0839
4.298	0.242	2.00	0.763	3.98	0.0839
4.298	0.368	3.54	6.62	3.98	0.0988
4.423	0.368	3.54	6.62	3.98	0.0988

[a]Material – 17-4 PH stainless; $\rho = 0.282\ lb_m/in^3$, $E = 29 \times 10^6\ lb/in^2$, $G = 11 \times 10^6\ lb/in^2$. Axis of symmetry coincident with 0.25c.

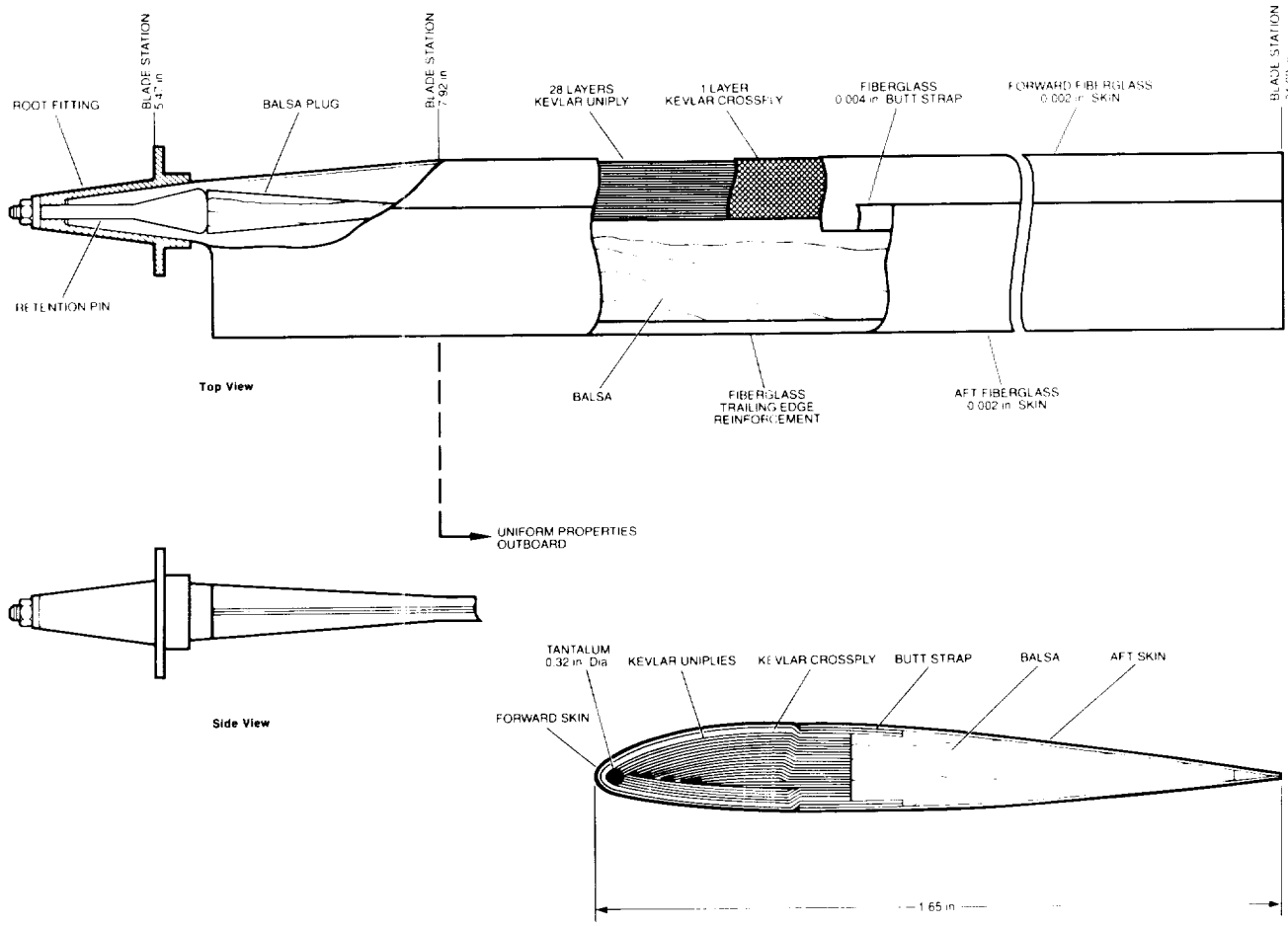

Figure 29.– Blade design and construction details.

all other computations in this report, the uncoupled nonrotating flap frequency is assumed to be the mean of the two values shown.

The flexure elastic coupling, $\mathcal{R}_h$, was calculated from nonrotating frequency measurements obtained as the flexure inclination was varied with the blade pitch angle set at 0°. The coupling value was determined from equation (B1) in a least squares sense. In figure 31, the calculated frequency variation using the fitted value of $\mathcal{R}_h$ is shown for configuration one as the flexure inclination is varied. The match with the lead-lag frequency is $\pm 0.6\%$. The agreement in flap frequency is poorer, at $\pm 4.0\%$.

Nonrotating frequency measurements were made for all four configurations, and the computed stiffness parameters are presented in table 8. Note that for configurations two and three the flexure inclination was not varied, therefore no value of $\mathcal{R}_h$ was computed.

The predictions of nonrotating frequency are quite good in the general case where both flexure inclination and blade pitch angle are nonzero. This is shown in figure 32, in which the nonrotating frequency variation is plotted as a function of blade pitch angle for $\theta_h = 36°$. The difference between theory and experiment is less than 1% for lead-lag, and on the order of 2% for flap.

The torsion and the higher flap and lead-lag bending modes have been measured for configuration one, and the results were reported in reference 6. The measured nonrotating torsion frequency including the effects of flexures and blade was 342 Hz. At the highest rotor speed tested, this

TABLE 6.– CALCULATED MASS AND STIFFNESS PROPERTIES OF HUB FLEXURES AND BLADE

Blade station, in.	Weight, $lb_m/in.$	EI_f, 10^6 lb-in^2	EI_c, 10^6 lb-in^2	GJ, 10^6 lb-in^2	I_θ, lb_m in^2/in.
2.034	0.573	20.1	20.1	15.6	0.403
2.431	0.573	20.1	20.1	15.6	0.403
2.431	0.422	5.18	5.18	3.93	0.101
2.581	0.422	5.18	5.18	3.93	0.101
2.581	0.0533	1.11	0.0179	3.93	0.101
2.633	0.0533	1.11	0.0179	3.93	0.101
2.633	0.398	0.291	0.0169	0.00995	0.136
2.750	0.398	0.291	0.0169	0.00995	0.136
2.791	0.369	0.259	0.00985	0.00995	0.136
2.883	0.357	0.239	0.00706	0.00995	0.136
2.883	0.120	0.0146	0.00695	0.00990	0.0326
2.890	0.119	0.0146	0.00673	0.00990	0.0326
2.983	0.131	0.0147	0.00945	0.00990	0.0326
2.989	0.131	0.0147	0.00962	0.00990	0.0326
3.030	0.143	0.0146	0.0152	0.00990	0.0326
3.088	0.139	0.0145	0.0148	0.00990	0.0326
3.088	0.106	0.000756	0.0146	0.00656	0.0170
3.111	0.0923	0.000028	0.0138	0.00656	0.0170
3.139	0.0904	0.000028	0.0135	0.00656	0.0170
3.200	0.0945	0.000028	0.0140	0.00656	0.0170
3.200	0.0555	0.000028	0.00138	0.00116	0.00754
3.225	0.0377	0.000028	0.000052	0.00116	0.00754
3.249	0.0393	0.000028	0.000052	0.00116	0.00754
3.295	0.0569	0.000028	0.000052	0.00116	0.00754
3.439	0.0569	0.000028	0.000052	0.00116	0.00754
3.450	0.0527	0.000028	0.000052	0.00116	0.00754
3.475	0.0626	0.000028	0.00139	0.00116	0.00754
3.475	0.102	0.000028	0.0146	0.00655	0.0170
3.485	0.0978	0.000028	0.0143	0.00655	0.0170
3.553	0.0932	0.000028	0.0142	0.00655	0.0170
3.585	0.0680	0.000028	0.00976	0.00655	0.0170
3.588	0.0674	0.000028	0.00968	0.00655	0.0170
3.595	0.0699	0.000250	0.00967	0.00655	0.0170
3.611	0.0777	0.000756	0.00952	0.00655	0.0170
3.611	0.110	0.0143	0.00961	0.00944	0.0326
3.663	0.107	0.0144	0.00848	0.00944	0.0326
3.705	0.115	0.0145	0.00969	0.00944	0.0326
3.741	0.133	0.0146	0.0110	0.00944	0.0326
3.751	0.144	0.0147	0.0127	0.00944	0.0326

TABLE 6.– CONCLUDED

Blade station, in.	Weight, $lb_m/in.$	EI_f, 10^6 lb-in^2	EI_c, 10^6 lb-in^2	GJ, 10^6 lb-in^2	I_θ, lb_m in^2/in.
3.773	0.160	0.0148	0.0162	0.00944	0.0326
3.851	0.160	0.0148	0.0162	0.00944	0.0326
3.851	0.181	0.0150	0.0164	0.00944	0.0373
4.101	0.181	0.0150	0.0164	0.00944	0.0373
4.101	0.051	0.0156	1.70	0.185	0.0167
4.223	0.051	0.0156	1.70	0.185	0.0167
4.223	0.222	1.77	3.66	2.18	0.0550
4.484	0.220	1.77	3.66	2.18	0.0550
4.484	0.231	1.77	3.66	2.18	0.0550
4.613	0.231	1.77	3.66	2.18	0.0550
4.613	0.0529	1.24	1.24	0.0959	0.00247
5.078	0.0510	1.24	1.24	0.0959	0.00243
5.260	0.191	1.24	1.24	0.0959	0.0394
5.410	0.191	1.24	1.24	0.0959	0.0394
5.410	0.0243	0.0459	0.0459	0.0238	0.000728
5.469	0.0291	0.0538	0.0538	0.0288	0.000867
5.469	0.119	0.0538	0.0538	0.0288	0.0147
5.529	0.118	0.0991	0.0991	0.0616	0.0155
5.529	0.155	0.0991	0.0991	0.0616	0.0295
5.659	0.160	0.101	0.101	0.0596	0.0297
5.659	0.0447	0.101	0.101	0.0596	0.00172
5.764	0.0470	0.102	0.102	0.0568	0.00167
5.764	0.0332	0.0526	0.0526	0.0187	0.000684
5.924	0.00763	0.00228	0.0617	0.0012	0.000711
7.924	0.00758	0.00228	0.0617	0.0012	0.000869
31.924	0.00758	0.00228	0.0617	0.0012	0.000869

TABLE 7.– ROTOR MASS PROPERTIES

Parameter	Value
Blade inertia, I, slug-ft^2	0.0118
Lock number, γ	7.99
Blade mass, m_b, slug	0.0159
Mass c.g. from centerline, r_{cg}, in.	10.06

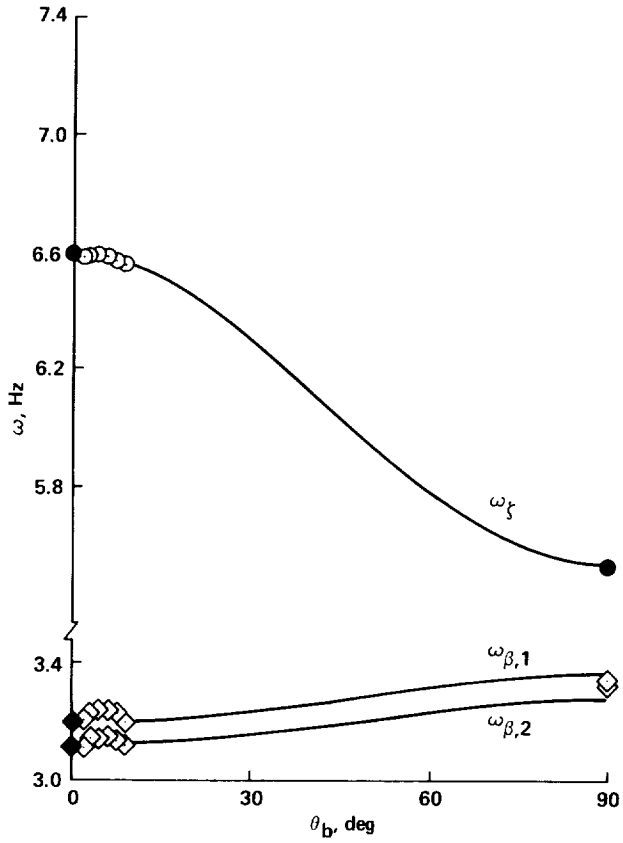

Figure 30.– Nonrotating lead-lag and flap-lag frequencies as functions of blade pitch angle for straight flap/straight lead-lag flexures (configuration one); $\theta_h = 0°, \mathcal{R}_b = 0.13$. Solid symbols indicate values used to calculate the stiffness parameters.

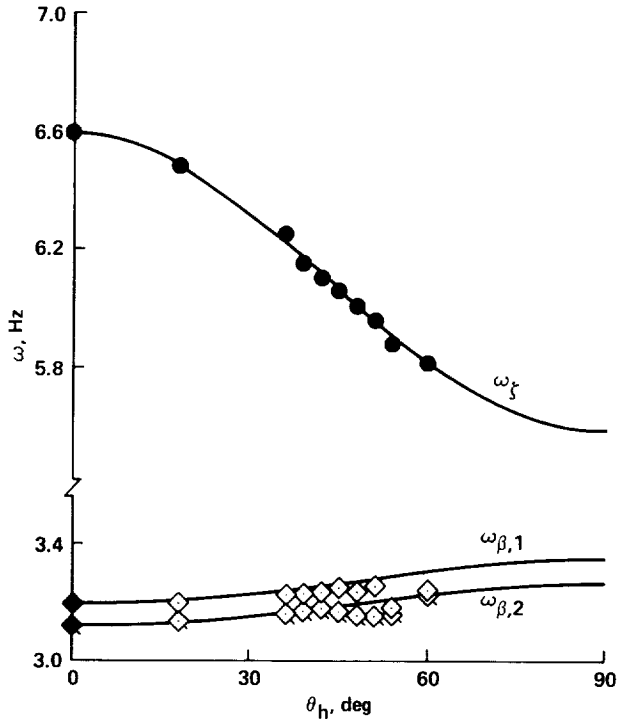

Figure 31.– Nonrotating lead-lag and flap-lag frequencies as a function of flexure inclination for straight flap and straight lead-lag flexures (configuration one); $\theta_b = 0°$, $\mathcal{R}_h = 0.88$. Solid symbols indicate values used to calculate the stiffness parameters.

TABLE 8.– ROTOR STIFFNESS PARAMETERS

Configuration	Flap flexures	Lead-lag flexures	$\omega_{\beta o}$, Hz	$\omega_{\zeta o}$, Hz	$\mathcal{R}_b$	$\mathcal{R}_h$
1	Straight	Straight	3.159	6.592	0.13	0.88
2	Straight	Skewed	3.118	7.087	0.12	–
3	Skewed	Straight	3.142	6.610	0.12	–
4	Skewed	Skewed	3.204	7.200	0.13	0.88

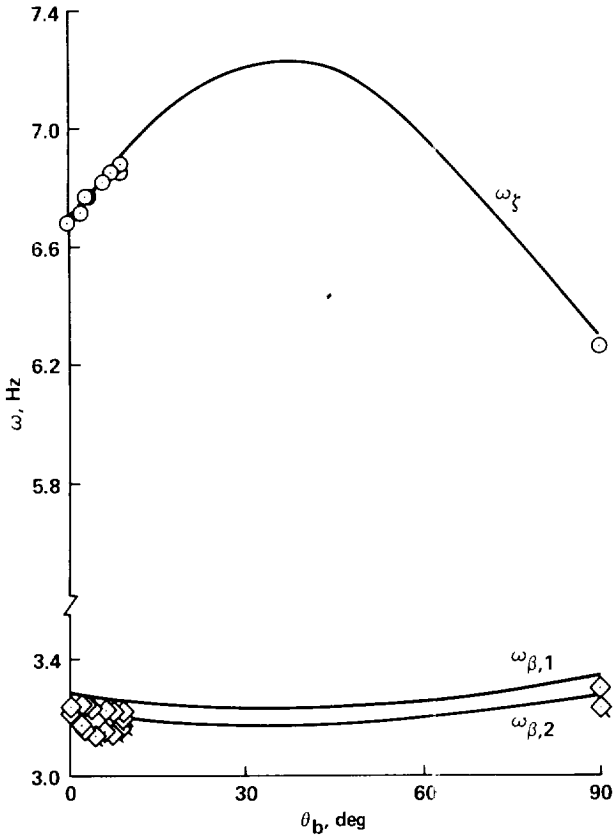

Figure 32.– Nonrotating lead-lag and flap-lag frequencies as functions of blade pitch angle for the skewed flap/skewed lead-lag flexures (configuration four); $\theta_h = 36°$.

gives a torsion frequency above 24/rev. Theoretical predictions of the stability of an isolated elastic blade which include the torsion degree of freedom (ref. 12) have shown that the torsion mode does not affect blade stability unless the torsion frequency is below 16/rev; therefore, the torsion mode should have no effect on rotor stability for this experiment. The higher blade modes are also well separated in frequency from the fundamental flap and lead-lag frequencies. The nonrotating second and third flap mode frequencies were 32 and 96 Hz, respectively, and the second and third lead-lag mode frequencies were 150 and 356 Hz.

The structural damping of the blade and flexure combination was determined from the transient decay during nonrotating tests. The values for the four flexure configurations are shown in table 9.

Steady flexure bending-moment data from tests of configuration four were used to estimate nonlinear aerodynamic section characteristics of the rotor. Using equations (A1), (A5), and (A6), the section lift and drag coefficients may be expressed as a function of the steady moment data:

$$\begin{Bmatrix} c_{l_o} \\ c_{d_o} \end{Bmatrix} = \begin{bmatrix} 1 & -\phi_i \\ \phi_i & -1 \end{bmatrix}^{-1} \left(\begin{bmatrix} F_\beta & F_\zeta \\ C_\beta & C_\zeta \end{bmatrix} \begin{Bmatrix} \beta_o \\ \zeta_o \end{Bmatrix} + \begin{Bmatrix} g m_b r_{cg} / I\Omega^2 \\ 0 \end{Bmatrix} \right) \Big/ \frac{\gamma B^4}{8a} \left(1 - \frac{4}{3} \frac{e}{B} \right) \qquad (B3)$$

TABLE 9.– BLADE/FLEXURE NONROTATING DAMPING

Configuration	Flap flexures	Lead-lag flexures	Structural damping, % critical
1	Straight	Straight	0.27
2	Straight	Skewed	0.46
3	Skewed	Straight	0.29
4	Skewed	Skewed	0.20

The solution for the section coefficients from the steady bending moment data is iterative, since the induced flow, ϕ_i, is also a function of c_{l_o}. Section lift and drag coefficient data calculated for $\theta_h = 0°$ are shown in figures 33 and 34. Scatter in the calculated coefficients is shown by indicating one standard deviation on either side of the mean value. Section lift and drag coefficient data from reference 13 for an NACA 0012 profile have been added to these figures for comparison. The section lift coefficient data in figure 33 have been shifted by $\Delta c_l = 0.15$ to account for the camber on the NACA 23012 profile used here. Relatively good agreement is seen for the section lift coefficient, but the section drag coefficient data calculated here show a greater rise in drag with angle of attack than was recorded in reference 13.

The lift and drag characteristics in figures 33 and 34 are approximated by the functions

$$c_l = 0.15 + 5.73\alpha \qquad (B4)$$

$$c_d = 0.0079 + 1.5\alpha^2 \qquad (B5)$$

These functions have been used for all of the theoretical calculations presented in this report. The tip loss factor, B, is assumed to be 0.97.

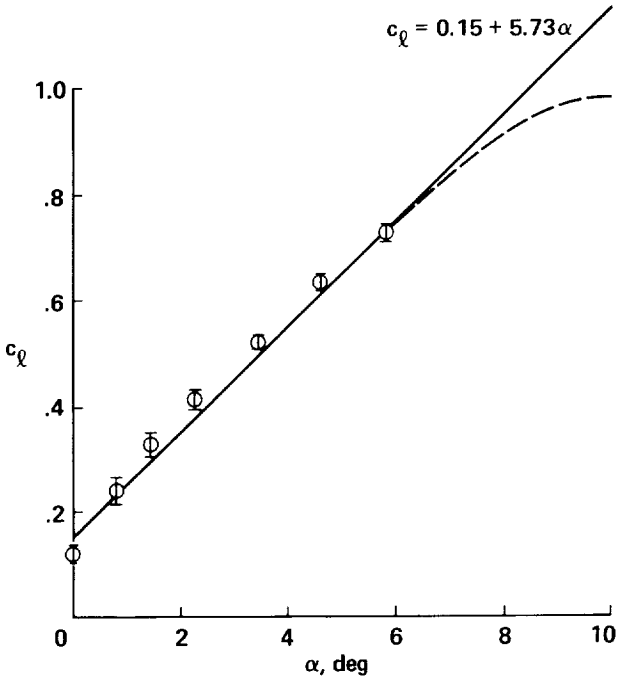

Figure 33.– Section lift coefficient derived from steady bending moment data for configuration four, $Re \approx 130,000$. Dashed curve is from reference 13, $Re \approx 250,000$.

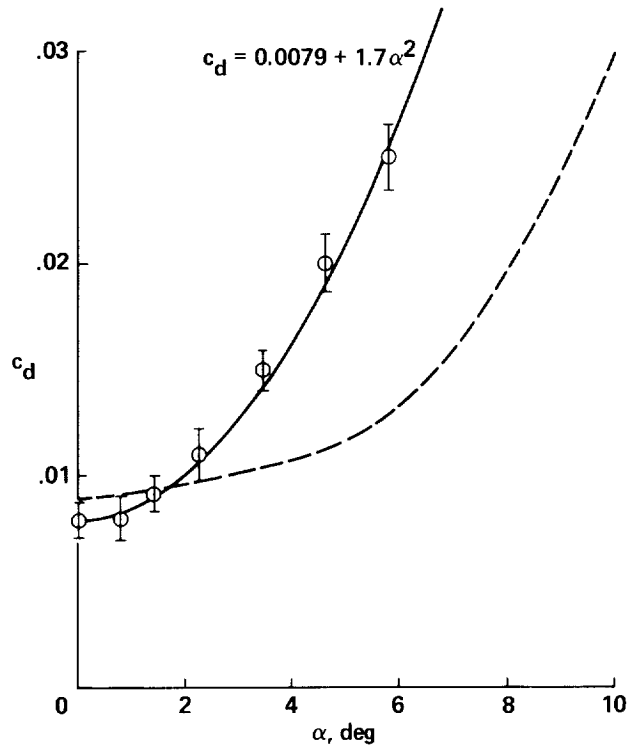

Figure 34.– Section drag coefficient derived from steady bending moment data for configuration four, $Re \approx 130,000$. Dashed curve is from reference 13, $Re \approx 330,000$.

APPENDIX C

EFFECTS OF STAND FLEXIBILITY ON BLADE LEAD-LAG DAMPING

Introduction

The observed difference between experiment and theory for damping at zero blade pitch and zero flexure inclination for configuration one (fig. 13(a)) is perplexing, in that the flap-lag equations become uncoupled under these conditions, and the only sources of lead-lag damping in the equations are structural damping and blade profile drag damping. The structural damping can be calculated quite accurately from nonrotating data, and the profile drag damping can be calculated from steady bending moment data, as discussed in appendix B. Although the profile drag damping measurements show considerable scatter, the estimated damping is an order of magnitude less than that required to explain the damping difference. A second experiment was undertaken to investigate this problem. Frequency and damping measurements were obtained at rotor speeds from zero, where theory and experiment agreed, up to the speeds used in the original test. There was increasing error in both frequency and damping as rotor speed was increased, which suggested that the stand flexibility might be coupling with the blade motions, and therefore the experiments were expanded to examine the effect of stand flexibility independent of rotor speed.

In the next section of this appendix is a description of the ways in which the stand flexibility was varied for the present experiment. Frequency and damping data are then presented as a function of rotor speed at five different values of stand flexibility. An approximate criterion for the stand stiffness required to avoid significant errors due to coupling between the lead-lag and stand degrees of freedom is discussed. Finally, a correction factor is obtained from these data and applied to the theoretical calculations for configurations with and without flexure inclination.

Experiment Description

The model rotor and hub used in the second experiment was the same as that in the original experiment except for minor changes in the excitation linkage and in the cable mounting. The model used for the second test is shown in figure 35 (compare with fig. 7). (Cables were used to stiffen the stand in both experiments, but had not been installed at the time the figure 7 photograph was taken.) The testing and data reduction methods were the same for both experiments.

Stand flexibility was varied by (1) changing the body roll spring, (2) using pneumatic clamps to lock the shaker excitation linkage, (3) using a body snubber normally used only for coupled rotor-body tests, and (4) changing the cable tension. The first three approaches affected the stand's lateral mode primarily, by changing the stiffness across the roll gimbal. The fourth approach, that of changing the cable tension, affected both the lateral and the longitudinal stand modes.

The gimbal design of the test stand allows freedom in both pitch and roll. The pitch degree of freedom was not needed for these tests, so it was locked out by fastening the yoke directly to the outer gimbal frame. The roll degree of freedom, however, was needed so that the blade lead-lag mode could be excited with the shaker, and damping measurements could be obtained from the excitation decay. The four methods of varying stand flexibility are discussed in more detail below.

1. Selection of either a soft or a stiff body-roll spring. The soft spring allowed substantial body roll motion and therefore it was easy to excite the rotor lead-lag mode with the shaker. The stiff spring, however, provided a significant restraining force across the gimbal, and restricted the amplitude of hub motion.

Figure 35.– Two-bladed rotor model used during second experiment.

2. Shaker linkage and pneumatic clamps. Under normal test procedures the pneumatic clamps were used to lock out the excitation linkage after the lead-lag motion had been built up to a sufficient level for measurements to be made. The shaker linkage and clamping mechanism can be seen at the left in figure 8. The combination of the excitation linkage and clamps acted as a very stiff spring across the roll gimbal. In this respect its behavior was similar to the body-roll spring, although the spring attachment points are different. It was possible, however, to bypass the clamping mechanism, and when this was done the shaker excitation linkage acted as a very soft spring across the roll gimbal, again in a fashion analogous to the soft body-roll spring.
3. Body snubber. This was mounted beneath the model, as shown in figure 8. When activated, it was forced against the model and became a third, parallel spring across the roll gimbal, independent of the roll spring and pneumatic clamp linkage. When the snubber was off, it did not contact the model, and became a zero-stiffness spring.
4. Cable tension. This means of varying stand stiffness affected the longitudinal and lateral stand modes equally. The stiffening cables were attached to the upper stand just below the yoke that supports the gimbal and the model, and ran from there to mounting strips on the test cell floor, as shown in figure 35. Cable tension was effected by either fully tightening or completely loosening the four cables.

Using these four methods of varying the stand flexibility, five stand configurations or cases were defined, as shown in table 10. The lateral stand frequency varied from 23 to 33 Hz for the five cases. The longitudinal stand frequency was not measured for each case, but in general was 1 or 2 Hz higher than the lateral. The experimental data presented in the main body of this report were obtained with the configuration identified as case 3 in table 10; this is considered the nominal case.

Experimental Results

Effect of Stand Stiffness on Frequency and Damping– In figure 36, for the five cases of stand flexibility defined in table 10, the lead-lag frequency and damping measurements are shown as functions of rotor speed. These are compared to the theoretical calculations from the model discussed in appendix A. For case 1, which has the lowest stand frequency, the data and theory show significant differences above rotor speeds of 250 to 350 rpm. This difference increases as rotor speed is increased. The data show a decrease in the lead-lag frequency as rotor speed is increased above 700 rpm—a trend that is significantly different from the theoretical behavior. For case 2, the differences between theory and experiment are reduced compared to case 1, and the agreement becomes better as the stand stiffness is increased for cases 3, 4, and 5. For the nominal case shown in figure 36(c), the agreement appears to be satisfactory up to rotor speeds of around 500 rpm, but significant differences are seen over

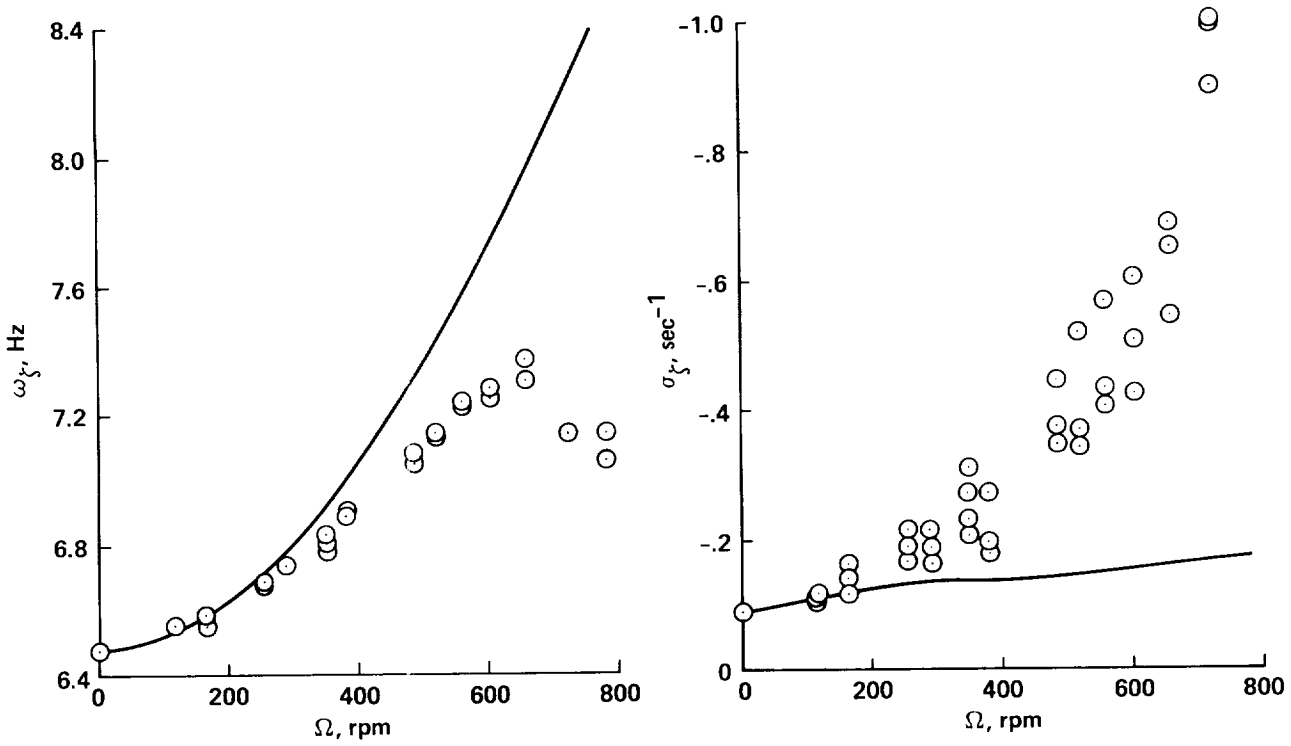

(a) ω_Y = 22.7 Hz.

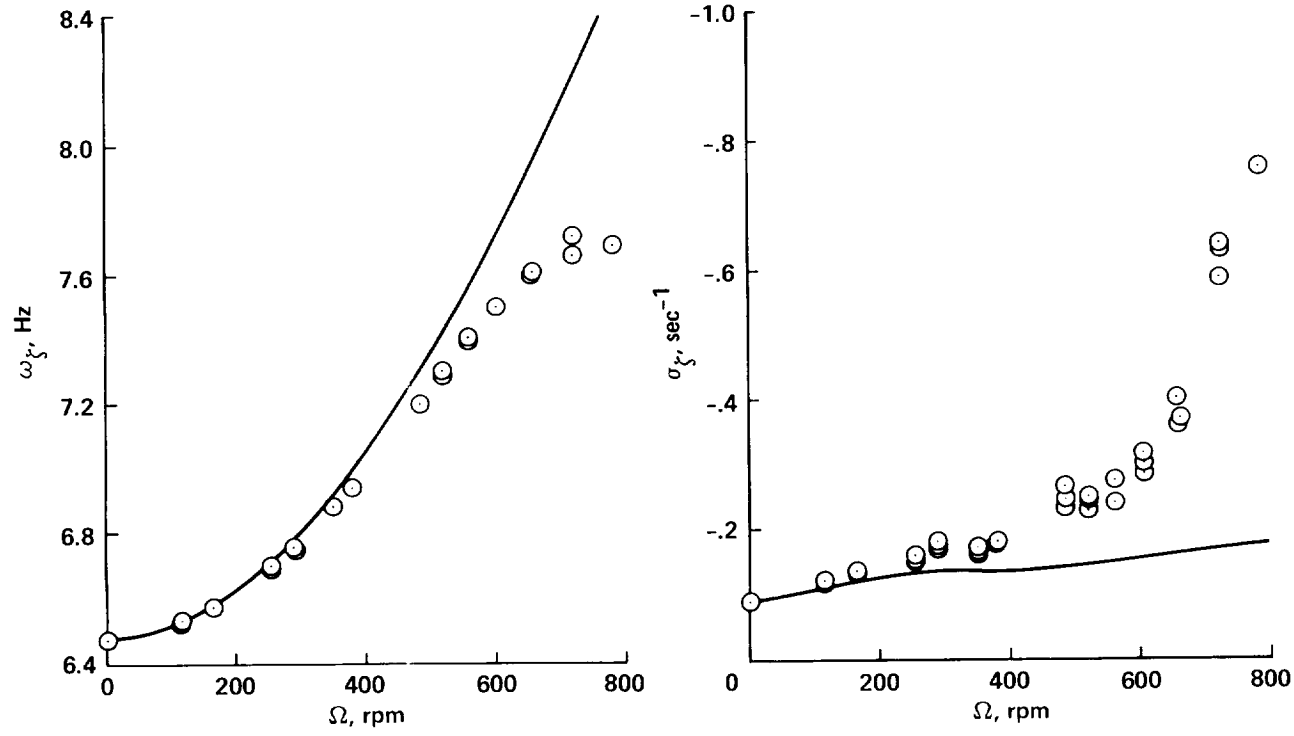

(b) ω_Y = 24.7 Hz.

Figure 36.– Lead-lag frequency and damping as functions of rotor speed for five values of lateral test stand stiffness; straight flap/straight lead-lag flexures, $\theta_h = \theta_b = 0°$.

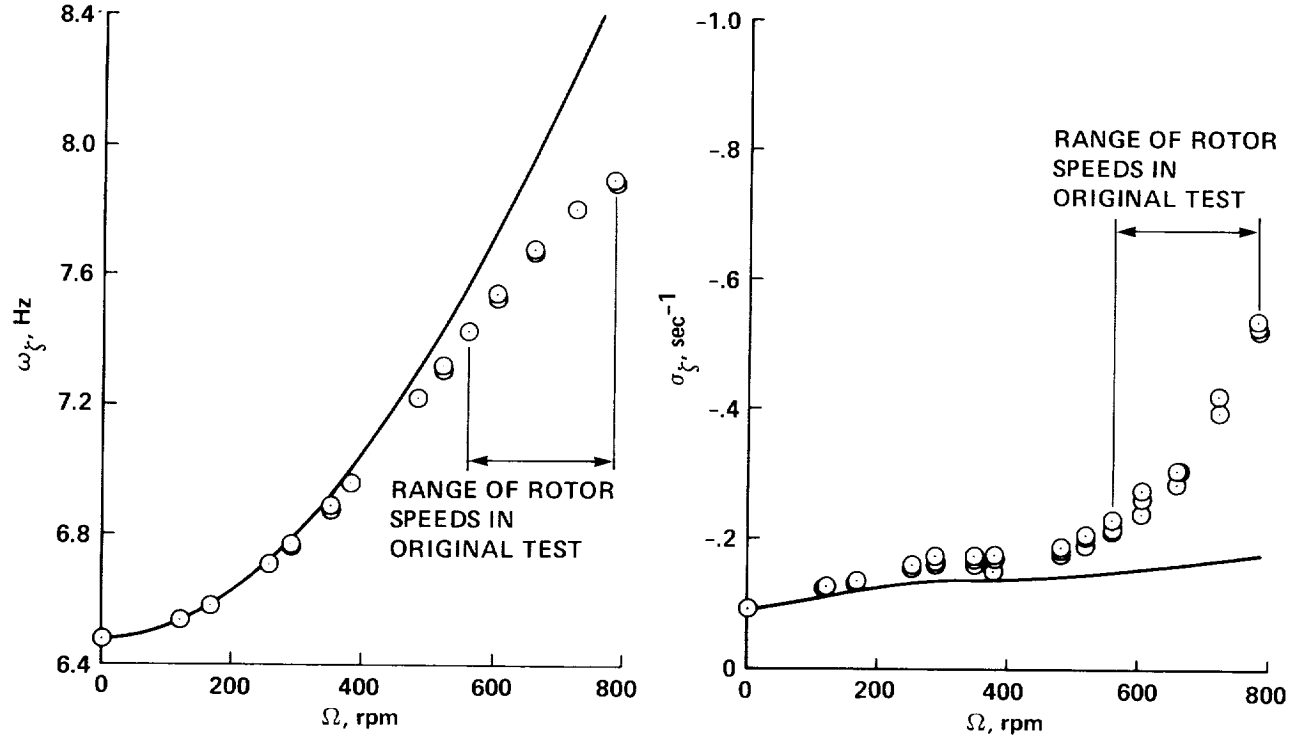

(c) ω_Y = 27.2 Hz.

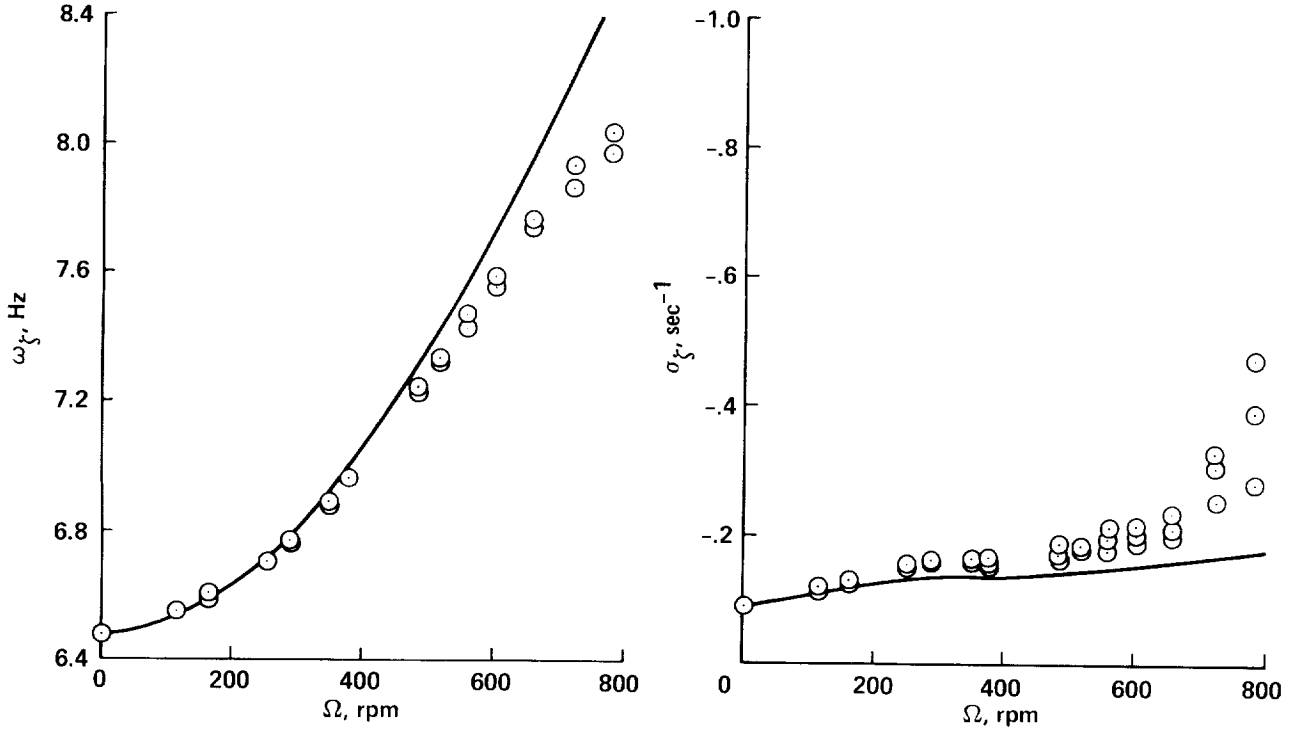

(d) ω_Y = 31.9 Hz.

Figure 36.– Continued.

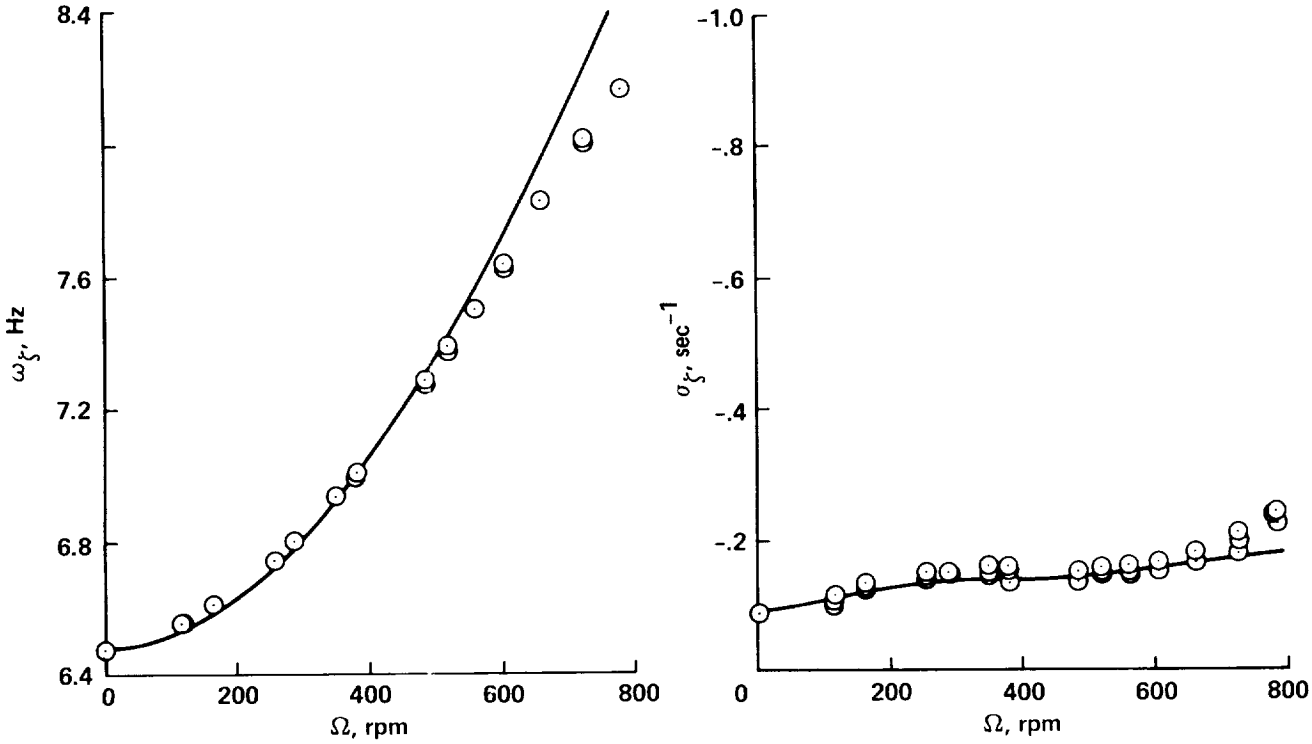

(e) ω_Y = 33.4 Hz.

Figure 36.– Concluded.

TABLE 10.– STAND CONFIGURATIONS

Case	ω_Y, Hz	Cables	Roll spring	Pneumatic clamp	Snubber
1	22.7	Taut	Maximum	Unclamped	Off
2	24.7	Slack	Minimum	Clamped	Off
3	27.2	Taut	Minimum	Clamped	Off
4	31.9	Taut	Maximum	Clamped	Off
5	33.4	Taut	Maximum	Clamped	On

the range of rotor speeds tested in the original experiment. For the stiffest configuration tested, theory and experiment agree for frequency to about 600 rpm, and for damping to nearly 800 rpm.

The comparison of frequency and damping data in figure 36 shows that the difference or error depends on the rotor speed and the stand frequency. It is proposed that the observed differences are caused by coupling of the lead-lag mode at a frequency of $\Omega + \omega_\zeta$ with the stand frequency, ω_Y. The ratio of these two terms is defined as the stand frequency ratio,

$$\frac{\Omega + \omega_\zeta}{\omega_Y}$$

It is expected that as this ratio approaches zero the difference or error in frequency and damping should also approach zero. As the ratio increases toward one, the difference should increase as well. The frequency difference is shown in figure 37 as a function of the stand frequency ratio. The y-axis of this plot has been shifted for each case so that the behavior can be more clearly seen. A curve has been faired through the data for each case, and the resulting curves are combined in figure 38. This figure shows that as the stand frequency ratio is reduced, the difference between the theoretical predictions and the measurements appears to be approaching an asymptote (not necessarily zero).

The difference between the measured and calculated damping shown in figure 36 is plotted in figure 39 as a function of the stand frequency ratio. The y-axis is again split for the five stiffness cases so that the behavior of the damping difference as a function of stand frequency ratio can be clearly seen. A composite plot of the hand-fitted curves is shown in figure 40. As the stand frequency ratio is reduced, the damping difference appears to be approaching an asymptote as was the case with the frequency data.

At stand frequency ratios above about 0.5, the rate of change in the frequency and damping differences rapidly increases, which reflects the strong coupling between the rotor and stand. Below this

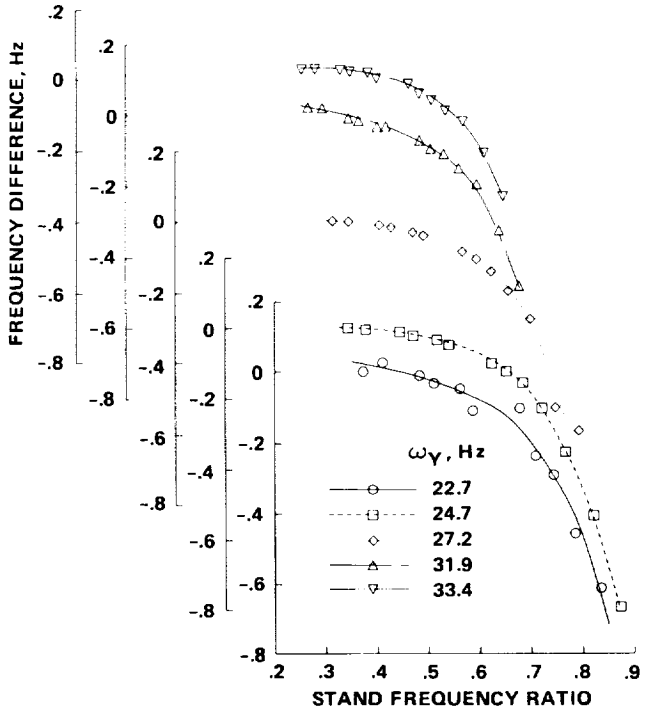

Figure 37.– Frequency difference as a function of the stand frequency ratio shown for five stand stiffness cases.

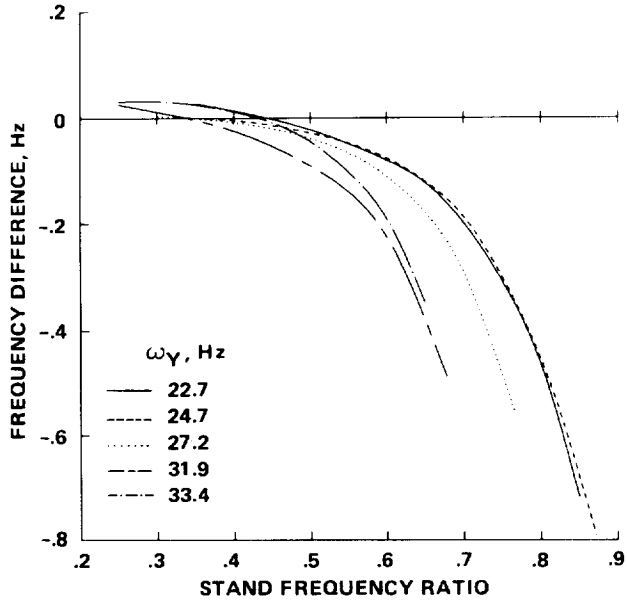

Figure 38.– Composite plot of frequency difference as a function of the stand frequency ratio.

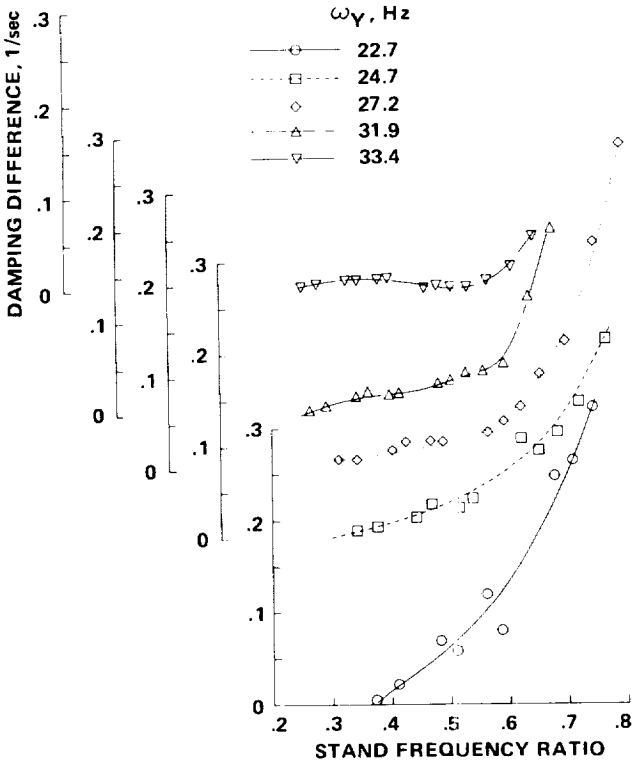

Figure 39.– Damping difference as a function of the stand frequency ratio shown for five stand stiffness cases.

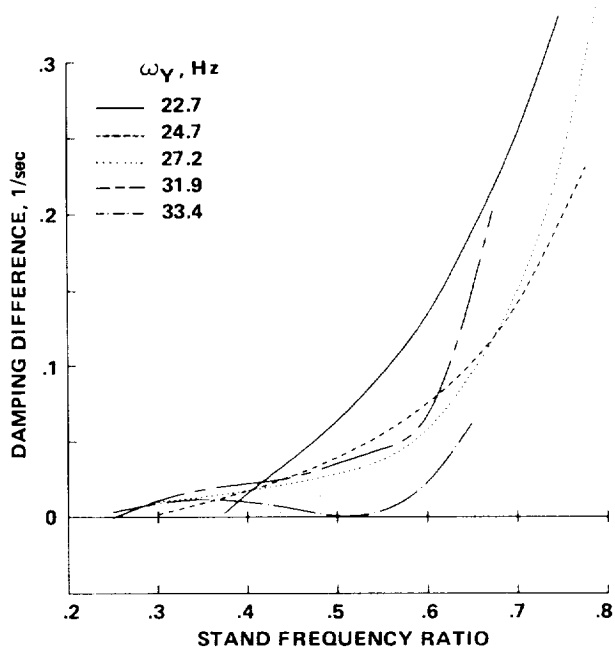

Figure 40.– Composite plot of damping difference as a function of the stand frequency ratio.

value the rate of change is significantly reduced. These results suggest that the stand frequency must be two and one-half to three times stiffer than the highest lead-lag frequency in the fixed system to avoid the kinds of problems that have been observed here.

Frequency and Damping Corrections– The regular behavior of the frequency and damping differences observed in figure 36 as rotor speed is varied suggests that the difference term as identified here could be used to "correct" the theoretical predictions in this report. The potential for such a correction has been examined using the results in this appendix. For a particular test condition the rotor speed, calculated lead-lag frequency, and stand frequency were used to determine the stand frequency ratio. The frequency and damping differences were then obtained from figures 37 and 39 for the third stiffness case, ω_Y = 27.2 Hz, which corresponded to the stand configuration used in the experiment. These experimentally determined differences were then added to the original theoretical predictions and the results were compared with the measurements. Such a "correction" should essentially be exact for configuration one at zero flexure inclination, as this is the configuration from which the correction was derived. What is of interest, however, is whether the correction is appropriate for other configurations and flexure inclinations.

The experimental data, theoretical predictions, and corrected theory are compared for two cases with zero flexure inclination in figure 41. The configuration-one results shown in figure 41(a) are good, as was expected. Figure 41(b) shows the pitch-lag coupled case, configuration two. In this case using the correction improves the agreement, but does not provide an exact match. The correction is, of course, larger at the lower values of nondimensional lead-lag frequency, which correspond to higher rotor speeds. The adequacy of the correction

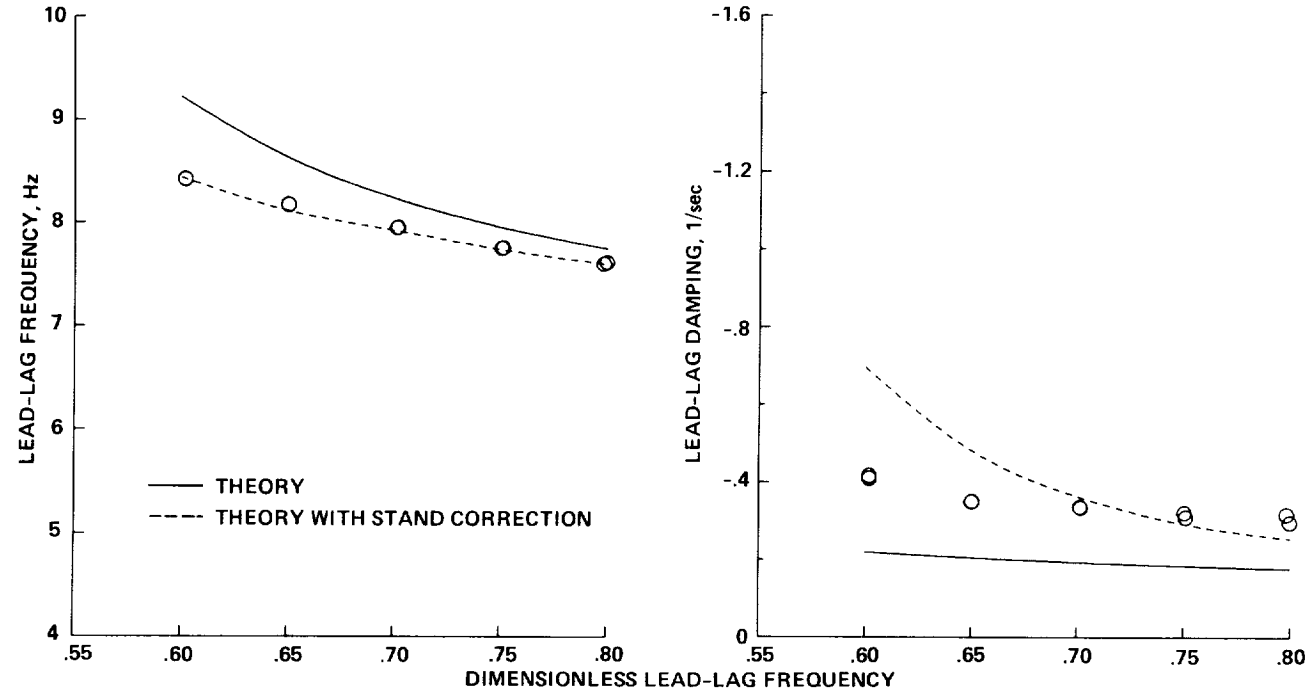

(a) Straight flap/straight lead-lag flexures (configuration one); $\theta_\beta = \theta_\zeta = 0$.

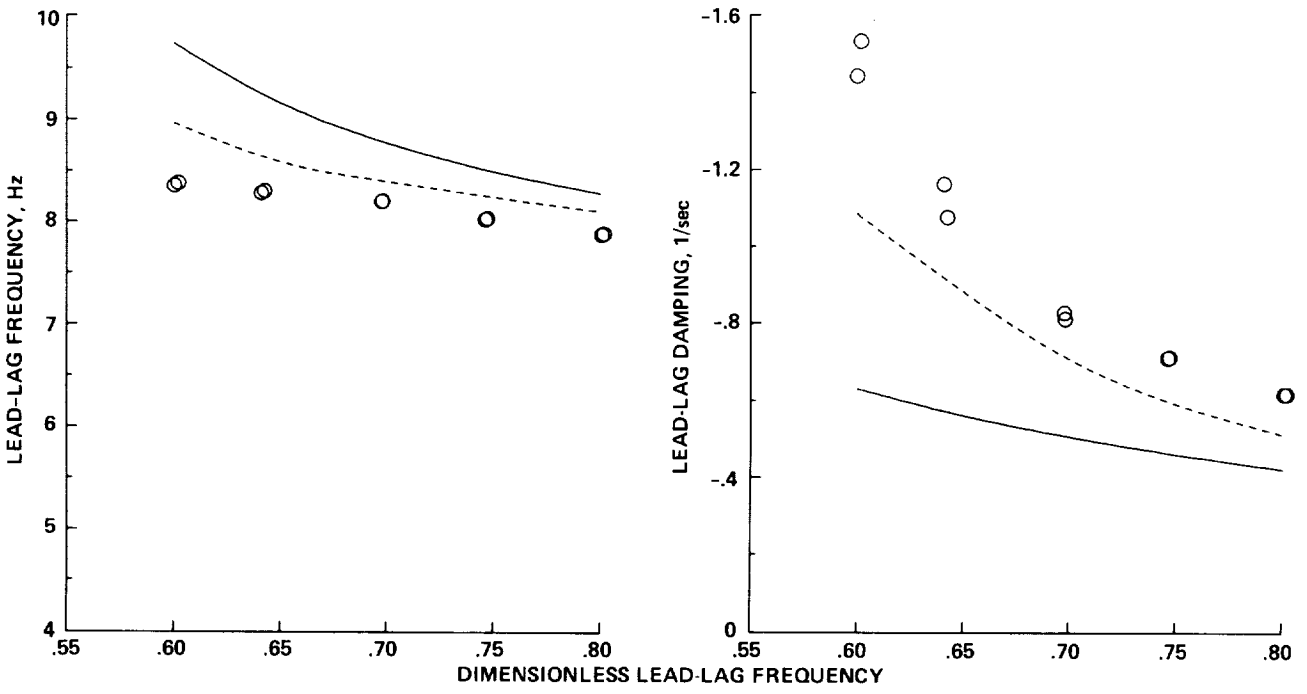

(b) Straight flap/skewed lead-lag flexures (configuration two); $\theta_\beta = 0, \theta_\zeta = -0.41$.

Figure 41.– Lead-lag frequency and damping as functions of nondimensional lead-lag frequency, including correction for stand coupling, $\theta_h = \theta_b = 0°$.

term at a flexure inclination of 36° for configuration one can be determined from figure 42. The correction term is smaller for this case, because the test rotor speed is lower. Use of the correction term results in some improvement in the damping at higher rotor speeds, but has no effect at all at the lower rotor speeds where the largest difference between theory and experiment is seen. It appears that coupling between the stand and the blade lead-lag degree of freedom can explain some of the differences seen between theory and measurement at a flexure inclination of 0°, but it does not explain the differences seen at the other flexure angles.

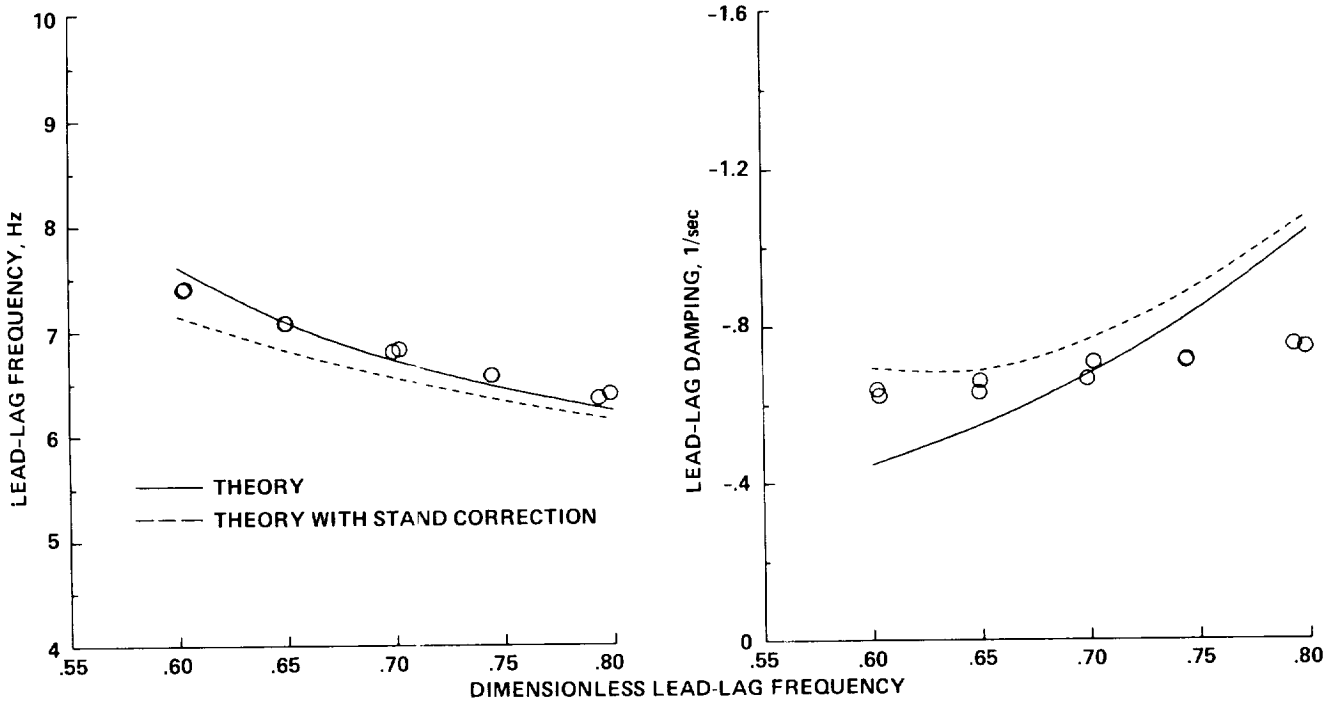

Figure 42.– Lead-lag frequency and damping as functions of nondimensional lead-lag frequency for straight flap/straight lead-lag flexures (configuration one), including correction for stand coupling; $\theta_h = 36°, \theta_\beta = \theta_\zeta = 0$.

REFERENCES

1. Ormiston, Robert A.; and Hodges, Dewey H.: Linear Flap-lag Dynamics of Hingeless Helicopter Rotor Blades in Hover. J. Am. Helicop. Soc., vol. 17, no. 2, Apr. 1972, pp. 2-14.
2. Ormiston, R. A.; and Bousman, W. G.: A Study of Stall-Induced Flap-lag Instability of Hingeless Rotors. Preprint No. 730, AHS 29th Annual National Forum, Washington, D.C., May 1973.
3. Curtiss, H. C., Jr.; and Putman, W. F.: An Experimental Investigation of the Flap-lag Stability of a Hingeless Rotor with Comparable Levels of Hub and Blade Stiffness in Hovering Flight. Princeton University, AMS Report No. 1300, June 1976.
4. Ormiston, R. A.: Techniques for Improving the Stability of Soft Inplane Hingeless Rotors. NASA TM X-62,390, 1974.
5. Bousman, W. G.; Sharpe, D. L.; and Ormiston, R. A.: An Experimental Study of Techniques for Increasing the Lead-lag Damping of Soft Inplane Hingeless Rotors. Preprint No. 1035, AHS 32nd Annual National V/STOL Forum, Washington, D.C., May 1976.
6. Bousman, William G.: An Experimental Investigation of Hingeless Helicopter Rotor-Body Stability in Hover. NASA TM 78489, 1978.
7. Lewis, Richard B., II: Army Helicopter Performance Trends. J. Am. Helicop. Soc., vol. 17, no. 2, April 1972, pp. 15-23.
8. Sharpe, David L.: An Experimental Investigation of the Flap-Lag-Torsion Aeroelastic Stability of a Small-Scale Hingeless Helicopter Rotor in Hover. NASA TP 2546, AVSCOM TR 85-A-9, 1986.
9. Bousman, William G.: An Analog Technique for the Measurement of Damping From Transient Decay Signals. NASA TM X-73,121, 1976.
10. Kaza, K. R. V.; and Kvaternik, R. G.: Examination of the Flap-lag Stability of Rigid Articulated Rotor Blades. J. Aircraft, vol. 16, no. 2, Dec. 1979, pp. 876-884.
11. Silcox, H.F.: Analytical and Model Investigations of Hingeless Rotor Air Stability, Volume 1, Section A: Structural Analysis – Rigid Blades, Report No. D210-10475-1A, Boeing Company, 1972.
12. Hodges, Dewey H.; and Ormiston, Robert A.: Stability of Elastic Bending and Torsion of Uniform Cantilevered Rotor Blades in Hover. AIAA Paper 73-405, AIAA/ASME/SAE 14th Structures, Structural Dynamics, and Materials Conference, Apr. 1973.
13. Jacobs, E. E.; and Sherman, A.: Airfoil Section Characteristics as Affected by the Variation of the Reynolds Number. NACA Report No. 586, 1936.

NASA
National Aeronautics and Space Administration

Report Documentation Page

1. Report No.	2. Government Accession No.	3. Recipient's Catalog No.
NASA TP- 3002 AVSCOM TR-89-A-002		

4. Title and Subtitle	5. Report Date
The Effects of Structural Flap-Lag and Pitch-Lag Coupling on Soft Inplane Hingeless Rotor Stability in Hover	May 1990
	6. Performing Organization Code

7. Author(s)	8. Performing Organization Report No.
William G. Bousman	A-89093
	10. Work Unit No. 992-21-01

9. Performing Organization Name and Address	11. Contract or Grant No.
Ames Research Center, Moffett Field, CA 94035-1000 and Aeroflightdynamics Directorate, U.S. Army Aviation Research And Technology Activity, Ames Research Center, Moffett Field, CA 94035-1099	
	13. Type of Report and Period Covered Technical Publication

12. Sponsoring Agency Name and Address	14. Sponsoring Agency Code
National Aeronautics and Space Administration, Washington, DC 20546-0001 and U.S. Army Aviation Systems Command, St. Louis, MO 63120-1798	

15. Supplementary Notes

Point of Contact: William G. Bousman, Ames Research Center, MS 215-1, Moffett Field, CA 94035-1000 (415) 604-3748 or FTS 464-3748

16. Abstract

A 1.62-m-diameter rotor model was tested in hover to examine the effects of structural flap-lag and pitch-lag coupling on isolated rotor blade lead-lag stability. Flap-lag coupling was introduced by inclining the principal axes of the blade structure up to 60°. Pitch-lag coupling was obtained either alone or in combination with flap-lag coupling through the use of skewed flexural hinges. The principal results confirm the predictions of theory, and show that both structural flap-lag and pitch-lag coupling when used separately are beneficial to blade stability. Moreover, when the couplings are combined, the lead-lag damping is significantly greater than it would be if the individual contributions were superimposed. Pitch-flap coupling is shown to have only a minor effect on blade lead-lag damping. Differences between theory and experiment observed at zero blade pitch and flexure angles during the initial testing were determined in a second test to be caused by stand flexibility. Other differences between theory and experiment warrant further investigation.

17. Key Words (Suggested by Author(s))	18. Distribution Statement
Hingeless rotor stability, Aeroelastic coupling, Helicopter model testing, Helicopter aeroelastic stability, Flap-lag coupling, Pitch-lag coupling	Unclassified-Unlimited Subject Category - 02

19. Security Classif. (of this report)	20. Security Classif. (of this page)	21. No. of Pages	22. Price
Unclassified	Unclassified	65	A04

For sale by the National Technical Information Service, Springfield, Virginia 22161

NASA-Langley, 1990

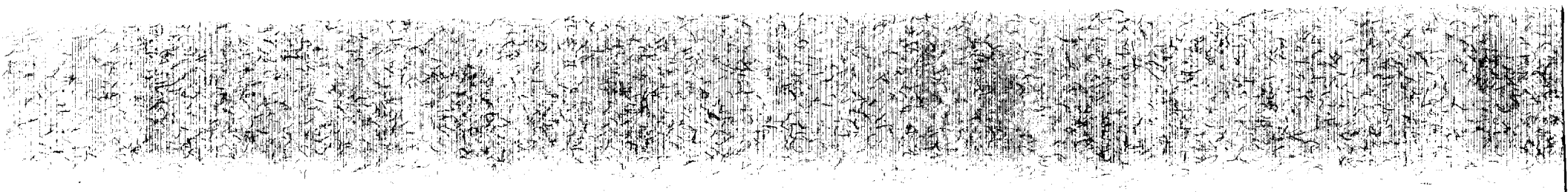

National Aeronautics and
Space Administration
Code NTT-4

Washington, D.C.
20546-0001

NASA